Analysis and preparation of (bio)nanoobjects in nano-microfluidic devices

Dissertation

submitted in partial fulfillment
of the requirements for the degree of
Doktor der Naturwissenschaften
(Dr. rer. nat.)

M.Sc. Martina Viefhues

Bielefeld University
Faculty of Physics
December 2012

Hiermit versichere ich, dass ich die vorliegende Arbeit selbstständig verfasst und keine anderen als die angegebenen Quellen und Hilfsmittel benutzt habe, dass alle Stellen der Arbeit, die wörtlich oder sinngemäß aus anderen Quellen übernommen wurden, als solche kenntlich gemacht sind, und dass die Arbeit in gleicher oder ähnlicher Form noch keiner Prüfungsbehörde vorgelegt wurde.

Bielefeld, den 3. Dezember 2012

(Martina Viefhues)

Gutachter
Prof.Dr. Thomas Huser
Prof.Dr. Andreas Hütten

Eingereicht am 3. Dezember 2012

Preface

Alle dargestellten Experimente wurden von mir selbst durchgeführt mit Ausnahme der Polarisierbarkeitsmessungen, die unter meiner Anleitung von Eugenie Fredrich und Verena Leder während ihrer Abschlussarbeiten durchgeführt wurden. Die experimentelle Umsetzung der multiplen Trennung wurde von Sonja Wegener während ihrer Masterarbeit unter meiner Anleitung durchgeführt. Die Simulationen der Teilchenbewegungen in den Kanalstrukturen wurden von Dr. Ralf Eichhorn entwickelt, programmiert und durchgeführt.

Die zentralen Ergebnisse der Arbeit sind bereits in der Fachliteratur veröffentlicht oder werden in kürze erscheinen. Es ist zu beachten, dass aufgrund der Heirat der Autorin sich der Nachname von Everwand zu Viefhues ändert.

1. M. Everwand, D. Anselmetti, and R. Regtmeier. On-Chip continuous-flow interaction studies of DNA and protein complexed DNA, Proceedings to 14th International Conference on Miniaturized Systems for Chemistry and Life Sciences (μTAS), October 3-7, 2010, Groningen, The Netherlands: 19-21, 2010.

2. J. Regtmeier, J. Käsewieter, M. Everwand, and D. Anselmetti. Continuous-flow Separation of Nanoparticles by Electrostatic Sieving at a Micro-nanofluidic interface, J. Separation Science, 34, Issue 10: 1180-1183, 2011.

3. J. Regtmeier, R. Eichhorn, M. Viefhues, L. Bogunovic, and D. Anselmetti. Electrodeless Dielectrophoresis for Bioanalysis: Theory, Devices and Applications, Electrophoresis, 32 (17), 2253-2273 , 2011 (invited review).

4. M. Viefhues, S. Marchanda, T.-C. Chao, D. Anselmetti, J. Regtmeier, and A. Ros. Physisorbed Surface Coatings for Poly(dimethylsiloxane) and Quartz Microfluidic Devices, Analytical and Bioanalytical Chemistry, 401, 2113-2122, 2011.

5. M. Viefhues, R. Eichhorn, E. Fredrich, J. Regtmeier, and D. Anselmetti, Continuous and Reversible Mixing or Demixing of Nanoparticles by Dielectrophoresis, Lab Chip, 12, 485-494, 2012.

6. A. Rischmüller, M. Viefhues, M. Dieding, M. Schmeer, R. Baier, D. Anselmetti and M. Schleef, Analytical tools in minicircle production, in: Minicircle and Miniplasmids DNA vectors. The future of non-viral and viral gene transfer, Edited by M. Schleef, Wiley-VCH, Weinheim, ISBN: 3527324569, 2012.

7. M. Viefhues, J. Regtmeier and D. Anselmetti, Nanofluidic devices for dielectrophoretic mobility shift assays by soft lithography, J. Micromech. and Microeng., 22, 115024, 2012.

8. M. Viefhues, J. Regtmeier and D. Anselmetti, Fast and continuous-flow separation of DNA-complexes and topological DNA variants in microfluidic chip format, Analyst, 138 (1), 186 - 196, 2013.

9. M. Viefhues, S. Wegener, A. Rischmüller, M. Schleef and D. Anselmetti, Continuous-flow dielectrophoresis for multiple-separation of DNA, in preparation

10. J. Regtmeier, S. Gerkens, M.Viefhues, L. Bogunovic and D. Anselmetti, Valveless pumping with one actuated membrane, in preparation.

Contents

1 Introduction **1**

2 Theory **5**

2.1 DNA 5

2.1.1 Statistical description 7

2.1.2 Fluorescence labeling of DNA 8

2.1.3 Protein-DNA and drug-DNA complexes 10

2.2 Gelelectrophoresis and electrophoretic mobility shift assays 12

2.3 Electrokinetics and hydrodynamics 13

2.3.1 Scaling laws and hydrodynamics on the μm-scale 13

2.3.2 The electrical double layer 14

2.3.3 Electrophoresis and electroosmosis 15

2.3.4 Dielectrophoresis 17

2.4 Intermolecular interactions 21

2.5 Brownian motion and diffusion 21

2.6 Kramers rate and first mean passage time 22

3 Materials and methods **24**

3.1 Biomolecular methods 24

3.1.1 Reproduction and extraction of DNA 24

3.1.2 Gelelectrophoresis/ EMSA 24

3.2 Production of masterwafer 25

3.3 Preparation of microfluidic chip 26

3.4 Experimental setup 29

3.5 Experimental procedures 31

3.5.1 Polystyrene bead procedures 31

3.5.2 DNA procedures 34

3.6 AFM imaging of DNA/RNAP-complexes 38

4 Results and discussion **39**

4.1 Production of device 39

4.2 Electrostatic sieving of nanoobjects 43

4.3 Concept of dielectrophoretic mixing and separation 48
4.4 Dielectrophoretic nanobead manipulation 57
4.4.1 Mixing of nanobeads 57
4.4.2 Separation of nanobeads 59
4.5 DNA manipulation and characterization by dielectrophoresis 63
4.5.1 DNA separation 63
4.5.2 Continuous-flow detection of DNA-complexes 70
4.5.3 Dielectrophoretic mobility shift assays (DEMSA) 73
4.5.4 Determination of polarizability 75
4.5.5 Electrophoretic mobility shift assay (EMSA) 76
4.5.6 DNA mixing 78
4.5.7 Summary: DNA manipulation and separation by dielectrophoresis . 81

5 Summary and Outlook **83**

Appendix **87**
Results of single DNA experiments 87
AFM images of nanobeads 89
List of Publications 91
Contributions to Conferences 92

Bibliography **94**

1 Introduction

In 1990 Manz et al. developed the concept of micro total analysis systems (μTAS) [1]. The idea of μTAS is to build a few cm^2 sized device that consists of several preparative and analytical tools to realize a so-called Lab-on-a-chip. Since that time the development as well as the range of applications continuously increase as regularly reviewed [2–16]. But even when the development has made significant progress in particular investigations of nanoobjects like small DNA-fragments or proteins are still a blind spot. With respect to the size of these, the devices must be further miniaturized towards nanofluidics.

Up to now, the precise and reproducible production of nanochannels is very challenging [17]. Most often nanochannels are produced by chemical or physical etching that is very time-consuming and expensive [18]. Thus, new techniques for production of nanochannels are required.

Two major applications can be envisioned for nanofluidic devices in medicine [9, 19, 20]: 1) the extremely fast detection of minimal amounts of specific markers, 2) new tools for faster drug design. In medicine early detection of specific markers is indispensable to start therapies as soon as possible. Beyond development of new detection methods, ever since investigation concentrates on developing new drugs. During drug discovery, interaction studies are performed to investigate the sensitivity and specificity of the drug, which is often very cumbersome [21]. In recent years a new class of therapy became more prominent, the so-called gene vaccination [22–25]. Gene vaccination is the introduction of genes of interest into patients. Most often viral and bacterial vector systems were used as transporter systems [24]. This revealed great hindrances concerning safety regulations as the viral or bacterial gens were inserted, too. In contrast, *minicircle* DNA consists only of the gene of interest and its regulating sequences [22–25]. Thus, production and purification control of *minicircle* DNA is of very high interest for medical applications.

To accelerate and push these amazing medical approaches μTAS preparative tools like mixing or separation/purification as well as analytical tools for detection of specific analytes or complex-formation have to be developed.

Several microfluidic analytical and preparative separation methods have been realized, so far. Some are based on hydrodynamic separation [26–31]. For example, Yamada and Seki exploited that particles of different sizes were aligned at different distances to the channel wall within a pinched microchannel. They were separated according to the particles sizes by the spreading flow profile at the constriction outlet [26]. Other separation techniques were based on magnetic fields [32–36], e.g. functionalized magnetic beads with receptor molecules on the surface. Electric fields yield a wide field of applications in microfluidics as for electrophoresis [37–42] or dielectrophoresis [3, 43–48]. Additionally, entropy was exploited to separate linear molecules like DNA in entropic ratchets [49–52]. Many of the mixing devices, published in literature, used diffusion in augmented contact areas as was nicely summarized in recent reviews [9, 12, 15, 16, 19, 53–55].

In this thesis, all methods that are demonstrated relied on one or several ridges that

narrowed a microchannel, and thus formed nanoslits. At these devices electric voltages were applied that effected electrophoretic, electroosmotic, dielectrophoretic and electrostatic sieving effects either in the microchannel or at the nanoslits.

Hence, the experimentalist had some parameters to control the processing performance:

- $U_{dc} \rightarrow$ linear transport effects
- $U_{ac} \rightarrow$ non-linear transport effects
- $\omega \rightarrow$ non-linear transport effects
- slit height $\rightarrow$ potential depth
- shape of ridge $\rightarrow$ ratio of linear and non-linear transport effects
- buffer concentration $\rightarrow$ sieving mechanism
- channel dimensions $\rightarrow$ geometrical factor

Generally, the processing mode can be distinguished between batch-processing and continuous-flow processing. In batch-processing mode, one partition of analyte is processed at a time. Whereas in continuous-flow mode, an analyte-stream is continuously injected towards the processing area and a real-time monitoring of the results, e.g. in analytical separation, is possible as well as on-line optimization, continuous harvesting or further downstream applications [32, 36, 56–63]. Thus, continuous-flow processing is of very high interest for μTAS for smart and maybe even self-optimizing devices (see Outlook).

In this thesis, several features were combined concerning the device as well as the performance that appear very contrary at a first glance. So, the device allowed easy and cost-effective fabrication of sophisticated nano-microfluidic channels. The techniques allowed efficient separation as well as mixing in one and the same device. And, especially with respect to μTAS, the novel tools enabled preparation as well as analysis. Although this was very challenging, the successful realization is laid out in this thesis.

The results are divided in five parts:

1. Production and characterization of the nano-microfluidic devices (section 4.1): presentation of novel technique that allowed fast prototyping of nano-microfluidic devices of very high width-to-height aspect ratio and characterization with respect to the stability and reproducibility. With that novel technique, a world record aspect ratio was achieved.

2. Electrostatic sieving of nanoobjects (section 4.2): realization of continuous-flow separation of nanobeads and manipulation of proteins by electrostatic sieving. Concentration polarization at the nanoslit was exploited to selectively manipulate nanobeads and proteins. Although the concentration polarization was known for a long time no continuous-flow operation of electrostatic sieving have been demonstrated to date.

3. Concept of continuous-flow dielectrophoresis (section 4.3): separation of mixtures of two or more species and mixing of analytes in one and the same device just by adapting the injection. The general requirements of the system are discussed concerning the electrokinetic effects and the device layout. Simulations of separation and mixing were performed and allowed analysis of the sensitivity of the system, i.e. minimal difference in size that could be sufficiently distinguished.

4. Dielectrophoretic nanobead manipulation (section 4.4): experimental results of continuous-flow mixing and separation of nanobeads. The separation procedure is demonstrated for mixtures of two or three species (100 nm, 60 nm, and 20 nm beads). Although various devices for continuous-flow separation of microbeads were published in literature for dielectrophoresis and electrodeless dielectrophoresis, the minimal manipulated bead size was 1 μm [58, 60, 61, 64–72]. Thus, nanobeads or small DNA-fragments were not accessible, except with the devices presented in this thesis. In case of mixing, some methods that exploited dielectrophoresis at microelectrodes were published [60, 73–79]. In contrast, here for the first time, continuous-flow mixing was performed by electrodeless dielectrophoresis.

5. DNA manipulation and characterization by dielectrophoresis (section 4.5): preparative and analytical separation of topological DNA variants. Continuous-flow separation and mixing of biological and medical relevant DNA-molecules were performed in the vicinity of nanochannels. Binary separation and mixing experiments proved the general applicability to linear DNA (2.686 kbp and 6.0 kbp) as well as circular DNA (parental DNA and *minicircle* DNA). Beyond binary separation, even more sophisticated total multiple-separation of parental, miniplasmid and *minicircle* DNA was achieved for the first time without the need of specific matrices.

   Concerning analytical separation, two novel fast methods for detection of DNA-complex formation are presented. The first method relied on continuous-flow separation of pure DNA and the anticipated DNA-complex. Hence, further downstream analysis would be possible. The second method was termed dielectrophoretic mobility shift assay (DEMSA) due to the detection technique. The DEMSA was a batch-processing technique that was based on dielectrophoretically retarded migration within an array of nanoslits.

Even when the before mentioned techniques differ, the general procedures/handling was similar for all continuous-flow experiments. So, the analyte was injected towards the structured channel and affected at the nanoslits. Downstream of the nanoslit the fluorescence intensity distribution was monitored and evaluated (see also figure 1.1).

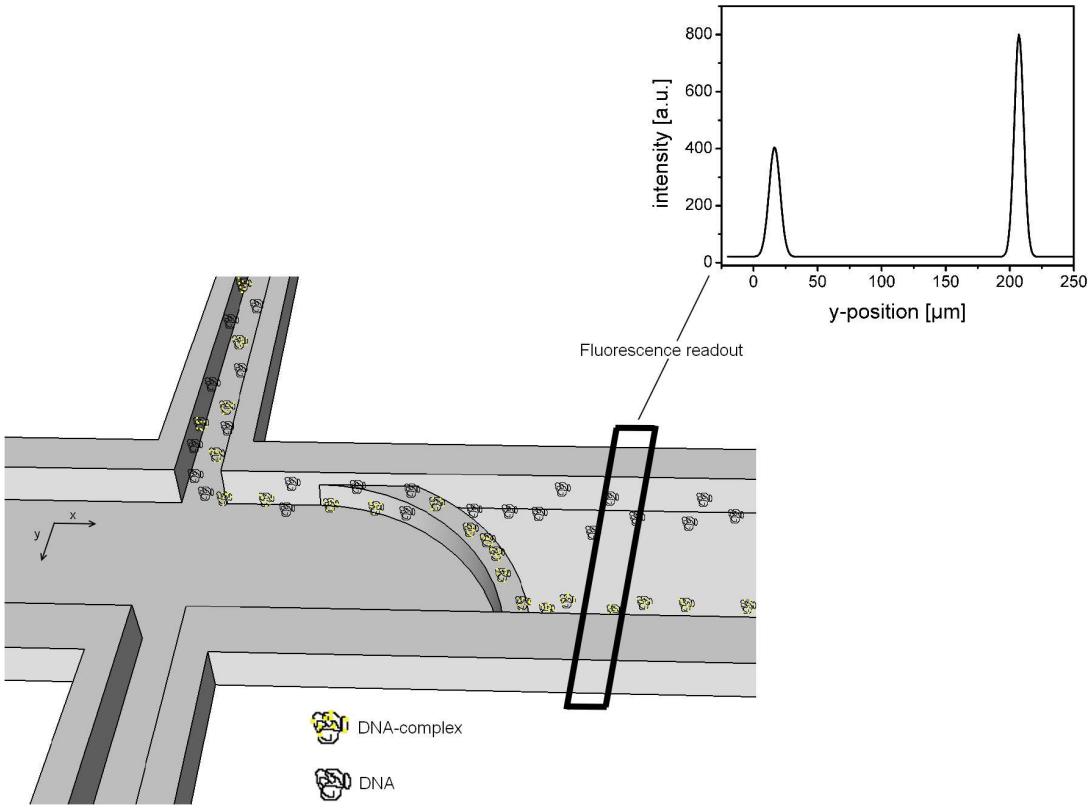

Figure 1.1: *Scheme of the continuous-flow separation and analysis. The analyte is injected towards the ridge as a narrow stream. At the ridge, one species is deflected, the second species passes the ridge unaffected. Downstream of the ridge the response is monitored by fluorescence intensity distributions.*

2 Theory

2.1 DNA

Deoxyribonucleic acid (DNA) is a long polymer that encodes the genetic information of every living organism. *Via* DNA the genetic information is passed from parental generation to daughter generation and so serves as long time information memory [80]. The genetic information is encoded by four different nucleotides that build the DNA. The nucleotides consist of a sugar (deoxyribose), phosphate and one base of adenine, thymine, guanine, or cytosine, respectively. Sugar and phosphate form the so-called backbone of the DNA whereas the bases lie in between (figure 2.1). Two of the bases are purines (adenine and guanine) and the others are pyrimidines (cytosine and thymine). One purine and one pyrimidine at a time are bound *via* hydrogenbonds forming complementary pairs, adenine and thymine with two hydrogen bonds and cytosine and guanine with three hydrogen bonds, respectively. For this, the genetic code is unique. The genetic information is read *via* specific enzymes that bind to the DNA. These enzymes, e.g. polymerases, bind to specific regions at the DNA and translate the DNA sequence into the aminoacids sequence of the protein of interest [80]. There are complex regulatory mechanisms that control the production of proteins or the inhibition of production, either. Diseases can occur, if the regulatory mechanisms are disturbed, as for cancer.

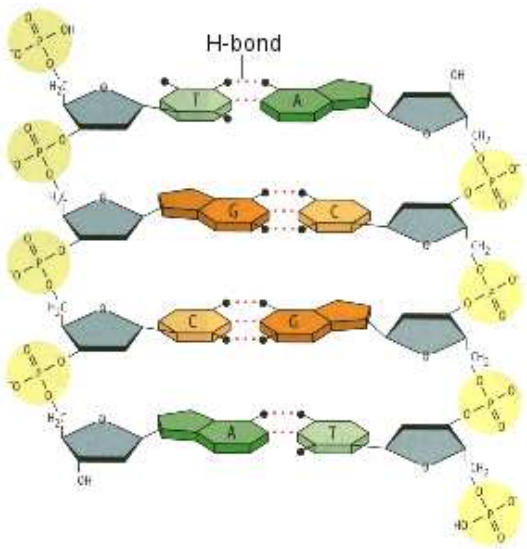

Figure 2.1: *Chemical structure of DNA. The backbone is built by sugar and phosphate while adenine (A) and thymine(T), and cytosine (C) and guanine (G) form the treads, respectively [80].*

The complementary binding of the nucleotides results a formation of a double helix with two

anti-parallel strands, winding around a common axis. Hydrophobic interactions stabilize the helical structure. The double helix structure forms a minor and a major groove. The grooves serve as recognition sites for several DNA-binding proteins [81, 82]. The periodicity of the helical structure is about 3.4 nm and spans over 10 bases. In diameter, the DNA is about 2 nm [80]. The helical conformation of the DNA is specified by the base sequence. In physiological solution the most often form is the B-form, a right-handed double helix with a standard distance of 0.34 nm of adjacent bases (see figure 2.2).

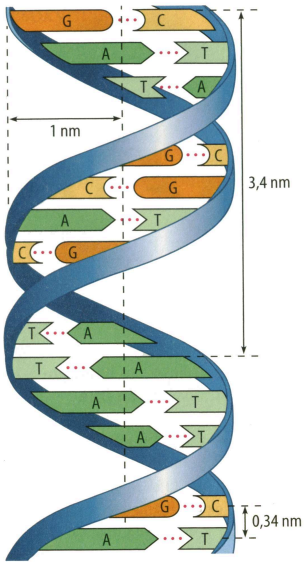

Figure 2.2: *DNA with helical structure. The width of the strand is about 2 nm. A fully twist of the strand is completed after 10 base pairs, 3.4 nm [80].*

In aqueous solution at neutral pH, the DNA backbone, more precisely the phosphate group, carries one negative charge per nucleotide. For this, the DNA can be regarded as polyelectrolyte that is surrounded by counterions of the surrounding solution (see section 2.3.2). The electric properties of the DNA become important for the separation processes investigated in this work. The electrokinetic mobility (see section 2.3.3) as well as the polarizability of the DNA molecule depend on the ion cloud (see section 2.3.4).

Possible conformations of DNA molecules are linear and circular. For bacterial DNA, also called plasmid DNA, the circular form is the most present. Genome DNA of higher organisms is mostly linear. The DNA of complex organisms is quite long (e.g. human genome with about 2 m within each cell). As a consequence, storage as random coil in the cell nucleus is impossible. Thus, the DNA strands are highly packed with structure proteins like histones [80].

For the circular form of DNA, there are two conformations to be distinguish. First, the circular form with its intrinsic number of helical turns, so called relaxed or open circle

(oc) form. When twisting or untwisting the linear DNA strand before covalently closing to the ring form, the ring forms a super helix, called the covalently closed circular (ccc) form. The supercoiled/ccc-form is of high biological and medical interest due to its ability to infiltrate cells, e.g. for plasmid vaccination or gene-therapy [23].

One special supercoiled DNA used in this work was the *minicircle* DNA. *Minicircle* DNA is defined to contain almost exclusively the "Gene of interest" and its regulating sequence motifs without bacterial backbone sequences [23]. Usually, the "Gene of interest" is inserted in a bacterial plasmid and duplicated along the bacterial cell cycle. For detection of infected bacterial cells often an antibiotics resistance is in the inserted sequence, too. When using such a plasmid for vaccination or gene therapy, the patient gets the bacterial DNA and the antibiotics resistance, which is a huge problem. Hence, *minicircle* DNA becomes important for gene-therapy or plasmid vaccination. For production of *minicircle* DNA the "Gene of interest" and a gene of antibiotics resistance is inserted in bacterial DNA, forming so-called parental DNA (see figure 2.3). After an inducible, sequence specific, in-vivo recombination process the *minicircle*-DNA is purified *via* an affinity-based chromatography [23].

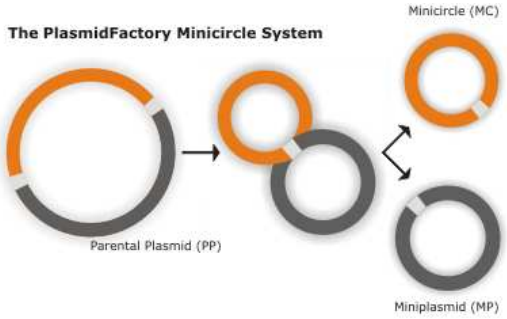

Figure 2.3: *Production of minicircle DNA. The parental plasmid carries a selection marker, the origin of replication, two recombination sites and the "Gene of interest". The recombination of parental DNA results in two circular, supercoiled molecules (miniplasmid and minicircle). The miniplasmid contains the selection marker, the ori, and bacterial sequences. The minicircle contains hardly more than the "Gene of interest" and all necessary elements for regulation in the target cells [83].*

2.1.1 Statistical description

Biopolymers can be described by statistical models, as *freely-jointed-chain* (FJC), *freely-rotating-chain* (FRC) or *worm-like-chain model* (WLC). FJC and FRC describe a polymer as an ideal chain with stiff segments. Whereas in FJC the segments are freely jointed, without any restrictions in rotation, in the FRC model the rotation is somewhat reduced in freedom, based on restricted angle of rotation. In contrast to these two models, the WLC model assumes the polymer as a single continuous, flexible cylinder, without segments. This

model is best suited for polymers that can be described with certain stiffness, like DNA. The persistence length defines the length on which the polymer can be assumed as a stick.

From the models above, the WLC model describes the DNA best. When the contour length L becomes large ($L \ll l_p$) the DNA molecule can be described as a random walk of a chain with segments of Kuhn length $l_{Kuhn} = 2l_p$. The average end-to-end distance $r_{end-to-end}$ and the radius of gyration r_G are related by [84]

$$r_{end-to-end} = \sqrt{6} r_G = l_{Kuhn} L^2 \quad . \tag{2.1}$$

The radius of gyration is defined as the distance between the axis of a rotating body and its center of gyration. The radius of gyration is related to the hydrodynamic radius r_H [85],

$$r_G = 1.51 \cdot r_H \quad . \tag{2.2}$$

Up to now, the excluded volume was not considered. It describes the effect that two monomers cannot be at the same place at same time. As a consequence, the radius of gyration becomes larger. When describing the DNA statistically, two forces are mainly acting on the DNA molecule, 1) entropic forces that tend to minimize the radius, 2) repulsion forces that enlarge the radius. In equilibrium the radius scales with the number of basepairs N

$$r_{G,WLC} \propto N^{\nu} \quad , \tag{2.3}$$

with ν the Flory exponent, that depends on the dimensionality d, the describing model and, especially, the excluded volume effect. For repulsive forces it is defined as $\nu \simeq \frac{3}{d+2}$. In 3 dimensions, the Flory exponent is 0.5 without excluded volume and 0.588 with appreciable excluded volume effects.

It is often assumed that the effective radius of DNA molecules additionally depends on screening ions of the ion cloud, i.e. the solvent. The characteristic parameter to describe the ion cloud is the Debye length (see section 2.3.2). It determines the electrostatic repulsion of the segments. Consequently, the radius and the persistence length scale with the ionic strength of the solvent. Under physiological conditions, the persistence length of double stranded DNA is about 50 nm [86].

2.1.2 Fluorescence labeling of DNA

According to Abbès formula for the diffractive limit $R = \frac{\lambda}{2NA}$ [87] is given with R object size, λ wavelength and NA numerical aperture of microscope. Thus, objects that are smaller than half of the wavelength of incident light, are not detectable with classical light microscopes. All analytes used in this work were below this limit. Hence, for all experiments the objects, (DNA, nanobeads, and proteins) were fluorescently labeled to overcome the diffraction limit.

Generally, fluorescence (F) is an effect of electron excitation and relaxation with light emission. First, the dye molecule absorbs a photon by exciting one electron into a higher

energy level (see figure 2.4). After a characteristic time of about 10^{-8} s, the electron relaxes to the ground state emitting a photon. In the excited state energy loss occurs without radiation, e.g. rotational relaxation or collisions with other molecules near by (internal conversion (IC)). The energy loss leads to reduced energy of the emitted photon, the so-called red shift or Stokes-shift [88]. By using dichroic mirrors, emitted photons can be selectively detected (see also section 3.4).

Beyond fluorescence, several other relaxation processes are possible. Phosphorescence is one of the relaxation pathways that might reduce the fluorescence efficiency. The phosphorescence (P) is an intersystem crossing (ISC) effect between the singlet state (S_1) and the triplet state (T_1). Since this is quantum mechanically forbidden, the lifetime is much longer than for fluorescence. Another relaxation process is the photo induced chemical reaction (PIC). All these effects can lead to quenching and reduced fluorescence intensity [88].

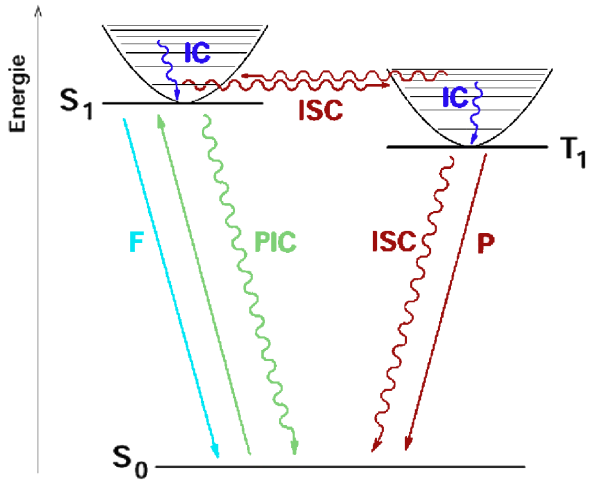

Figure 2.4: *Jablonski diagram. The system is excited from the ground state S_0 to first excited state S_1 by absorption of a photon, several pathways of relaxation are possible (see main text) indicated by the arrows.*

In this work the intercalator YOYO-1 [1] was used for fluorescent labeling of DNA. YOYO-1 is built by planar aromatic rings that are four times positively charged (see figure 2.5). The structure allows intercalation between two base pairs with a very high binding constant of $6 \cdot 10^8$ Mol^{-1} [89]. When YOYO-1 intercalates between two base pairs the conformation of the dye changes, resulting in a significant increased quantum yield by a factor of 410 compared to the free molecule [90].

[1] 11,1-(4,4,7,7-tetramethyl-4,7diazaundecamethylene)-bis-4-[3-methyl-2,3-dihydro-(benzo-1,3-oxazol)-2-methylidene]-quinoliumtetraiodid

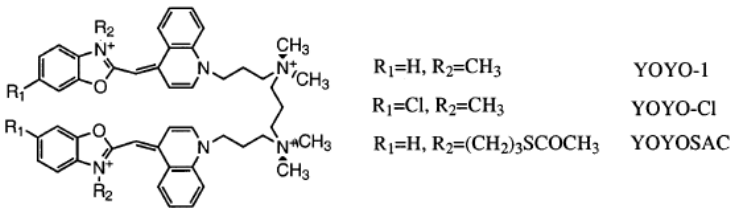

Figure 2.5: *Chemical structure of YOYO-1. The planar rings (positively charged) intercalate between two base pairs (negatively charged backbone) [91].*

2.1.3 Protein-DNA and drug-DNA complexes

As already mentioned in section 2.1 diseases may occur if the regulatory mechanisms of DNA transcription are defect or when proteins bind to DNA inhibiting the transcription. In this context, the investigations as well as the detection of DNA complexes with proteins or drugs are of great interest in medicine. On the one hand for screening methods, like the detection of anti double-stranded DNA antibodies, specific for *systemic lupus erythematosus* [92]. On the other hand, for binding interaction studies as for rational drug design [21]. In this work, two different types of complexes were investigated. The first complex was a drug-DNA complex and the second complex was a protein-DNA complex.

For the drug-DNA-complex, Actinomycin D (ACTD) was used because of its special interest in cancer and HIV therapy. It binds to the DNA, thus blocks the assembly of proteins to the DNA, and stops cell proliferation [93]. It consists of a phenoxazone ringsystem, bound to two cyclic pentapeptides (see figure 2.6) [94]. These are built of threonine (conjunction to phenoxazone), d-alanine, proline, sarcosine, and methyl-valine, respectively. An ester-bound closes the ring to lactone. The aromatic ringsystem intercalates unspecific in the DNA with a binding constant of 10^6 Mol^{-1} [95]. After the intercalation of ACTD to DNA, the shape of the DNA-molecule is changed a bit to a slightly bended and unwound form [81]. Additionally, the net charge of the DNA-complex changes. As a consequence, the electrophoretic mobility changes. Furlan et al. could detect a shift between DNA/ACTD-complexes and DNA by EMSA (see section 3.1.2) [96].

The protein-DNA complex, used in this thesis, was with *Escherichia coli (E.coli)* RNA polymerase core enzyme (RNAP). Polymerases bind to the DNA due to protein synthesis, according to the base sequence [80]. RNA polymerase for example synthesizes RNA. The *E.coli* core enzyme consists of three subunits (see figure 2.7) with molecular mass of 389 kDa [97]. When the polymerase binds to the DNA the DNA strand is strongly bend, thus the conformation of the DNA changes [98]. Due to the charged groups, the polymerase also changes the net charge of the DNA molecule. Both of these effects results in altered electrokinetic mobilities, observed in EMSA experiments [99, 100].

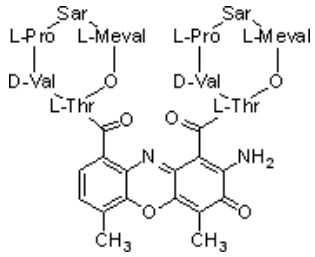

Figure 2.6: *Chemical structure of Actinomycin D. The planar rings can intercalate between two base pairs [94].*

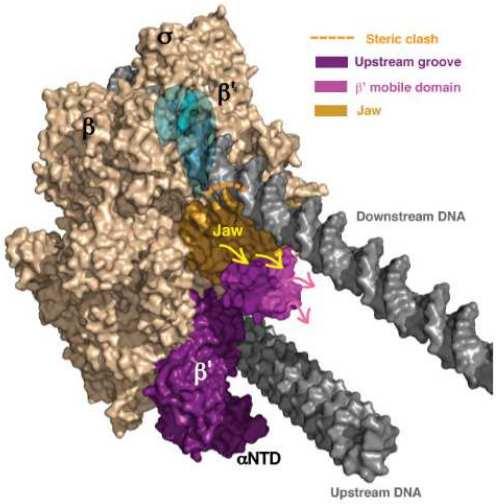

Figure 2.7: *DNA polymerase complex. The E. coli RNA polymerase consists of three subunits [97].*

2.2 Gelelectrophoresis and electrophoretic mobility shift assays

The new technique of dielectrophoretic separation of DNA and DNA complexes presented in this work is compared to well-established techniques of gel electrophoresis and electrophoretic mobility shift assays (EMSA). In gelelectrophoresis two separation criteria are possible, either the size of the analyte [41, 84, 101] or the conformation [102].

When describing the separation mechanism the gel is assumed to be a porous media and the analyte (here DNA) to be small and a hard sphere [41]. The specific ratio between the free mobility of the analyte and mobility in the separation matrix depends on the available volume of the particle (with respect to the molecules size and the concentration of the gel) [103]. There are three different regions for migration within a porous material [84]: 1) the Ogston limit, for analyte of diameter smaller than average pore size, 2) the reptation regime, for analyte of diameter larger than most of the pores, 3) the biased reptation with molecular alignment.

In this work, 1.2% agarose gel was used, with pore size of 100 nm to 200 nm. Thus, for DNA of size 2.0 kbp to 7.0 kbp, as used in this thesis, the migration mechanism was in the reptation regime.

Depending on the pore size and the analyte size, the electrophoretic mobility significantly alters (see figure 2.8). Generally, DNA with larger diameter migrates more slowly than smaller DNA.

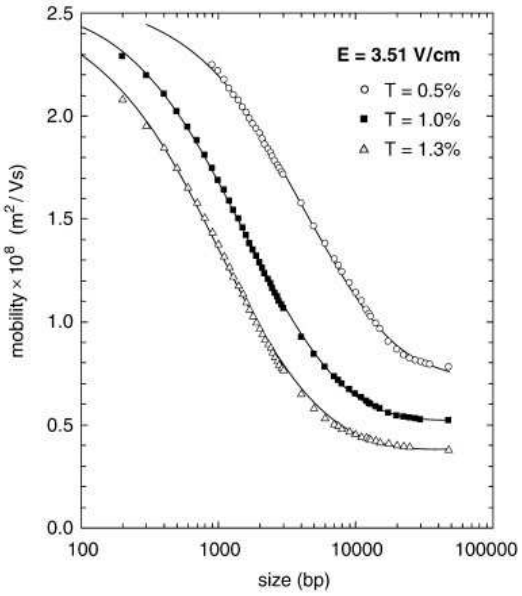

Figure 2.8: *Dependence of size of DNA versus mobility for different concentrations of agarose gel [41].*

DNA-complex formation can be detected *via* gel electrophoresis, by so-called electrophoretic mobility shift assay (EMSA). The electrophoretic mobility is altered by change in analyte size and/or in analyte conformation [104]. Thus, a shift between DNA and DNA-complexes occur due to the different migration velocities. The typical runtime of gelelectrophoresis is 3 h. Hence, the investigated analyte has to be stable for at least a few hours [104–109].

To characterize the separation, the resolution can be calculated by [110],

$$Res = \frac{x_1 - x_2}{2 \cdot (\sigma_1 + \sigma_2)} \quad , \tag{2.4}$$

with $x_{1,2}$ positions of bands and $\sigma_{1,2}$ widths of bands. The resolution of gelelectrophoresis depends on the gel (pore size and running buffer), the separation time, and the analytes.

2.3 Electrokinetics and hydrodynamics

For all chip experiments, as well as the gel electrophoresis, electric fields or hydrostatic pressures were used to drive the molecules. Due to the small volumes of the microfluidic devices, other effects dominate the flow than in the macroscopic regime. In the next sections, the basics of electrokinetics and hydrodynamics on the micrometer-scale are presented.

2.3.1 Scaling laws and hydrodynamics on the μm-scale

When scaling down a system to microscopic dimensions, effects known from macroscopics become negligible (mass, gravity), whereas other effects become dominant (surface, viscosity, diffusion) and some new effects occur (new transport mechanisms) [7, 111]. Most of them are based on the surface to volume ratio $r_{S,V}$

$$r_{S,V} \propto \frac{a^2}{a^3} \quad , \tag{2.5}$$

with a characteristic length, for example diameter of capillaries or channels. From this equation, it is clear that the surfaces become more important for smaller devices. In the chip experiments, typical lengths are at micrometer scale (few micrometers in height and hundreds of micrometer in width). Thus, surface effects are very important when describing migration in microfluidic channels.

One dimensionless number to characterize fluid flows is the Reynolds number R_η [111]. It is defined as ratio of inertia and viscous forces and allows a prediction whether the flow is laminar or turbulent [112],

$$R_\eta = \frac{\rho v a}{\eta} \quad . \tag{2.6}$$

With ρ density of fluid, v velocity, and η dynamic viscosity of fluid. Laminar flow is observed for Reynolds numbers below 2300 [113]. To calculate the Reynolds number for

rectangular channel geometries the hydraulic diameter, $d_h = \frac{2bh}{b+h}$, with h and b channel height and width [114], is used. According to channel dimensions, Reynolds numbers for microfluidic devices are typically smaller than 1. Laminar flow or simply Stokes flow is generally accepted for microscale devices [111]. Thus, for mixing in microfluidic devices stirring does not work [54], and diffusion becomes predominant (see also section 2.5).

2.3.2 The electrical double layer

All chip experiments were performed in poly(dimethylsiloxane) (PDMS) devices with aqueous solutions (see section 3.3). SiOH-groups are formed at PDMS surfaces and are negatively charged in aqueous solutions at about pH 7 [39].

Charged surfaces are shielded by counter ions and appear (at distance) electrically neutral. The ion distribution at the surface is referred to as electrical double layer (EDL). The first layer, next to the surface, is called the Stern-layer. In the Stern-layer the counter ions are assumed to be immobilized at the surface. The characteristic length is estimated by the Bjerrum-length and about the thickness of single ions [115]. The Stern-layer is followed by the diffusive or Gouy-Chapman-layer. Within that layer, the electrostatic attraction of the surface charge is weakened so that the ions can diffuse [116].

To calculate the electric surface potential, with respect to distance to channel wall, the ions distribution can be described by the Boltzmann equation [117],

$$n_{\pm} = n_0 exp\left(\pm\frac{e\psi(r)}{k_B T}\right) \quad , \tag{2.7}$$

with $n_{\pm}$ ion number densities, n_0 bulk concentration of salt, e electron charge, $\psi(r)$ external field at position r and $k_B T$ thermal energy. Furthermore, ψ is equal to the average field established by the ions. This leads to the nonlinear Poisson-Boltzmann equation [118],

$$-\nabla^2\psi = \frac{e}{\epsilon_m}\sum_i c_i z_i exp\left[\frac{-z_i e\psi}{k_B T}\right] \quad . \tag{2.8}$$

ϵ_m is the permittivity of the fluid, c_i and z_i are concentration and valency of i-th ion.

Under the assumption that the thermal energy is much smaller than the potential energy of the external field ($e\psi \gg k_B T$), equation (2.8) can be linearized (Debye-Hückel-theory). For the linearized equation (2.8) the characteristic length of the electrical double layer, Debye length λ_D, can be calculated to

$$\lambda_D = \sqrt{\frac{\epsilon k_B T}{\sum_i N A c_i z_i^2 e^2}} \quad . \tag{2.9}$$

λ_D is the characteristic length scale over which the potential is decreased to 1/e of the surface potential. At the Debye length the attractive potential of the surface charges and

entropic repulsion of ions are equal [119]. As a rule of thumb the Debye length can be estimated by $\lambda_D[nm] \simeq 9.6/\sqrt{cz}$ with c in [mM], for a symmetric electrolyte in water at 298 K [120].

In figure 2.9 the electric double layer and the resulting potential are depicted. Although the Stern-layer and the Gouy-Chapman-layer are combined in the electrical double layer, the electric potential decay is different. So for the Stern-layer the potential decreases linearly, whereas in the diffusive layer the decay is exponentially [115, 121]. The potential at the interface of these two regions is called ζ-potential.

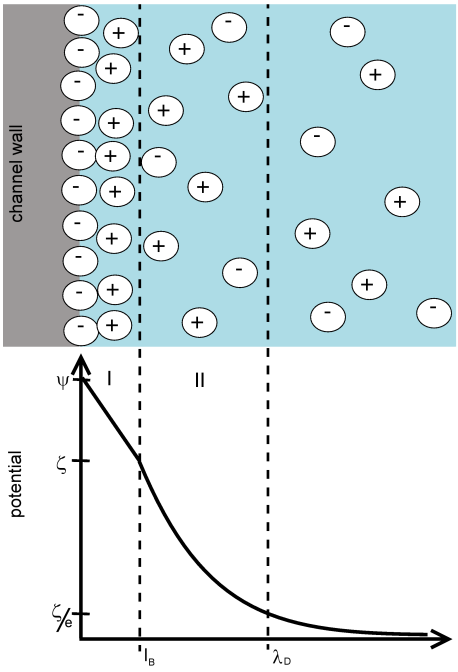

Figure 2.9: *Electrical double layer at negatively charged surface and resulting potential. Region I is the Stern-layer, the potential decays linearly. Region II is defined as diffusive or Gouy-Chapman-layer with exponentially decay of potential. l_B and λ_D are Bjerrum and Debye length.*

2.3.3 Electrophoresis and electroosmosis

The analytes were driven in chip experiments either by external electric fields or by hydrodynamic pressures, applied to the microfluidic channel. When electric fields are applied to charged objects or electrolyte solutions, mainly two phenomena can be observed: 1) electroosmotic flow and 2) electrophoresis.

Electroosmotic flow is based on the electric double layer that occurs at charged surfaces (see section 2.3.2). If an electric field is applied tangentially to the charged surface, the ions within the electrical double layer start to migrate. Due to viscous drag forces the

molecules outside the electrical double layer follow the migration and a flow over the whole channel width occurs [115, 121]. This induced electroosmotic flow yields some advantages for analytes transport, like the plug like flow profile (see figure 2.10).

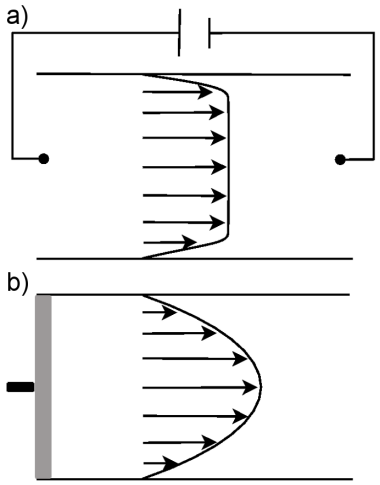

Figure 2.10: *Flow profiles. a) Electroosmotic flow profile. Electric voltages are applied to the channel that drive ions and consequently the whole buffer. b) Hydrostatic flow profile. Hydrostatic pressures are applied to the channel that drive the solution.*

The electroosmotic mobility μ_{eo}, characterizes the electroosmotic flow by the ratio of electroosmotic velocity v_{eo} and applied electric field E $\mu_{eo} = \frac{v_{eo}}{E}$. μ_{eo} can be calculated if the following boundary conditions are fulfilled: the surface exhibits a no-slip condition, i.e. the velocity at solid-liquid interface equals zero; the electrical double layer is small relative to the characteristic length, i.e. $\lambda_D \ll h$; the electric field E is constant over the whole channel; the flow is stationary. Then the electroosmotic mobility is given by [121],

$$\mu_{eo} = -\frac{\epsilon_0 \epsilon_m \zeta}{\eta} \quad . \tag{2.10}$$

This formula is known as Helmholz-Schmoluchowski equation.

The second electrokinetic phenomenon, electrophoresis, describes the migration of a charged object, with surface potential ζ, relative to a stationary liquid by an applied electric field. The electrophoretic mobility of the charged object can be obtained from the electroosmotic mobility by just changing the frame of reference. It calls [115],

$$\mu_{ep} = +\frac{\epsilon_0 \epsilon_m \zeta}{\eta} \quad . \tag{2.11}$$

This property is also called the similitude of electrophoresis and electroosmosis [71]. The similitude is true if the above mentioned boundary conditions are fulfilled. For all performed chip experiments the boundary conditions were fulfilled, so the electroosmotic and

electrophoretic motion of charged objects can be described by equation (2.10) and equation (2.11).

From equation (2.11) it becomes clear that the electrophoretic mobility is independent of object size and shape, and only depends on surface potential. This is important especially for the separation of DNA molecules. Since the surface potential of DNA molecules is independent of the molecules size, a length independent migration occurs in free solution [42, 84].

2.3.4 Dielectrophoresis

Dielectrophoresis is described as the migration of a polarizable particle in an inhomogeneous electric field. This offers the possibility that particles with no net charge can be manipulated *via* electric fields, offering new applications in separation science. The polarizability is influenced by the material, the size, and the surrounding of a particle. Thus, dielectrophoresis can be exploited to distinguish analytes with respect to these parameters. Dielectrophoresis is used to selectively manipulate or separate analytes, like DNA [122–129], proteins [130–132], cells [133–143], (nano)beads [56, 58, 66, 75, 78, 144, 145] or carbon nano tubes [146, 147].

There are two established techniques to generate the necessary inhomogeneous electric fields (figure 2.11). 1) Microelectrodes are placed inside the microchannel. 2) The microchannel is structured with insulating posts or hurdles, usually referred to as insulating or electrodeless dielectrophoresis (eDEP) [43, 148]. In this thesis, the latter route is pursued, because the electrodeless dielectrophoresis lacks of electrochemical effects at the region of manipulation, allows easy fabrication processes and yields homogeneous electric fields over the full channel height [43–45, 47].

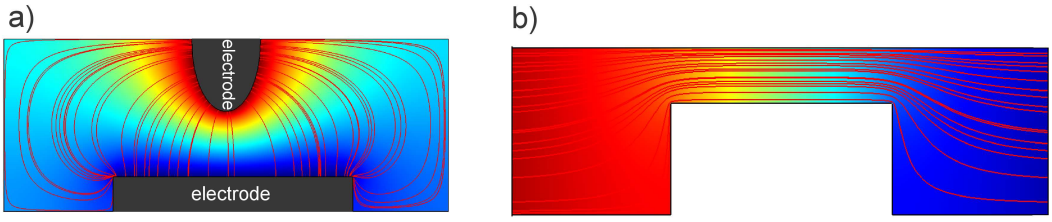

Figure 2.11: *Established techniques for dielectrophoresis with electrodes a) and insulator based b). The electric field lines are depicted in red, the strength of the electric potential is color-coded. According to the technique, the electric field decays with respect to distance to upper electrode as for DEP a). Whereas for eDEP the electric field is homogeneous over the whole channel height for b).*

The dielectrophoretic force is given by [149],

$$\vec{F}_{DEP} = \vec{p}\nabla\vec{E} \tag{2.12}$$

with $\vec{p}$ dipole moment of particle and $\vec{E}$ electric field. In literature, the dielectrophoretic force is mostly written in a different form that depicts the influences of the particles radius a and material (*via* permittivity ϵ_p), the surrounding medium (*via* permittivity ϵ_m) and the frequency dependence *via* the Clausius-Mosotti factor ($CM = \frac{\tilde{\epsilon}_p - \tilde{\epsilon}_m}{\tilde{\epsilon}_p + 2\tilde{\epsilon}_m}$, $\tilde{\epsilon}_{p,m}$ are the complex permittivities of particle and medium) factor [75, 150–154],

$$\vec{F}_{DEP} = 2\pi a^3 \epsilon_m \Re[CM] \left(\nabla \vec{E}^2\right) \quad . \tag{2.13}$$

For equation (2.13) it is assumed that the polarizability is solely dominated by the material. The ion cloud is neglected.

Via the Clausius-Mosotti factor the direction of dielectrophoretic force is defined, i.e. if the permittivity of the particle exceeds the permittivity of the medium, particles are attracted by regions of higher electric fields (positive dielectrophoresis) and *vice versa*a (negative dielectrophoresis). Here, the experiments are performed with DNA or polystyrene beads. DNA exhibits most often positive DEP [47, 65, 122, 123, 125, 154–157]. Polystyrene beads exhibit negative DEP [56, 66, 134, 144].

For equation (2.13) the definition of the dipole moment

$$\vec{p} = \alpha(\omega)\vec{E} \tag{2.14}$$

is used with $\alpha(\omega)$ frequency dependent polarizability. The polarizability can be calculated for the following assumptions: 1) the particle is a homogeneous dielectric particle with ohmic conductance but no dielectric loss. 2) It is spherical. 3) The frequency is in the low frequency range, i.e. the time constant of electric field is larger than the time needed for the charges to accumulate at the surface of the particle [158]. Then the polarization processes are dominated by charge transport and the Clausius-Mosotti factor becomes [45]

$$CM_{cond} = \frac{\sigma_p - \sigma_f}{\sigma_p + 2\sigma_f} \quad , \tag{2.15}$$

with σ_p conductivity of particle and σ_f conductivity of fluid. In the low frequency range, the dipole moment of a particle is given by [159]

$$\vec{p} = 2\pi\epsilon_m \Re[CM_{cond}] a^3 \vec{E} \quad . \tag{2.16}$$

For the polystyrene beads, the assumptions are valid, whereas the DNA molecules are no homogeneous dielectric particles. Hence, the exact polarizability of DNA cannot be calculated with equation (2.16). But the polarizability may be estimated since it scales with the Flory exponent [125].

The dielectrophoretic potential is written by $W_{DEP} = -\vec{p}\vec{E}$. When applying an alternating electric field $\vec{E}(t) = sin(\omega t)\vec{E}$, and with equation (2.14) the time-averaged dielectrophoretic potential can be written as

$$W_{DEP} = -\frac{1}{2}\alpha\vec{E}^2 \quad . \tag{2.17}$$

The inhomogeneous electric field is created at an insulating ridge that reduces the channel height. The resulting dielectrophoretic potential landscape is depicted in figure 2.12. It is obvious, that the dielectrophoretic potential significantly changes in the vicinity of the nanoslit. Here, two cases have to be distinguished: positive and negative dielectrophoresis. If the analyte exhibits a positive polarizability, the dielectrophoretic potential is reduced within the nanoslit with local minima at the edges of the ridge. As a consequence, particles with positive polarizability will be trapped on top of the ridge, where the dielectrophoretic potential can be approximated as a well. In the case *vice versa*, negative polarizability, the particles will be trapped before the ridge, since the dielectrophoretic potential forms a hurdle to these particles. Even when the shape of the resulting potential is different, well or hurdle, the escape process out of the potential well or over the potential hurdle is similar (see section 2.6).

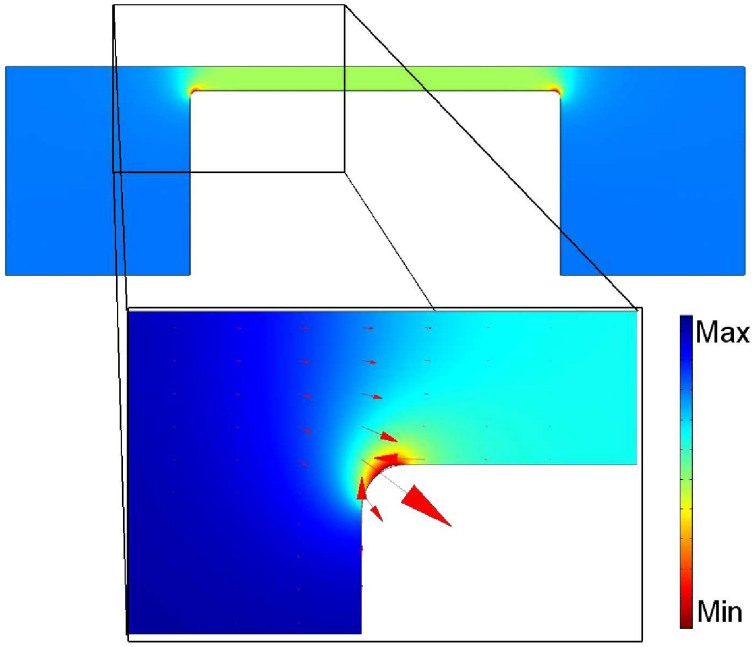

Figure 2.12: *Numerical simulation of dielectrophoretic potential ($W_{DEP} \propto \vec{E}^2$) at the nanoslit in cross-sectional view. The color code indicates the magnitude of the potential energy in arbitrary units. Potential minima occur at the edges for $\alpha > 0$ (DNA), the arrows indicate the direction of the resulting dielectrophoretic force. In case of $\alpha < 0$ at the edges were potential maxima (polystyrene beads).*

Since the dielectrophoretic potential is proportional to the polarizability, the particles manipulated *via* dielectrophoresis must be sufficiently polarizable. The polarizability of polystyrene beads is mainly understood [160]. For DNA the polarization effect is still not completely known [161]. It is assumed, that the major part of the polarizability of DNA stems from the induced dipole of the surrounding ion cloud [65, 155, 161, 162]. As described in section 2.3.2, charged objects are shielded by counter ions and seem uncharged in the absence of an electric field. However, when an electric field is applied the counter ions are moved by the shear of fluid movement. This leads to increased net charge density along the DNA strand, whereas the counter ion charge distribution becomes polarized (see figure 2.13).

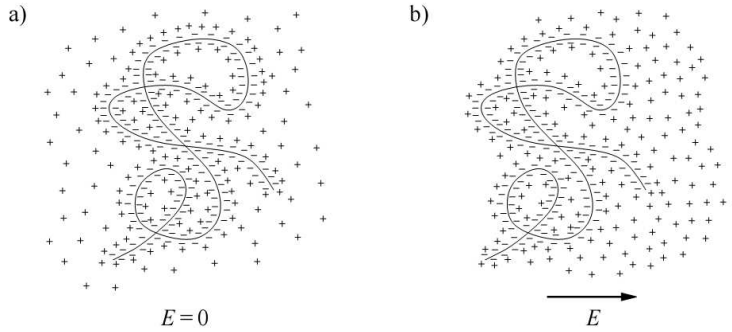

Figure 2.13: *Scheme of DNA ion cloud polarization for large λ_D. a) In absence of an electric field the DNA is completely shielded by counter ions. b) In presence of an electric field $\vec{E}$ the ion cloud is shifted along the DNA, thus a dipole moment is induced.*

In several experiments, a correlation between viscosity of fluid [155], ionic strength [122, 126, 161–164], surfactants [165] or frequency of electric field [79, 155] and dielectrophoretic force was observed. For DNA the dielectrophoretic force decreases with increasing viscosity of fluid [155]. In the ion cloud model, an increased viscosity would reduce the polarizability and accordingly the dielectrophoretic force would decrease. Concerning the ionic strength the electrical double layer is directly influenced. For an increased ionic strength the thickness of the Debye layer decreases, at the same time the polarizability decreases [122, 126, 161, 162]. Hence, the ion cloud model seems plausible for DNA.

The dipole formation and alignment process require a finite time [166]. For ac dielectrophoresis, the ion cloud migrates along the DNA strand. Every time the electric field alters, it changes its direction. As a consequence, the available time for migration along the DNA strand is set by the frequency. This effect was observed by several groups over a wide range of frequencies ($10^{-1} - 10^{7}\,Hz$) [122, 133, 155, 166, 167]. In the low-frequency region, up to few kilohertz the ions are able to follow the electric field. In that region, the polarizability depends primarily on the DNA size [166], whereas for higher frequencies the time is too short for migration of the ion cloud. In the high frequency range, the frequency dependency

is based on fluctuations in the double layer [166]. However, in this work the frequencies were in the low frequency region. In this region, additional effects occur and complicate the quantitative analysis of the polarizability. Generally, fluid motions by hydrodynamics or electroosmosis influence the ion distribution along the DNA molecule. Additionally, the electrophoretic motion of the DNA itself complicates the exact quantitative analysis of the polarizability.

Since the dielectrophoretic force scales cubically with the particles radius (equation (2.13)), separation of particles of same material but different size can be explained [66, 69]. Additionally it becomes clear that for smaller objects, like nanobeads or proteins, it is more difficult to generate dielectrophoretic forces to sufficiently manipulate objects of a few nanometer size. The necessary dielectrophoretic potential/forces can be estimated if the polarizability of the object of interest is known or, at least, could be estimated by equation (2.17) [43].

2.4 Intermolecular interactions

The objects used in the experiments were negatively charged DNA (see section 2.1) or carboxylated surface of nano beads (see section 3.3), so repulsive forces occur between the particles that can be described by Coulomb interactions. Additionally, the charges are shielded by counter ions. Hence, the resulting interaction potential can be written by the Derjagui-Landau-Verwey-Overbeek (DLVO) potential [168]

$$V_{DLVO}(r) = \left(\frac{Qexp(\kappa R)}{1+\kappa R}\right)^2 \frac{exp(-\kappa r)}{\epsilon r} \quad . \tag{2.18}$$

With r distance between two charged colloids, Q the charge of the colloid (without effects of solvent molecules), R the hard core radius of colloid and $\kappa = 1/\lambda_D$. From equation (2.18) it becomes clear that the DLVO potential decays exponentially. As already mentioned in section 2.3.2 the Debye length characterizes the length for an exponential decay of a surface potential. For buffer of 1 mM concentration, as used for all dielectrophoresis experiments, the Debye length is about 3 nm. Thus, the interactions between the beads or DNA can be assumed as hard ball interactions (see also section 4.3).

2.5 Brownian motion and diffusion

Diffusion is the (random) thermal motion of particles, firstly described by the Botanist Brown for pollen. The origin of the motion is permanent collisions with molecules of the surrounding medium.

As already mentioned in section 2.3.1, diffusion becomes important on the micrometer scale. For example, a 100 μm particle moves 2 $\mu m^2/s$ by diffusion at room temperature [8].

The diffusion can be characterized by the diffusion coefficient D that is defined as follows [169],

$$D := \lim_{t\to\infty} \frac{<\vec{x}(t)^2> - <\vec{x}(t)>^2}{2dt} \quad . \tag{2.19}$$

With $x(t)$ position of particle at time t, $< \cdot >$ denotes the ensemble average. Without external forces $<\vec{x}(t)>^2 = 0$.

In 1905, Einstein was able to explain the Brownian motion by the molecular kinetic theory of heat [170]. He derived the diffusion coefficient as solely temperature dependent with

$$D = \frac{k_B T}{6\pi\eta r_{particle}} \quad . \tag{2.20}$$

Accordingly, the radius of a particle $r_{particle}$ can be determined from the diffusion coefficient for known temperature and fluid viscosity. Especially for DNA the diffusion coefficient allows determination of the hydrodynamic radius and so the radius of gyration (see section 2.1.1).

2.6 Kramers rate and first mean passage time

Molecular reactions like binding or folding events as well as the escape of trapped molecules out of a metastable potential well (see figure 2.14) can be described by the Kramers rate.

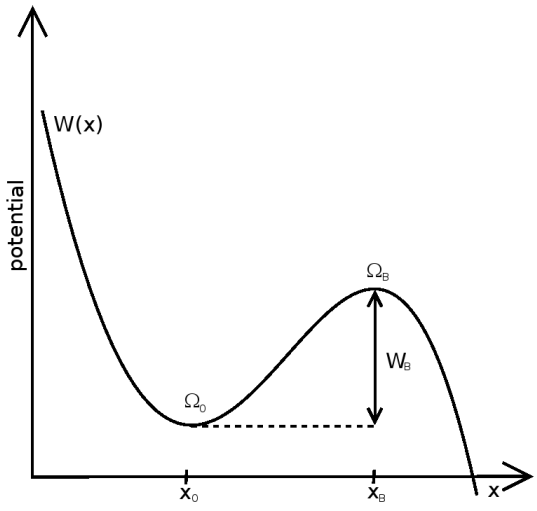

Figure 2.14: *Potential landscape for molecular reactions and escape processes.*

Therefore, the potential $W(x)$ is approximated piecewise as harmonic potential and is

described by [171]

$$W(x) - W(x_0) = \begin{cases} \frac{1}{2}\Omega_0^2(x - x_0)^2 & for\ x \approx x_0 \\ W_B - \frac{1}{2}\Omega_0^2(x - x_B)^2 & for\ x \approx x_B \end{cases} \quad . \tag{2.21}$$

With x_0 the starting position of the particle, x_B local maximum of the potential, $\Omega_{0,B}$ curvatures of potential at x_0 and x_B, i.e. the second derivatives of the potential $\frac{\partial^2 W(x)}{\partial x^2}$. It is assumed, that the particle is much smaller than the dimensions of the potential, i.e. the particle does not see changes in the potential landscape. With an overdamped Langevin equation, the dynamics of the particle can be described [171, 172]. This becomes important for simulation of the separation processes (see section 4.3).

Due to Brownian motion, the particle can escape out of the potential [169]. Even when the thermal motion is a stochastic process the mean escape behavior is characterized by the so called Kramers rate $k_{Kramers}$ and depends on the thermal energy $k_B T$ and the shape of the potential $\frac{|\Omega_0 \Omega_B|}{2\pi f}$

$$k_{Kramers} = \frac{|\Omega_0 \Omega_B|}{2\pi f} exp\left(-\frac{W_B}{k_B T}\right) \quad . \tag{2.22}$$

The inverse of the Kramers rate is equivalent to the first mean passage time [173]. The first mean passage time is the average of N independent realizations of a particle starting within the potential well and escape due to thermal activation. Thus, it corresponds to the lifetime within the potential well, hence to the time the particle is trapped (trapping time). So, the trapping time is defined as

$$\tau = \frac{1}{k_{Kramers}} = \frac{2\pi f}{|\Omega_0 \Omega_B|} exp\left(\frac{W_B}{k_B T}\right) \quad . \tag{2.23}$$

Adopted to dielectrophoretic trapping the Kramers rate can be simplified as

$$\tau \propto exp\left(\frac{\Delta W - \Delta W_{dc}}{k_B T}\right) \quad , \tag{2.24}$$

where $(\Delta W - \Delta W_{dc})$ denotes the dielectrophoretic potential barrier reduced due to additional superimposed potentials (static voltages U_{dc}, see section 3.5).

3 Materials and methods

3.1 Biomolecular methods

3.1.1 Reproduction and extraction of DNA

For the experiments, linear as well as circular DNA molecules of different lengths were used. One species, the linear 2.686 kbp DNA, was custom made. Briefly, pUC 18 vector DNA was cloned with *Escherichia coli* (*E.coli*) cells, isolated and linearized with Nde*I*.

Transfected *E. coli* cells, containing the pUC 18 vector, were raised in LB medium[2] with ampicillin at 37 °C in a wobble incubator at 300 rpm and cultivated over night. Next day, the cells were centrifuged at 3200xg[3] for 5 min.

Afterwards the DNA was isolated with the QIAprep Miniprep Kit (Qiagen, USA) according to supplier's information. The bacteria were lysed with a proteinase and the DNA was bound via centrifugation to the column. Impurities were removed during washing steps and the DNA was eluted with 50 μl EB buffer (10 mM Tris Cl, pH 8.5). A DNA concentration of 295 $ng/\mu l$ was determined *via* UV-VIS spectroscopy. For linearization, the pUC 18 DNA was digested with Nde*I*. Therefore, 600 μl of DNA solution, 20 $\mu l NdeI$, 70 μl buffer and 10 μl MilliQ water were incubated for 4 h at 37 °C.

To determine the purity of the DNA after restriction, gelelectrophoresis was performed (see figure 3.1). Therefore, a 1.2% agarose gel (see 3.1.2) was used. In figure 3.1 the difference between the pUC18 DNA before and after digestion could be clearly noticed. Before the restriction, several bands could be seen whereas after the restriction only one bright band was visible. The several bands before restriction were based on different conformations of the circular vector.

After quality check, remaining impurities were removed from the DNA. Therefore, a QIAquick Purification kit from Qiagen, USA, was used, according to supplier's information. The DNA bound specifically to the column, whereas impurities were removed during the washing step. Afterwards, the DNA was eluted with 50 μl MilliQ water. The concentration was determined to 360 $ng/\mu l$, the total amount of linearized pUC18 DNA was 72 μg.

3.1.2 Gelelectrophoresis/ EMSA

The gelelectrophoresis was performed in 1.2% agarose gel. For production of the gel, the appropriate amount of agarose was solved in 1 fold TAE buffer, containing 400 mM Tris (99%, Roth, Germany), 100 mM NaCl (Riedel-de-Haen, Germany) and 10 mM EDTA (Sigma-Aldrich, Germany) in MilliQ water. The pH-value was set to 7.8 by glacial acetic acid (100%, Merck, Germany). The suspension was heated up until the agarose was fully dissolved. Afterwards, the suspension was filled in an acrylic glass chamber and a basset

[2]LB-medium consists of bacterial peptone, yeast extract, NaCl and agar

[3]g stands for acceleration of gravity with 9.81 m/s^2. That is a common notation of size in centrifugation.

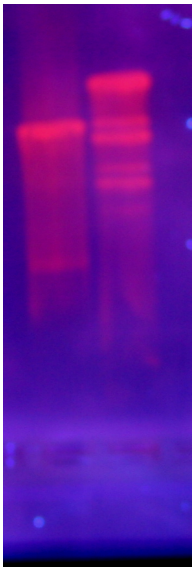

Figure 3.1: *Gel electrophoresis of pUC18 DNA before (right) and after digestion (left) with NdeI.*

was placed into it to form wells. After the gel was at room temperature, the basset was removed and the gel was carefully poured with TAE buffer.

100 ng of the DNA of interest was pipetted in each well with the same volume of loading buffer (TE/G buffer, Molekularbiologisches & Biochemisches Labor Dr. Bartling GmbH, Germany). For control of the experimental performance, size marker, pBR 328 Mix I from Molekularbiologisches & Biochemisches Labor Dr. Bartling GmbH, Germany, were pipetted in the outer wells in every experiment. The gelelectrophoresis was performed at 333 V/m for about 3 h. Afterwards, the DNA was labeled with ethidiumbromide (Merck, Germany), illuminated under UV-light (3UV-38 3 UV Lamp, UVP, Cambridge, UK) to visualize the DNA bands and photographed.

3.2 Production of masterwafer

During the experiments, several different channel layouts have been used for the different applications and chip enhancements (see section 4.1). The general chip production, nevertheless, was always the same according to the concept of soft lithography using a masterwafer with the negative relief structure [17, 174]. Briefly, on a silicone wafer the negative relief structures of the devices were built *via* photolithography. Afterwards, a liquid polymer was poured over the negative relief structure, cured, and peeled off.

In figure 3.2, the two-step contact lithographic production of the masterwafer is depicted. First, the silicon wafer (CrysTec, Germany) was purified twice in peroxy sulfuric acid,

one part sulfuric acid (concentrated, Merck, Germany) and three parts hydrogen peroxide (30%, Merck, Germany), for 5 minutes at a time and rinsed with deionized water. The wafer was dried in a centrifuge (Delta10, Ble-Laboratory Equipment GmbH, Germany) and baked on a hot plate (200 °C) for 20 minutes to remove the remaining water.

When the wafer was at room temperature, the first layer of SU-8 photoresist (Microresist, Germany), defining the height of the nanoslit, was spin coated. The layer thickness could be varied depending on the centrifugation time and speed and the solid fraction of photoresist (see also section 4.1). After prebake at 95 °C for 3 min the photoresist was illuminated through a chromium mask (Delta Mask, Netherlands) in a mask-aligner (MJB3, Süss MicroTec, Germany) for 1.7 s. Afterwards, the wafer was baked at 95 °C for 1 min and developed in mr-dev developer (Microresist, USA) for 1 min. With acetone and isopropanol, successively, the wafer was rinsed and dried with nitrogen. The layer thickness was determined with a profilometer (DekTak 3030 ST, Stanford Nanofabrication Facility Equipment, USA).

The outline of the ridge was structured with the second layer of photoresist also determining the height of free channel. Before the second layer of photoresist was poured onto the wafer, the position crosses were covered with adhesive tape. For the second layer, SU-8 photoresist with 52% solid fraction was used for all devices. The photoresist was poured onto the wafer and spincoated at 3000 rpm for 30 s. After a prebake at 95 °C for 3 min, the adhesive tapes were removed and the second photomask was carefully aligned with the mask aligner. The second layer was illuminated for 7 s according to supplier's information. Again, the photoresist was developed after a post exposure bake at 95 °C for 3 min. With acetone and isopropanol, successively, the wafer was rinsed and dried with nitrogen. A thickness of 5 μm was determined for the second layer. Whereas the total structure height depended on the height of the first layer.

After terminal bake, 200 °C for 20 min, the masterwafer was silanized to enable repeated molding. Therefore, the wafer was mounted in an exsiccator and 10 droplets of Tridecafluor-1,1,2,2-tetra-hydrooctyltrichlorsilan (TTTS) from Merck, Germany, were given on a watch-glass. Then the exsiccator was evacuated with a turbo pump for 30 min and rest for further 30 min.

3.3 Preparation of microfluidic chip

The masterwafer was poured with a double-layer of hard poly(dimethylsiloxane) (h-PDMS) [175] and poly(dimethylsiloxane) (PDMS) [17]. The h-PDMS, 3.4 g vinylmethylsiloxane-dimethylsiloxane trimethylsiloxy terminated copolymer (ABCR GmbH & Co KG, Germany), 18 μl platinum-divinyltetramethylsiloxane complex (ABCR GmbH & Co KG, Germany), 1 droplet of 2,4,6,8-tetramethyl-2,4,6,8-tetravinylcyclotetrasiloxane (Sigma Aldrich, Germany) and 1 ml (25-35% methylhydrosiloxane)-dimethylsiloxane copolymer (ABCR GmbH & Co KG, Germany), was stirred and poured onto the masterwafer and precured on a hot plate at 65 °C for 3 min. The height of the h-PDMS layer was about 40 μm.

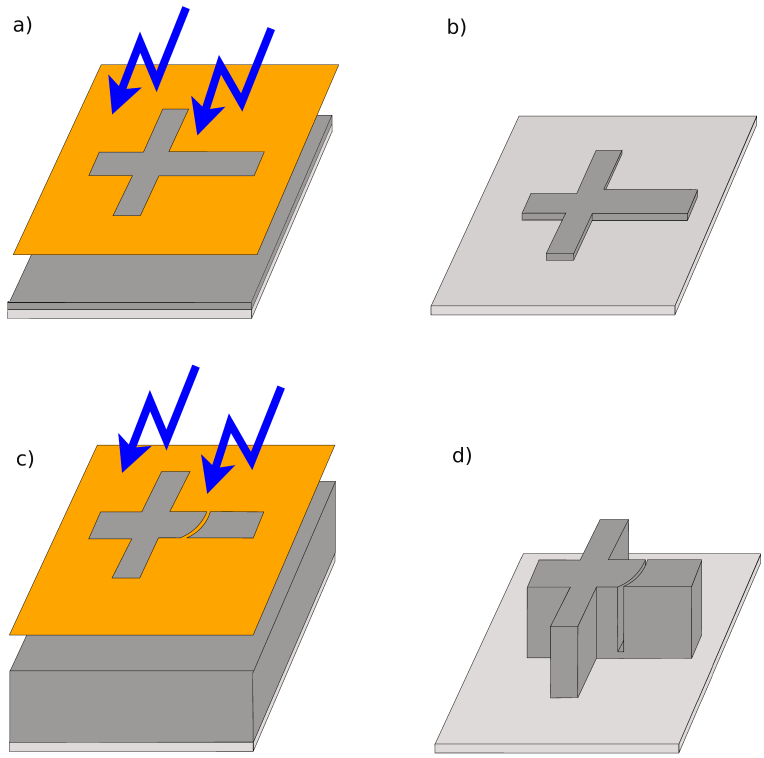

Figure 3.2: *Scheme of masterwafer production. a) Thin layer of photoresist (dark grey) was spincoated on a silicon wafer (light grey) and illuminated through a chromium mask (orange), defining the nanoslit height and the general channel layout. b) Silicon wafer with first layer of photoresist after developing. c) Second layer of photoresist was spincoated and illuminated through a chromium mask, defining the ridge shape and free channel height. d) Masterwafer, with negative relief structure, ready to be molded with PDMS.*

Thus, the h-PDMS covered the whole photoresist structures. On top of the h-PDMS layer a layer of PDMS, 7 g prepolymer (Sylgard, Dow Corning, Germany) and 0.7 g linker (Silicone elastomer curing agent, Dow Corning, Germany), was poured. The double layer was cured on a hot plate, 65 °C for 45 min [56].

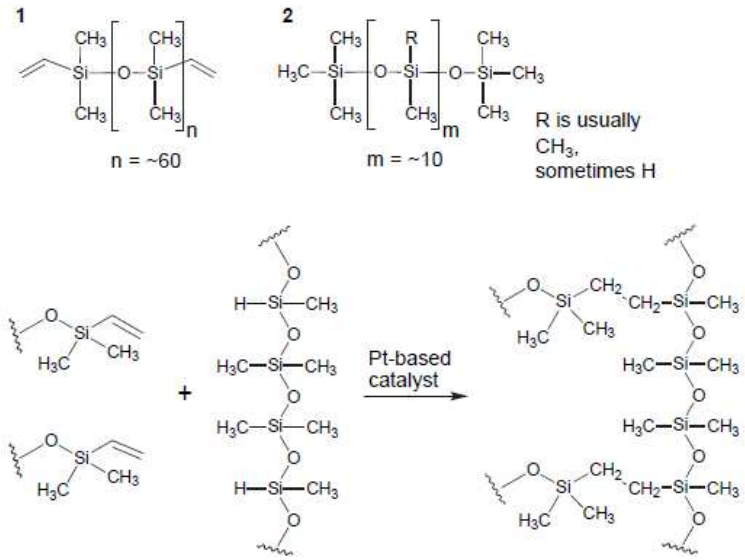

Figure 3.3: *Chemical structure of PDMS and the linker, accordingly. The cross-linking was catalyzed by a platinum-based catalyzer [176].*

After curing, the PDMS slab was peeled off and the channel structures of interest were cut out. For access to the channel, holes were punched at the channel ends. With PDMS spincoated (3000 rpm, 30 s, cured at 65 °C for 10 min) coverslips the structures were closed (see figure 3.4). The PDMS slab and the coverslips were cleaned successively in acetone, ethanol (Merck, Germany), and deionized water in an ultrasonic bath (T490A, Elma, Germany) and dried with nitrogen. The PDMS slab and the cover slips were oxidized (for 30 s) in a homemade plasma-chamber [125]. The chip was assembled subsequent to the plasmaoxidation.

30 min after chip assembly, the channels were filled with the running buffer. To minimize adhesion of particles to the PDMS surface and for control of electroosmotic flow, the running buffer contained n-dodecyle-β-D-maltoside for the DNA experiments, or the Pluronic F_{108} for the polystyrene bead experiments [17, 56, 177]. A Plexiglas holder with platinum electrodes was placed on the microchip for electronic contact and to enlarge the reservoirs. In each reservoir of the Plexiglas holder 9 μl solution were pipetted according to the experiment.

As mentioned in section 2.1.2, the DNA was fluorescent labeled with YOYO-1 (Invitrogen, USA). Therefore, DNA was incubated with YOYO-1 (ratio of 1 YOYO-1 per 10 DNA base

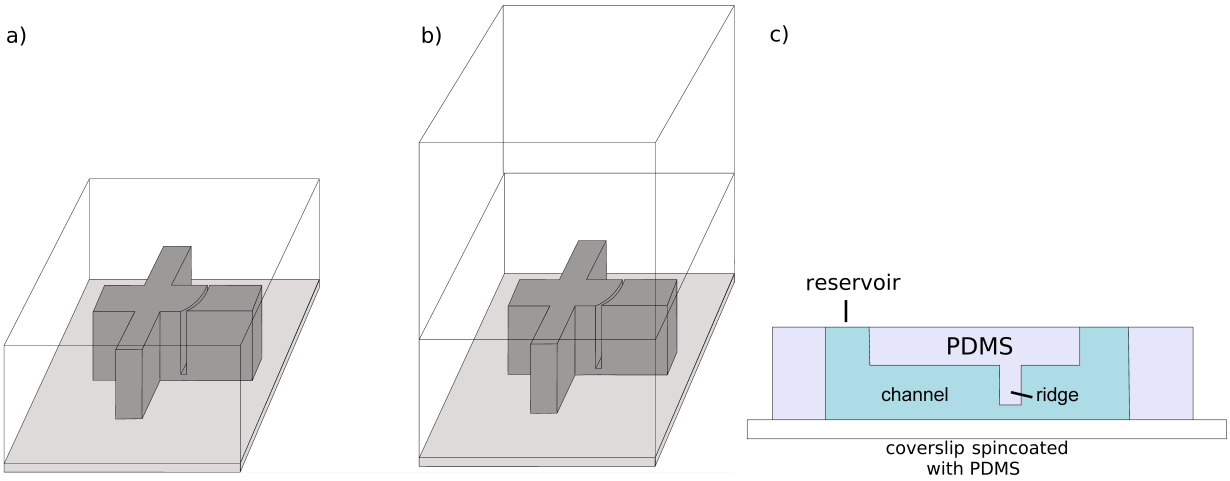

Figure 3.4: *Scheme of double-layer soft lithography. a) First layer of h-PDMS 40 µm in height (not to scale), to stably mold the constriction. b) Second layer of PDMS 1 mm (not to scale), for better handability. c) Cross section of assembled chip with reservoirs and running buffer (blue).*

pairs) for 2 h on a vortexer (Vortexer-Genie 2, Scientific Industries, USA, 0-level). For the drug-DNA complexes Actinomycin D (ACTD, 384 MDa, Applichem, Germany, 0.3 mM) was added to 100 ng DNA in three different amounts, 2 μl (ratio of 1 ACTD per 5 DNA base pairs), 1 μl (ratio of 1 ACTD per 10 DNA base pairs) or 0.5 μl (ratio of 1 ACTD per 5 DNA base pairs), respectively. The second DNA-complex was formed with *E. coli* RNA polymerase core enzyme (Epicentre Biotechnologies, USA, MW 389 kDa), 2 μl of stock solution were added to 100 ng DNA. The DNA-complex solutions also contained YOYO-1 and were incubated for 2 h, either.

Additionally, to DNA experiments, nanobeads were used for manipulation experiments and characterization of the nano channel (see section 4). Therefore, carboxylated polystyrene beads (FluoSpheres, Invitrogen, USA) were used. The beads were fluorescently labeled, 20 nm and 100 nm (Ex 580 nm/ Em 605 nm) and 40 nm, 60 nm and 500 nm(Ex 505 nm/Em 515 nm).

For all on-chip experiments, the solutions were diluted to about 10 pM concentration, for the DNA experiments as well as for the bead experiments.

3.4 Experimental setup

The prepared microchip with the Plexiglas holder was mounted on the motorized xy-stage of an inverted fluorescence microscope (Axiovert 200, Zeiss, Germany) (see figure 3.5). Illumination of the specimen was performed with a mercury vapor lamp (HBO50, Zeiss, Germany). All experiments, except for 500 μm beads, were performed with a 100-fold oil-

immersion objective (PLAN Neofluar, NA 1.3, Zeiss, Germany). Two different fluorescence filter sets consisted of 1) BP 450-490 a FT 510 and BP 515-565 (for DNA, 40 nm, 60 nm, and 500 nm bead experiments) and 2) BP 546/12 a FT 560 and BP 575/640 (for 20 nm and 100 nm bead experiments).

A gray filter with 25% transmittance reduced the emission light to minimize photobleaching. For image acquisition a SensiCam PCI interface board (PCO, Germany) was used as video grabber together with DaVis 6.2 software (LaVision, Germany).

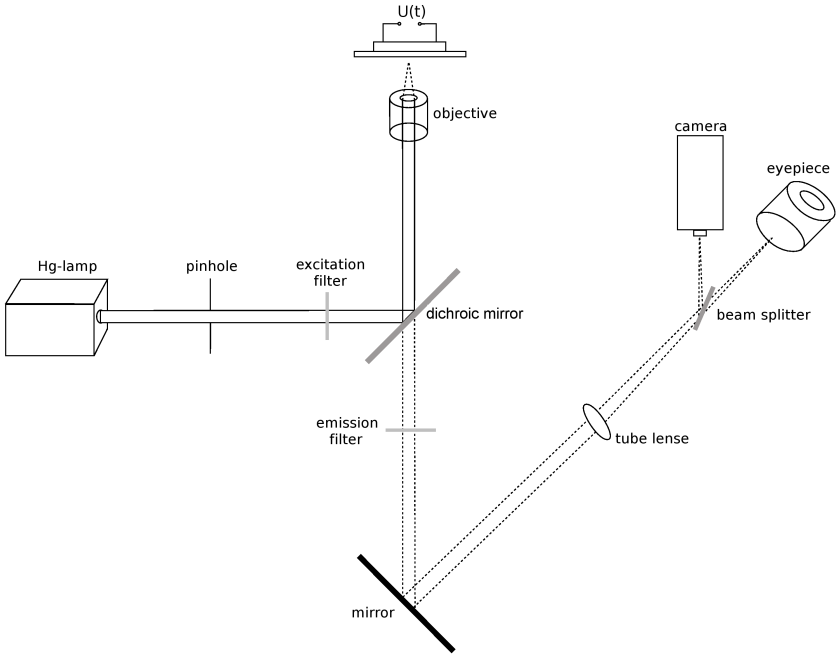

Figure 3.5: *Setup of inverted fluorescence microscope with mounted microfluidic chip connected to voltage source.*

The dc-voltages were generated with power supplies from FUG (HCL 14-12500, Germany), the ac-voltages were generated with a DS 345 function generator from Stanford Research Systems, USA, and 100-fold amplified with an AMS-1B30 amplifier (Matsusada Precision, Japan). The applied voltages and frequencies were controlled *via* custom-made LabView 6i programs.

For the hydrodynamically driven nanobeads (see section 4.2), the pressure was generated by applying nitrogen. A custom-made LabView 6i program controlled the 3/2 way valves (MHA2-MS1H-3/2G-2-K, Festo, Germany).

3.5 Experimental procedures

3.5.1 Polystyrene bead procedures

Passability of nanoslit The passability of the nanoslits was tested with appropriate polystyrene beads. Beads with diameter of 100 nm for heights of 125 nm and 180 nm, or beads with diameter of 500 nm, for nanoslits of height more than 500 nm were used, respectively. In case of the 100 nm beads, a 100-fold oil-immersion objective was used. For the 500 nm beads a 40-fold objective was used, that allowed overview of the whole channel width. The beads were driven by dc-voltages and image sequences of fluorescence video microscopy were recorded at the nanoslits for each ridge layout and width-to-height aspect ratio. The frame rate was 10 fps. The binning was 8 by 8 pixels.

Electrostatic sieving For the continuous-flow electrostatic sieving of nanobeads, first the mixture was injected towards the nanoslit by hydrodynamic flow. Therefore, pressures were applied at reservoirs 1 and 3 (see figure 3.6), such that the nanobeads flow in a narrow stream that occupied less than a quarter of the channel width. Additionally, dc-voltages were superimposed at reservoir 2 and adapted until a total deflection of one species was observed. The channel was scanned over the whole channel width up- and downstream of the ridge (see Image processing).

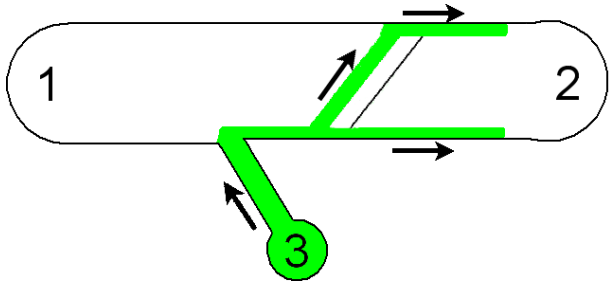

Figure 3.6: *Sketch of continuous-flow electrostatic sieving. A mixture of nanobeads was injected from channel 3 into channel 2 via pressure driven flow. For appropriate parameters (dc-voltage, pressure) one sort of beads was totally deflected, whereas the second sort passed the nanoslit unaffected (see section 4.2).*

Dielectrophoretic mixing For the continuous-flow mixing of nanobeads, two sorts of beads were injected from opposed channels 3 and 4 into channel 2 (see figure 3.7). The beads were driven by electroosmotic flow. Therefore, appropriate dc-voltages -less than 40 V- were applied at channels 1, 3, and 4 such that both particle streams immediately bend and flow parallel to the channel wall occupying less than a quarter channel width each.

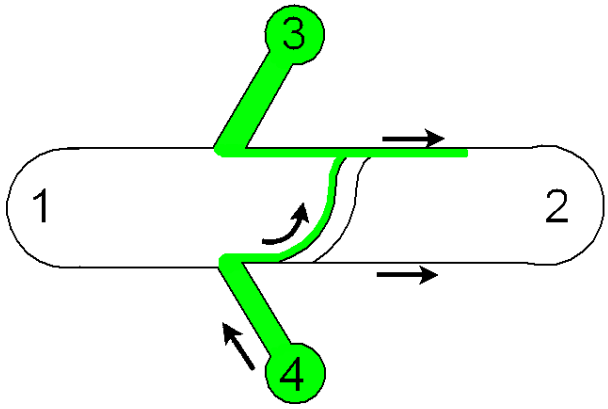

Figure 3.7: *Sketch of continuous-flow mixing procedure of polystyrene nanobeads. The nanobeads were injected from channels 3 and 4 via electroosmotic flow. For appropriate parameters (dc- and ac-voltages, frequency) beads from reservoir 4 were totally deflected at the ridge and led into the second stream.*

To start the mixing process ac-voltages were superimposed at channel 1 to deflect the beads of channel 4 into the second stream. Appropriate ac-voltage and frequency were determined as follows. First, ac-voltage was set to a reasonable small value, 50 V. Then the frequency was tuned in the range of 50 Hz to 1000 Hz. If no full deflection of beads was observed, the ac-voltage was set to a higher value and again the frequency was tuned from 50 Hz to 1000 Hz. This scheme was repeated until a full deflection of beads along the ridge was observed.

During the mixing the channel was scanned over the whole channel width (see Image processing). Since the two bead species differed in brightness, the joined stream could be evaluated by eye due to the particles distribution.

Dielectrophoretic separation For the nanobead separation, a mixture of various species was continuously injected from channel 4 into channel 2 towards the ridge (see figure 3.8). The beads were driven *via* electroosmotic flow by appropriate dc-voltages applied to channels 1,3 and 4. The dc-voltages were set such that the particle stream was bended immediately in a narrow stream -occupying less than quarter of the channel width- that flew parallel to the channel wall. An ac-voltage was superimposed at channel 1 to generate a dielectrophoretic landscape.

Appropriate ac-voltage and frequency were determined as follows. First, ac-voltage was set to reasonable small value of 50 V, then the frequency was tuned in the range of 50 Hz to 1000 Hz. If no full deflection of beads was observed at the ridge, the ac-voltage was set to a higher value and again the frequency was tuned from 50 Hz to 1000 Hz. This scheme was repeated until a full deflection of beads along the ridge was observed. Afterwards, a separation of the mixture was performed. During the separation, the channel was scanned

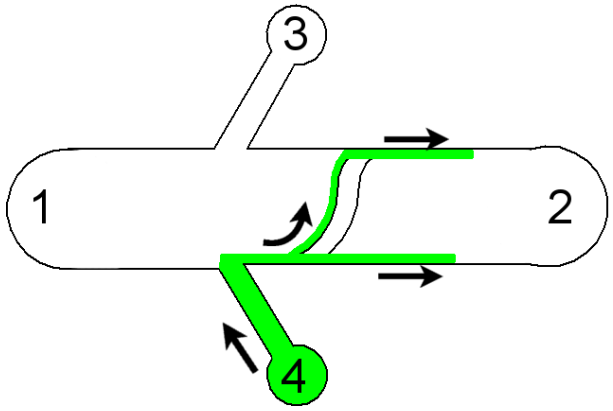

Figure 3.8: *Sketch of continuous-flow separation procedure of polystyrene nanobeads. A mixture of nanobeads was injected from channel 4 into channel 2 via electroosmotic flow. For appropriate parameters (dc- and ac-voltages, frequency) one sort of beads was totally deflected, whereas the second sort passed the nanoslit unaffected. The manipulated/deflected nanobeads exhibited negative dielectrophoresis (see section 2.3.4).*

(see Image processing).

Image processing For the 100-fold objective the region of interest (ROI) captured 86 μm in x-direction and 68.6 μm in y-direction, i.e. the channel had to be scanned during the experiments to catch the whole channel width. The channel was scanned in y-direction with constant speed, 10 $\mu m/s$ at different x-positions of interest. The y-position within the channel was determined by scanning time and speed. Raw image data were processed in DaVis 6.2 with a nonlinear filter.

The region of interest (ROI) was partitioned in six slices (see figure 3.9) each with height 11.4 μm (y-direction) to reduce convolution effects. Successively recorded images were shifted by 1 μm in y-direction (due to scanning speed and frame rate), so that every eleventh image the slices overlapped. The fluorescence intensity distribution in the channel, corresponded to the nanobead distribution. For all slices, the total fluorescence intensity was determined. The measured intensity was averaged up to six such overlapping slices and plotted versus the y-position. These data were fitted with Gaussian curves and the separation resolution was calculated by equation (2.4).

Mean free mobility The mean free mobility of the polystyrene beads was determined for successful separation and mixing experiments at fixed voltages. Therefore, the molecules flow was recorded (10 fps, 8 by 8 pixels binning) downstream of the constriction for separation and upstream of the constriction for mixing. Using tracking software (ImageJ plugin "ParticleTracker" by G. Levy) the trajectories, parallel to channel axis, were evaluated and the velocity was calculated by the trajectory length and recorded time. The mean free mobility was calculated for an average of 30 particles per experiment.

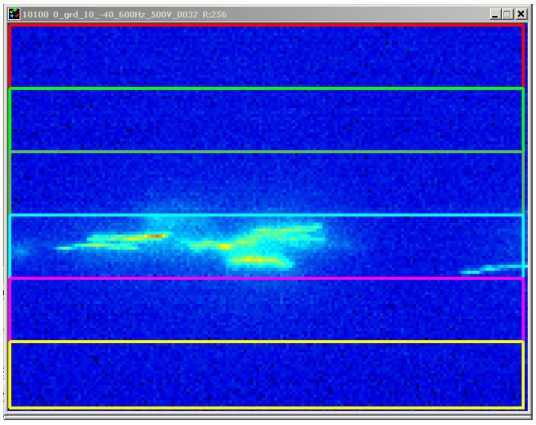

Figure 3.9: *The region of interest was partitioned in six slices, each with height of 11 µm. To determine the analytes distribution the fluorescence intensity was measured in each slice, separately, along the scanning procedure, and averaged over up to six overlapping slices.*

3.5.2 DNA procedures

Separation For the continuous-flow DNA separation and complex detection the mixture of DNA molecules was continuously injected from channel 4 into channel 2 towards the ridge (see figure 3.10). The DNA was driven electrophoretically by appropriate dc-voltages (see section 4.3) applied to channels 1,3 and 4. The dc-voltages were set such that the DNA was immediately bent in a narrow stream -occupied less than quarter of the channel width- that flew parallel to the channel wall. An ac-voltage was superimposed to generate a dielectrophoretic potential landscape.

Appropriate ac-voltages and frequencies were determined as follows. First, ac-voltage was set to reasonable small value, 50 V, then the frequency was tuned in the range of 50 Hz to 1000 Hz. If no full deflection of DNA was observed, the ac-voltage was set to a higher value and again the frequency was tuned from 50 Hz to 1000 Hz. This scheme was repeated until a full deflection of DNA along the ridge was observed. Afterwards, a separation of the mixture was performed. During the separation the channel was scanned over the channel width (see Image processing).

Mixing For the DNA continuous-flow mixing experiments two sorts of DNA were injected from opposed channels 3 and 4 into channel 2 (see figure 3.11). The DNA was driven electrophoretically by appropriate dc-voltages applied to channels 1,3 and 4 such that both DNA streams immediately bend and flow parallel to the channel wall each occupying less than a quarter channel width.

To start the mixing process, ac-voltages were superimposed at channel 1 to deflect the DNA of channel 4 into the molecules stream of channel 3. Appropriate ac-voltage and frequency were determined as follows. First, ac-voltage was set to reasonable small value

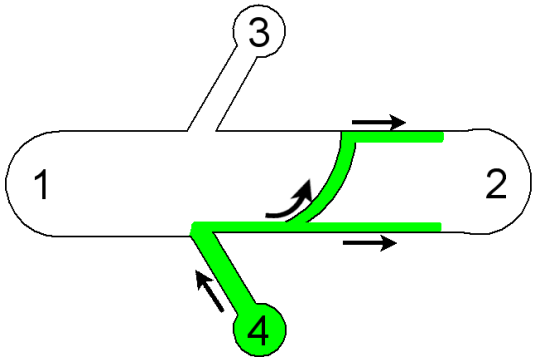

Figure 3.10: *Sketch of separation procedure. A mixture of two sorts of DNA was injected from channel 4 into channel 2 via electrophoresis. For appropriate parameters (dc- and ac-voltages, frequency) one sort of DNA was deflected at the ridge whereas the second sort passed the nanoslit unaffected.*

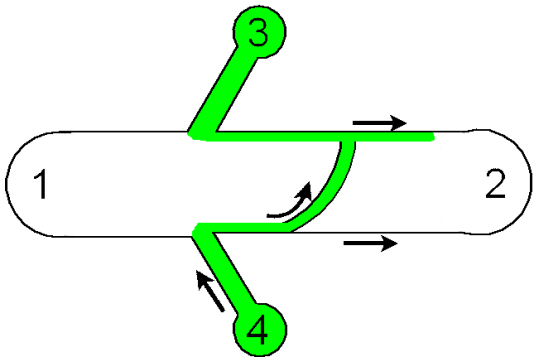

Figure 3.11: *Sketch of mixing procedure. The DNA was injected from channels 3 and 4 via electrophoresis. For appropriate parameters (dc- and ac-voltages, frequency) DNA from reservoir 4 was totally deflected at the ridge and led into the second molecules stream.*

of 50 V, then the frequency was tuned in the range of 50 Hz to 1000 Hz. If no full deflection of DNA was observed, the ac-voltage was set to a higher value and again the frequency was tuned from 50 Hz to 1000 Hz. This scheme was repeated until a full deflection of DNA along the ridge was observed. During the mixing the channel was scanned over the whole channel width (see Image processing).

Image processing For the 100-fold objective the region of interest (ROI) captured 86 μm in x-direction and 68.6 μm in y-direction, i.e. the channel had to be scanned during the experiments to catch the whole channel width, important for the continuous-flow performances. The channel was scanned in y-direction with constant speed, 10 $\mu m/s$ at different x-positions of interest. The y-position within the channel was determined by scanning time and speed. Raw image data were processed in DaVis 6.2 with a nonlinear filter.

The region of interest (ROI) was partitioned in six slices (see figure 3.9) each with height of 11.4 μm (y-direction) to reduce convolution effects. Successively recorded images were shifted by 1 μm in y-direction (due to scanning speed and frame rate), so that every eleventh image the slices overlapped. For all slices, the total fluorescence intensity was determined. The measured intensity at a fixed position in the array of nanoslits was averaged up to six such overlapping slices and plotted versus the y-position. These data were fitted with Gaussian curves and the separation resolution was calculated by equation (2.4).

Dielectrophoretic mobility shift assays (DEMSA) For performing DEMSA experiments, the analytes of interest were driven subsequently through an array of nanoslits. Therefore, pinched injection protocol was used to inject a defined amount of analyte towards the nanoslits [178]. In first step, at reservoirs 1,2 and 3 dc-voltages were set such that the DNA molecules migrated from reservoir 3 to reservoir 4 without leaking into channels 1 and 2 (see figure 3.12). In the second step, dc-voltage was superimposed by an ac-voltage, both applied at reservoir 1, to drive a defined amount of DNA molecules to reservoir 4 and simultaneously create dielectrophoretic traps at the nanoslits. Channels 2,3 and 4 were grounded. The fluorescence intensities were monitored during the second step and plotted versus time for each species, afterwards.

Polarizability For quantification of the polarizabilities, pinched injection protocol was used similar to the DEMSA experiments (see above) to drive the DNA-molecules through the array of nanoslits. Additionally, after each injection the applied ac-voltages were varied to generate dielectrophoretic traps of varying depth.

In a well-defined region of interest (ROI), an image sequence of molecules passing by was recorded for each U_{ac}, also for $U_{ac} = 0$. Since the fluorescence intensity was directly proportional to the amount of DNA the mean trapping time of DNA could be determined automatically [126]. To calculate the polarizability, equation (2.24) is rewritten as [126, 179]

$$ln\tau = const + \frac{\xi \alpha U_{ac}^2}{k_B T} \quad . \tag{3.1}$$

With ξ as a constant value of the device that depended on the exact geometrical channel dimensions. For calculation of the polarizability $ln\tau$ was plotted versus U_{ac}^2 and fitted with

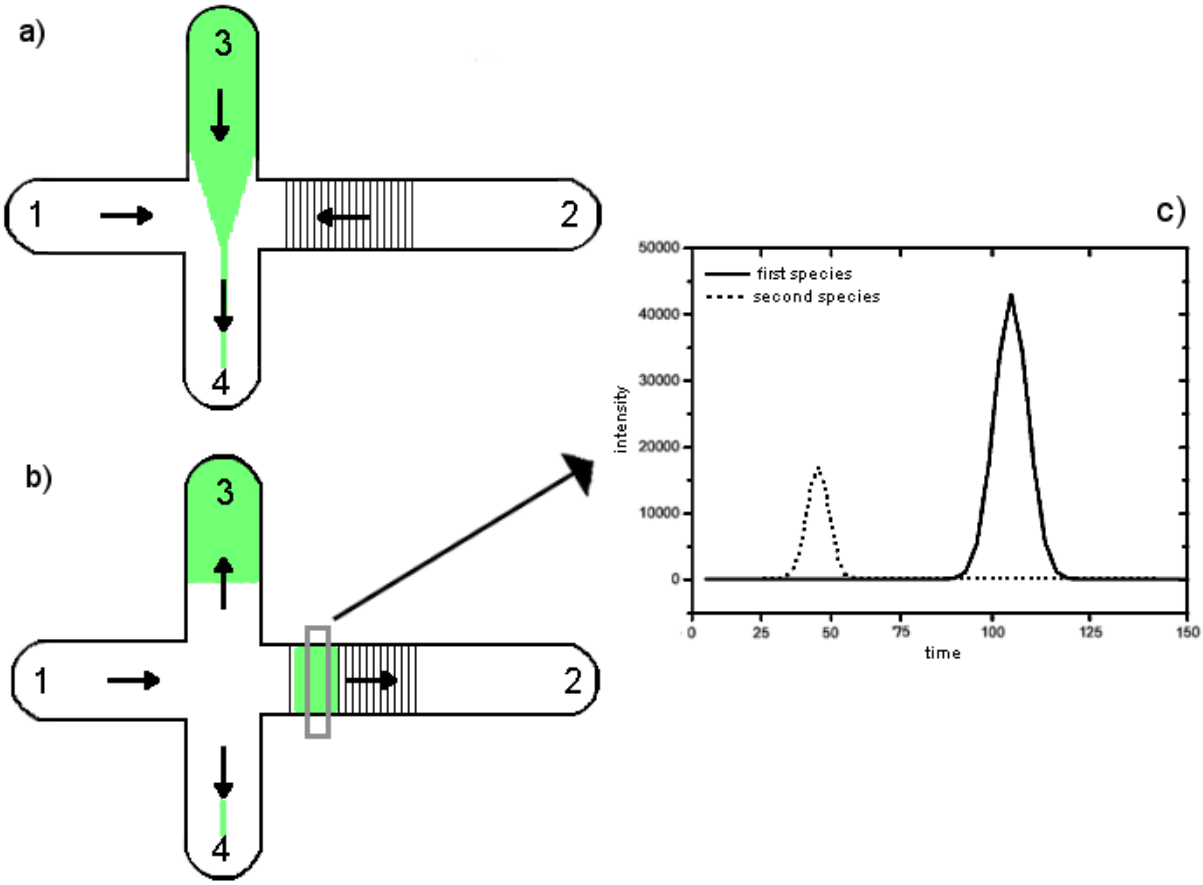

Figure 3.12: *Sketch of pinched injection protocol and fluorescence evaluation, as used for DEMSA experiments. First, the analyte stream was focused in a narrow stream a). In the second step a defined amount of analyte was injected in the structured channel b) and fluorescence intensity was monitored downstream of the ridges. By plotting the fluorescence intensities versus time for each species, complex formation was detected c).*

equation (3.1). With the slope of the linear fit, ξ, and k_BT, the polarizability could be determined [126].

Diffusion To determine the diffusion constant of DNA the Brownian motion was recorded over about 60 s in the microfluidic chip. The images were taken with a 100-fold oil-immersion objective with 10 frames per second (fps) and a binning of 8 by 8 pixels. *Via* pinched injection a defined volume ($\approx$ 60 fl) of DNA was injected into the channel [178]. After the injection, all voltages were switched off.

The DNA was highly diluted ($\approx$ 10 pM), thus single molecule trajectories could be observed. Using tracking software (ImageJ plugin "ParticleTracker" by G. Levy) the trajectories were evaluated. When plotting the mean square distance versus the time the diffusion constant could be calculated from the slope of the fit using equation (2.19)(see section 2.5).

3.6 AFM imaging of DNA/RNAP-complexes

The DNA/RNAP-complexes were displayed *via* scanning force microscopy, AFM (Bioscope, Veeco, USA). The DNA was prepared as for the chip experiments, lacking the dilution to 10 pM concentration. The stock solution of RNAP/DNA-complexes was diluted 20-fold with 1 mM phosphate buffer, consisting 1 mM EDTA and 2 mM Trolox. 1.5 μl of the solution was pipetted on a silanized Mica slice. After the buffer was completely evaporated, the Mica slice was rinsed with MilliQ water and dried with nitrogen.

The prepared samples were mounted on the Bioscope stage and images were taken in tapping-mode (frequency 300 kHz, scan rate 0.5 Hz) with TAP 300-AL cantilever from Budget Sensors, Bulgaria.

4 Results and discussion

In the next sections, the results are presented and discussed. The goal of this thesis was to develop new analytical and preparative tools for application in μTAS that combined several contrary features. All novel tools that were developed had in common that they were placed in the vicinity of a nanochannel. Thus, at the beginning the reproducible production of nanochannels was necessary. In section 4.1 the production and characterization of the nano-microfluidic devices is presented. After the successful production of nano-microchannel the results of continuous-flow separation of nanobeads and manipulation of proteins via electrostatic sieving is demonstrated in section 4.2. In section 4.3 the basic concept of dielectrophoretic continuous-flow mixing and separation of nanoobjects is described. The experimental results of dielectrophoretic manipulation of nanobeads are presented and discussed in section 4.4. That is followed by the description of dielectrophoretic manipulation and characterization of DNA in section 4.5. Finally, two new techniques for detection of DNA-complexes are presented with continuous-flow detection and dielectrophoretic mobility shift assays. Both new detection methods are compared with the established technique of electrophoretic mobility shift assays (EMSA).

4.1 Production of device

When designing a microfluidic device some preliminary conditions have to be considered. First, the function of the device, i.e. is it used for detection, separation or mixing? Second, the kind of operation mode, batch processing or continuous-flow, is important for the design layout. Additionally, the investigated probe, biological or artificial, must be considered. Especially for biological probes, the experimental environment is important. Some analytes need special surroundings, like pH-value, surfactants, and gases and so on. Last but not least the material of the device had to be capable to the former mentioned requirements [17].

The goal of this thesis was to develop versatile nano-microfluidic devices that allowed preparative tools like mixing, separation or purification as well as analytical tools for detection. The novel method should yield access to nanobeads, small DNA-fragments or proteins and detection of complex-formation. The nano-microfluidic devices were as various as the aimed applications (see figure 4.1). Nevertheless all methods that are demonstrated relied on one or several ridges that narrowed a microchannel, and thus formed nanochannels.

Up to now, the production of nanochannels was challenging. Most of the nanochannels are made by chemical or physical etching [18]. Physical etching is very time consuming and for chemical etching, often hazardous acids or bases are necessary, furthermore both techniques are very expensive [174, 180].

In contrast to the etching techniques, in this thesis, soft lithography with poly(dimethylsiloxane) (PDMS) was used to fabricate the microfluidic devices. Soft lithography allowed

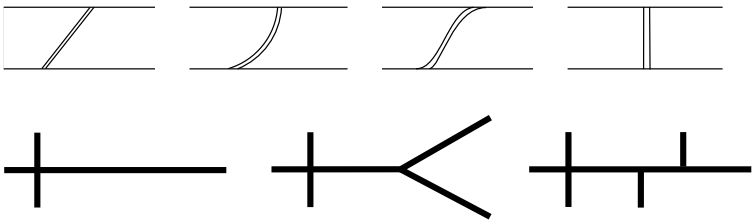

Figure 4.1: *Overview of variety of device layouts (all in top view). Top: layouts of ridges, from left to right: diagonal, arc, s-shaped, perpendicular. Bottom: layouts of microchannel.*

solid fraction [%]	rpm	time [s]	thickness [nm]
52	3000	30	5000 ±50
17	900	30	670 ±30
17	1000	30	520 ±20
13	1000	30	180 ±15
13	1500	30	115 ±15

Table 1: Thickness of photoresist due to solid fraction of SU-8 and centrifugation parameters (rounds per minute (rpm) and time). The height slightly varies between two masterwafer according to the time of precentrifugation.

fast chip developments in one day and subsequent chips within few hours [17]. PDMS was used throughout this work because of its material properties; PDMS is biocompatible, gas permeable and electric insulating as well as mechanical and chemical stable [2, 181]. Due to its transparency in the visible spectrum, 300-700 nm [182], it allowed detection of fluorescent stained molecules. With US$ 0.47 costs per device, reflecting the raw material costs and effort it took to produce the device, PDMS chips were very cheap [183]. Although PDMS exhibited several advantages, up to now monolithic production of stable nanochannels of PDMS was impossible.

When producing the device, first the negative relief structures were built on a silicone wafer, forming the masterwafer. As described in section 3.2, the masterwafer was built *via* two-step contact lithography. In the first lithography step, the height of the nanoslit was defined. The solid fraction of SU-8 photoresist was 17% or 13%, respectively. According to the spin coating parameters and the solid fraction, the structure height could be adjusted (see table 1) and was controlled by profilometer scans (figure 4.2 a-c). In the second photolithography step, the layout of the ridges and the total channel height were defined. The second layer had a thickness of 5 μm, whereas the total structure height varied between 5.2 μm and 5.7 μm, due to the height of the first layer.

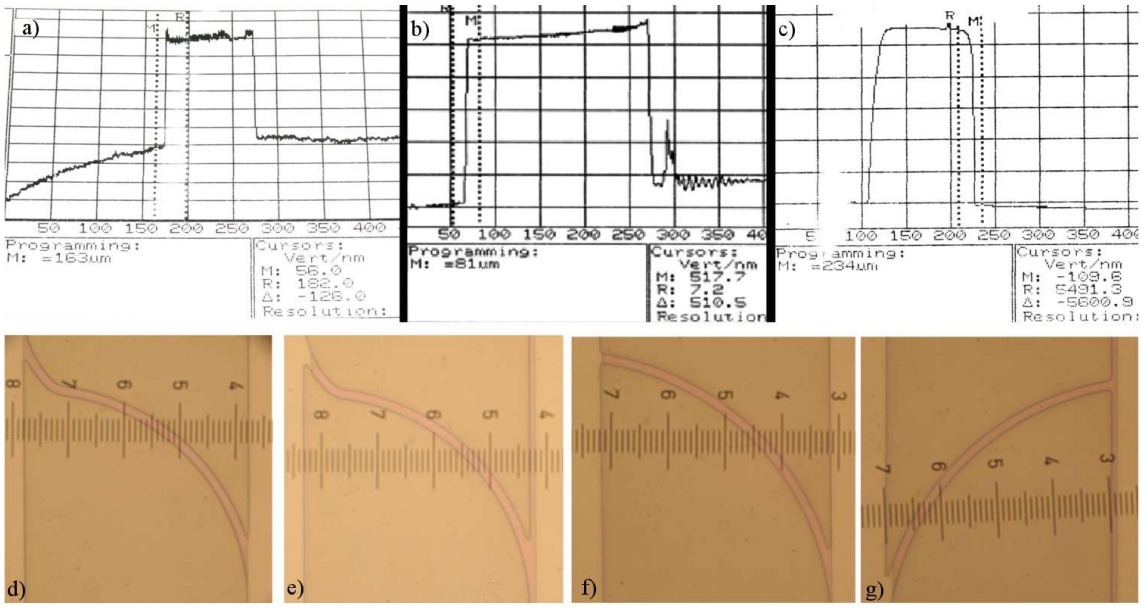

Figure 4.2: *Control of production process via profilometer scans (a-c) and photographs of masterwafer with 20 fold magnification, all channels with width of 200 µm (d-g). a) 126 nm structure height for first SU-8 layer. b) 510 nm structure height for first SU-8 layer. c) 5.6 µm height of whole structure after terminal back. d) and f) perfectly aligned structures with asymmetric-s and arc-shaped ridges. e) and g) Structures with lateral displacement. The second layers were slightly shifted to the left.*

The second lithographic step was the most critical and time-consuming along the production process, since the photomask had to be aligned perfectly to the first layer without lateral displacement or tilting. Most of the second layers fit perfectly to the first (see figure 4.2 d) and f). Only in few cases a displacement of the two layers became visible (see figure 4.2 e) and g).

A double layer of hard PDMS (h-PDMS) [175] and PDMS enabled a stable nanochannel. The h-PDMS exhibited a higher mechanical stability, but was too brittle for single use, no peel off of the masterwafer was possible. PDMS exhibited a higher elasticity that allowed an easy peel off of the master wafer, but prohibited a stable nanochannel. With the double layer, the advantages of both sorts were combined [17].

The stability or sagging, respectively, of the nanochannel was investigated by passability tests with appropriate nanobeads. In figure 4.3, time-lapsed fluorescence images are depicted. For nanochannels of height more than 500 nm, 500 nm polystyrene beads were used to investigate the sagging. The 500 nm beads passed the nanoslit over the full channel width. Hence, the flow through height was assumed to be more than 500 nm, since the beads could not pass the nanoslit otherwise. For the 125 nm and 180 nm nanochannels 100 nm beads were used. The beads only passed the 180 nm slit over the whole channel

width.

Concerning the reproducibility of the nanoslits, it was found that about 95% of the devices were stable. When passing the nanoslit the beads were depicted as longish structures. This was due to the fast migration according to the high electric fields within the nanoslit and the frame rate of image acquisition.

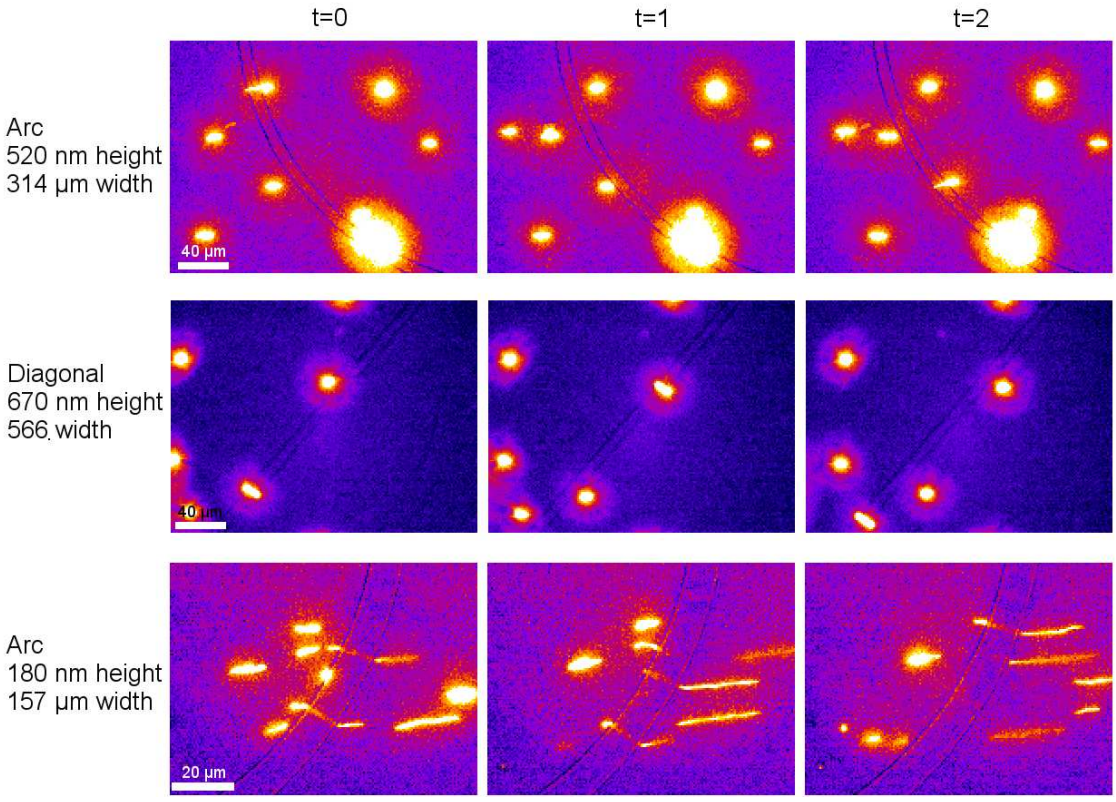

Figure 4.3: *Passability control of nanoslit. Time-lapsed fluorescence images of nanoslit are depicted. 500 nm beads were used, except for nanoslits of heights of 180 nm where 100 nm beads were used. The longish structures of the beads when passing the nanoslits were due to the increased electric fields within the nanoslit and the frame rate of image acquisition. The direction of flow was from left to right.*

Here, the 180 nm PDMS nanochannels were the channels of minimal height. The 125 nm slits collapsed and were not passable (not shown). Based on these results, stable nanochannels with width-to-height aspect ratios up to 873:1 were demonstrated. Thus, the highest aspect ratio was 14.5 times higher than the previously published results of Mao with an ratio of 60:1, for the use of PDMS [184], and 3.5 times higher than the results for the use of glass-silicone structures with a ratio of 250:1 [185].

4.2 Electrostatic sieving of nanoobjects

In this thesis, two different approaches for continuous-flow manipulation are presented. The general concept of continuous-flow processing was that a (selective) force was applied perpendicular to the direction of flow [186]. Hence, if two species, with different response to the force, reached the active region, each would exhibit a specific trajectory. Throughout this work, two independent forces were applied to the analytes. 1) A force that drove the analytes through the channel system. 2) A selective force in the vicinity of a nanoslit that allowed control of the analytes.

The first separation mechanism was based on an ion- or charge(density) selective electrostatic sieve (selective force) that was formed by an overlapping Debye layer within a nanoslit of 520 nm height [187]. This effect is also called concentration polarization [188]. Additionally, hydrodynamic pressures were applied to drive all analytes. The ridge was arranged with a 45° angle to the direction of flow. As a consequence, nanoobjects that were retarded by the electrostatic sieve migrated along the ridge. At the other channel wall, the beads passed the nanoslit, activated by thermal energy (*cf.* section 2.6). The hydrodynamic transport v_{hydr} depended only on the channel geometries and the applied pressures, i.e. $v_{hydr} \propto \Delta p$. Thus, by combining both transport effects, different properties were addressable selectively.

Since the separation mechanism was based on an overlapping electrical double layer, the dimensions of the electrical double layer were considered with respect to the nanochannel. An electric double layer was formed in the whole device due to the negatively charged PDMS surface (see section 2.3.2). To estimate the thickness of the electrical double layer a rule of thumb was used, that considered the ionic strength I [189]:

$$\lambda_D = \frac{2.1 \cdot 10^{-10} m}{\sqrt{I}} \quad . \tag{4.1}$$

With equation (4.1) a double layer of about 100 nm was calculated for MilliQ water (conductivity 4.59 μS/cm). Although smaller than the nanochannel height, it might be recalled that λ_D referred to the length at which the Debye potential dropped to 37%. Thus, a small overlap of both electric double layers seemed reasonable in the 520 nm height nanoslit. As a consequence, the nanoslit exhibited a non-neutral charge distribution (see figure 4.4), hence concentration polarization, and became ion-selective, i.e. differently charged objects exhibited different electrostatic interaction energies [57]. Gillespie calculated the ratio $\beta_{part} = \frac{c_n}{c_o}$ of nanoparticles within c_n and out c_o of the nanoslit by density functional theory for various particle radii and valencies [189]. An exponential dependency on radius and valency was found, that was used for separation throughout this thesis.

As a proof of principle, continuous-flow separation of highly carboxylated nanobeads, 20 nm (fluorescence emission 605 nm) and 40 nm (fluorescence emission 515 nm), was performed. The nanobeads differed significantly in surface charge density with $9.6 \cdot 10^{-6}$ C/cm^2 for the 20 nm beads and $4.2 \cdot 10^{-5}$ C/cm^2 for the 40 nm beads. The mixture of the beads was injected as a narrow stream towards the nanoslit *via* pressure-driven flow. When

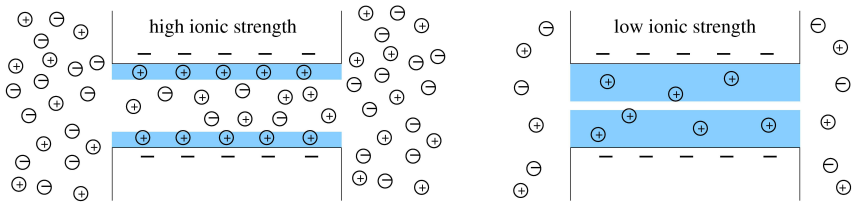

Figure 4.4: *Electrical double layer in a nanoslit for different ionic strengths. In case of high ionic strength, the Debye layers were small compared to the nanoslit height. In case vice versa, low ionic strength, the Debye layers increased and might overlap. Thus, the nanoslit became ion and (charged) particle selective, an electrostatic sieve, for either low ionic strength and/or narrow nanochannels.*

appropriate dc-voltages (7 V) were superimposed, the 36 nm beads were deflected along the ridge and passed the nanoslit at the other channel wall by Brownian motion, whereas the 15 nm beads passed the ridge unhindered. Thus, two distinct streams were observed downstream of the nanoslit (see figure 4.5).

Evaluation of the fluorescence distribution downstream of the ridge revealed that about 97% of the 40 nm beads were deflected, whereas most of the 20 nm beads (79%) passed the nanoslit unaffected. AFM images depicted that the size distribution of the 20 nm beads was very wide ranging from 7 to 35 nm with mean size of 15 nm. Hence, the reduced amount of unaffected 20 nm beads supported a size-dependent separation mechanism. Further analysis of the 20 nm beads size distribution revealed that particles larger than 23 nm were deflected. The size distribution of the 40 nm beads was more narrow with mean size of 36 nm $\pm$ 5 nm. This corresponded to the high amount of affected/deflected 40 nm beads (see figure 4.5).

To analyze the separation mechanism in more detail, additional experiments were performed for varying ionic strengths (conductivity respectively) or dc-voltages. Therefore response of 20 nm beads was investigated in MilliQ water with conductivity of 4.59 μS/cm, Debye length of 100 nm, and 1 mM phosphate buffer, Debye length of 2 nm. Due to the Debye lengths, the electrical double layers within the nanoslit overlapped only in MilliQ water. For both experiments, dc-voltages of 40 V were used. In figure 4.6 fluorescence images of the nanoslits during the experimental performance are depicted. The 20 nm beads were fully deflected at 40 V for the use of MilliQ water. In contrast, for the use of 1 mM phosphate buffer the beads were not deflected. The 40 nm beads were not deflected in 1 mM phosphate buffer, either (not shown). Thus, the electrical double layer overlap was mandatory for the sieving mechanism.

After determining the effect of the ionic strength, the applied voltages were varied. Since the electrical double layer overlap was mandatory dc-variations were performed in MilliQ water to investigate the effect of the applied voltage to the sieving mechanism. 20 nm

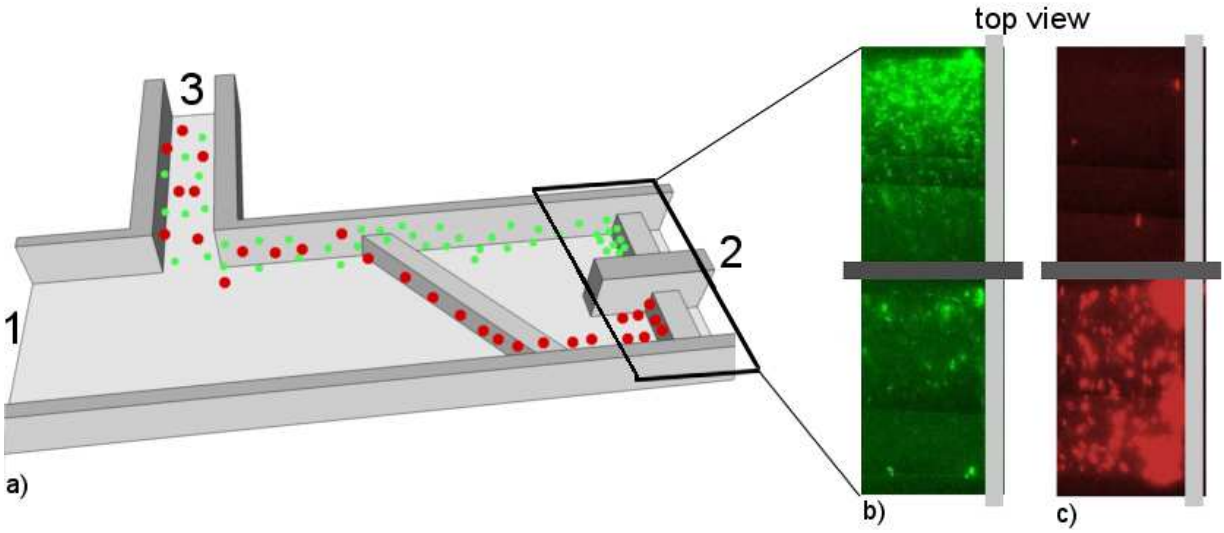

Figure 4.5: *Electrostatic sieving of nanobeads. a) Sketch of device consisting a 45° tilted ridge that created a 520 nm slit where the separation took part. A wall divided the channel into two with an additional orthogonal 520 nm slit. The 40 nm beads (red) were deflected at the tilted ridge, whereas the 15 nm beads (green) passed the ridge unhindered. Both species accumulated at the orthogonal ridge. b) Fluorescence images of the orthogonal ridge using the 605 nm emission filter, depicting the 20 nm beads. 79% of the 20 nm beads passed the nanoslit unaffected, i.e. appeared in the upper channel. The reduced percentage of unaffected beads was due to the wide size distribution of the 20 nm beads (particles up to 35 nm were observed in AFM images). c) Fluorescence images of the orthogonal ridge using the 515 nm emission filter, depicting the 40 nm beads. About 97% of the 40 nm beads were deflected. Hence, successful continuous-flow separation was achieved with electrostatic sieving.*

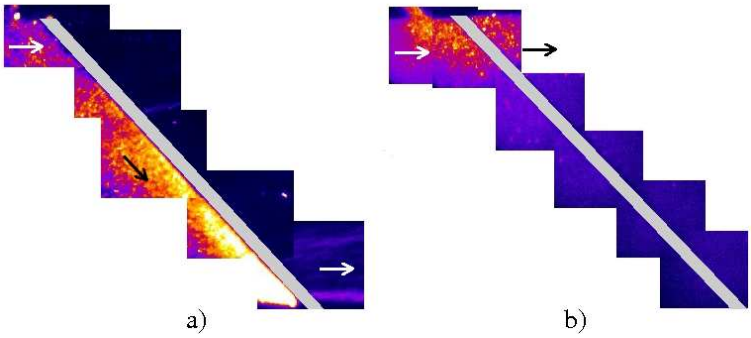

Figure 4.6: *The influence of electrical double layer overlap to the sieving mechanism was studied by varying the ionic strength (nanoslit of 520 nm height). The applied dc-voltage and the hydrodynamic pressures were kept constant: 40 V at reservoir 2, and 428 Pa and 611 Pa at reservoirs 1 and 3. a) MilliQ water with Debye length of 100 nm, 15 nm beads were deflected. b) For 1 mM phosphate buffer (2 nm Debye length) the 15 nm beads were not deflected.*

beads were deflected at the nanoslit for dc-voltages of more than 20 V. Otherwise the beads passed the ridge unaffected (see figure 4.7). This was in agreement with the separation demonstrated above, because the dc-voltages used for the sufficient separation were 7 V. These findings implied that the dc-voltage influenced the charge distribution at the nanoslit.

To understand these effects a close look is necessary concerning the ion distribution in the vicinity of the nanoslit. When dc-voltages were applied to the channel, the ions started to migrate. The counter-ions, positively charged, in the vicinity of the nanochannel migrated towards the cathode and passed the nanochannel. This led to counter-ion depletion at the anode side of the nanochannel [187]. In contrast, the negative ions migrated towards the anode, but could not pass the nanochannel. Thus, at the anode side of the nanochannel both sorts of ions depleted, whereas at the cathode side an ion-enrichment occurred. The size of the ion-enrichment or -depletion zone, respectively, depended on the strength of the applied voltages due to the equilibrium of the electrostatic and entropic forces. Hence, by applying dc-voltages, the intrinsic concentration polarization was enhanced and perm selectivity of the nanochannel was -controllably- increased. This effect has been mentioned in literature [7, 187, 190–192] but has not been demonstrated for continuous-flow operating processes, so far.

The electric double layer overlap within the nanochannel formed an electrostatic sieve for anions or negatively charged nanobeads, like the carboxylated polystyrene beads used for the experiments. The selectivity of the electrostatic sieving was controlled by the applied dc-voltages, as observed by Plecis et al. [191]. The additional hydrodynamic pressure allowed control of the particle migration without influencing the electrical double layer.

When describing the analytes migration, especially the deflection, additional electrokinetic effects like dielectrophoresis had to be considered. To exclude deflection based on dielectrophoresis, the inhomogeneous electric field at the nanoslit was numerically calculated (COMSOL). With equation (2.15) and equation (2.16) the polarizabilities of the nanobeads were estimated. Based on these results the dielectrophoretic potential was significantly smaller than the thermal energy. Hence, dielectrophoretic manipulation was excluded.

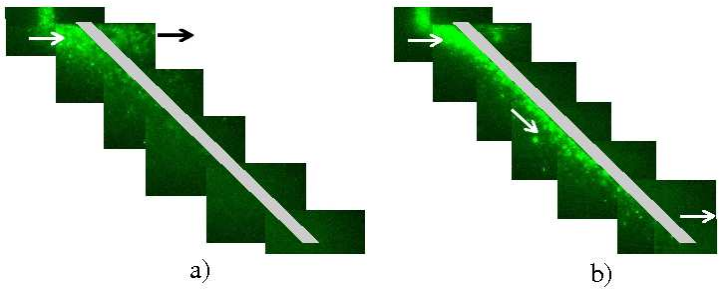

Figure 4.7: *Injection and manipulation of 20 nm nanoparticles at the tilted nanoslit (520 nm height) for different dc-voltages. Pressure was applied to reservoirs 1 (306 Pa) and 2 (469 Pa). a) dc-voltage of 5 V was applied to reservoir 3 without any deflection of the nanoparticles. b) 20 V with a significant deflection.*

After successful separation of 20 nm and 40 nm beads, the device was tested for manipulation of proteins. Streptavidin, size of 67 kDa, was used for manipulation experiments. A narrow stream of streptavidin was injected towards the nanoslit and deflected for appropriate dc-voltages and pressures (see figure 4.8 a). If the voltage was switched off, the streptavidin passed the nanoslit unaffected (figure 4.8 b). Thus, it was possible to control the continuous-flow manipulation of streptavidin and deflection at the nanoslit.

The continuous-flow mode of separation allowed on-line adaption of the applied voltage and hydrodynamic pressure. Hence, real-time optimization of the separation efficiency and high reproducibility were capable. The current throughput of about 10 nl/min was promising. By parallelization or optimization towards higher flow rates, the throughput might be significantly increased.

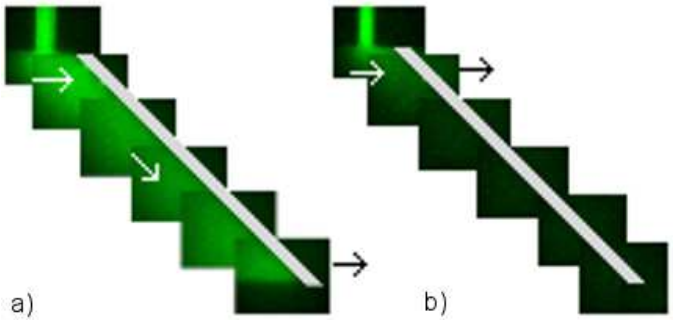

Figure 4.8: *Migration of streptavidin (67 kDa) at the nanoslit (520 nm height). By applying appropriate dc-voltages (4 V) and pressures (265 Pa at reservoir 1 and 408 Pa at reservoir 3) streptavidin was deflected at the nanoslit. b) If the voltage was switched off, the streptavidin passed the nanoslit unhindered.*

4.3 Concept of dielectrophoretic mixing and separation

With the electrostatic sieving mechanism, a novel tool for continuous-flow separation of nanoobjects was introduced. Continuous-flow processing exhibited several advantages, like fast response-time, up- and downstream applications and on-line adaptability, thus it is of very high interest for μTAS. Since the electrostatic sieving relied on very low ionic strengths (see section 4.2), especially for biological active probes, a different continuous-flow separation mechanism was requested. With electrodeless dielectrophoresis, a non-invasive technique was developed that allowed continuous-flow manipulation in a biocompatible environment.

For the dielectrophoretic manipulation dc- and ac-voltages were applied to actuate the microfluidic chip. The resulting dynamical behavior was governed by linear and non-linear electrokinetic effects of electric field $\vec{E}(r,t)$, at location r and time t. Due to the applied external voltages several effects occurred. Here, the focus was on the dominating electrokinetic effects of electroosmotic flow, electrophoresis, and dielectrophoresis, whereas the effect of thermal noise and joule heating are discussed later on.

The resulting particle velocity by the applied electric fields can be written as [56]

$$\vec{u} = (\mu_{eo} + \mu_{ep})\vec{E} + \mu_{DEP}\nabla \left|\vec{E}\right|^2 \quad . \tag{4.2}$$

In equation (4.2) the similitude of electroosmotic flow and electrophoresis (*cf.* section 2.3.3) was assumed. Since the net particle migration was averaged out for the frequencies used in the experiments (300-650 Hz, see section 4.5 and section 4.4), the ac-voltages did not contribute to electroosmotic flow or electrophoresis.

Additionally, the dc-component of $\vec{E}$, denoted as $\vec{E}_{dc}$ was much smaller than the oscil-

lating sinusoidal voltage signal, denoted as $\vec{E}_{ac}$, namely $\left|\vec{E}_{dc}\right|^2 \ll \left|\vec{E}_{ac}\right|^2$ (see section 4.5 and section 4.4). Hence, the contribution of the dc-component could be neglected for dielectrophoretic motion.

With these assumptions equation (4.2) was written as time-averaged form [56]

$$\bar{\vec{u}} = (\mu_{eo} + \mu_{ep})\vec{E}_{dc} + \frac{1}{2}\mu_{DEP}\nabla\left|\vec{E}_{ac}\right|^2 \quad . \tag{4.3}$$

The quintessence of equation (4.3) was, that both electrokinetic effects, linear as well as non-linear, were controlled separately. The linear effects were governed by dc-voltages and the non-linear effects by ac-voltages.

Generally, in the used devices two regions could be distinguished for the migration of particles. The first region was far away from the nanoslit, where the electric field was practically uniform. In this region, the migration of particles was solely governed by the linear electrokinetic effects. The dielectrophoretic forces and migration needed spatial inhomogeneities in the electric field, as could be clearly seen in equation (2.12) and equation (4.3). Thus, dielectrophoresis was neglected for particle migration except for the region of the insulating ridge, where spatial inhomogeneities occurred. In that region linear as well as non-linear electrokinetics had to be taken into account.

For all dielectrophoretic mixing and separation experiments, curved ridges were used. Simulations of the dc electric field at the ridge revealed, that the electric field had a small component tangential to the edge of the ridge (see figure 4.9). As already analyzed by Hawkins et al. the relative strength of this component depended on the inclination angle of the electric field and the ridge [66]. It became maximal, if the ridge was parallel to the long channel axis and *vice versa* for the ridge perpendicular to the long channel axis. In contrast, the dielectrophoretic force was oriented perpendicular to the edge of the ridge [56]. The direction of the dielectrophoretic force depended on the polarizability of the analyte. For positive α (DNA) it pointed towards the edges, i.e. a dielectrophoretic well was formed. Whereas for negative polarizability (nanobeads), it pointed away from the edge, i.e. a dielectrophoretic hurdle was formed.

When combining the electroosmotic/electrophoretic and dielectrophoretic effects the resulting migration varied along the ridge. For instance, dielectrophoretic forces were practically absent where the ridge merged tangentially with the channel wall, generating an entrance to the dielectrophoretic trap (see figure 4.10).

The path of a particle was governed by the relative magnitude of the acting forces, linear and non-linear, that could be controlled separately. Theoretically, the voltages could be tuned such that either dielectrophoresis was negligible or much stronger than the linear effects. In the first case, a polarizable object would pass the ridge unhindered, dominated by linear effects, whereas in the second case, it would be deflected along the ridge. These two different cases with the corresponding types of dynamical behavior formed the basic working principle of the dielectrophoretic continuous-flow manipulation.

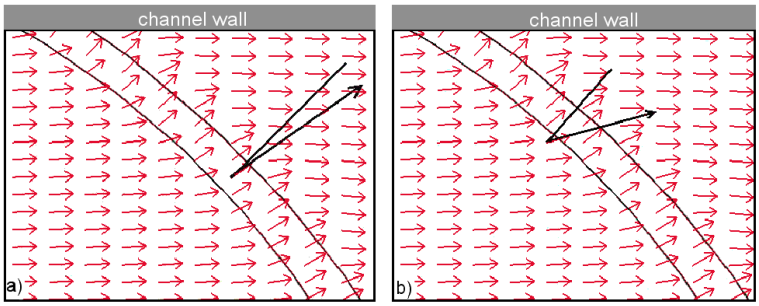

Figure 4.9: *Numerical simulation of normalized electric field* ($\vec{E}/\left|\vec{E}\right|$) *at a section of the ridge. The increase in magnitude of the electric field was not resolved but could be calculated by the ratio of the full height and nanochannel height. For illustration, the lot to the edge was indicated by a black line, and the direction of the electric field at the same point was depicted by the black arrow. Since an angle between these occurs, the electric field had a component tangential to the ridge, responsible for transport along the ridge. Additionally, downstream of the ridge the electric field had a component pointing towards the channel wall. Hence, the analytes were focused towards the channel wall.*

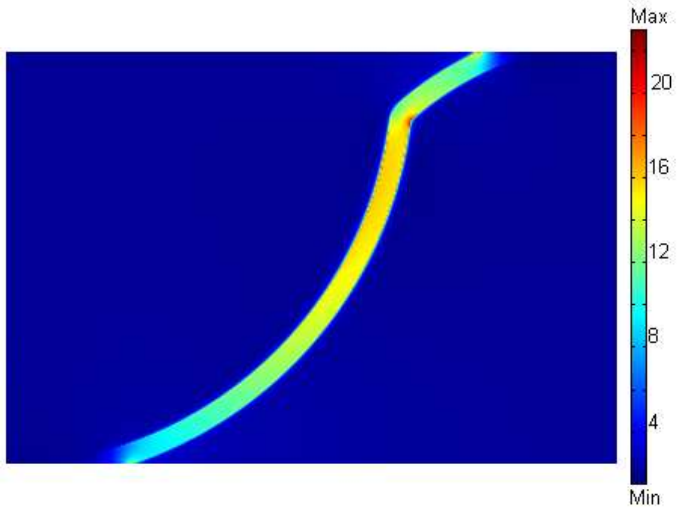

Figure 4.10: *Numerical simulation of* $|\vec{E}|^2$*, the dielectrophoretic potential, at the ridge (top view). The strength of the potential is color-coded. In a tiny region around the edges the dielectrophoretic potential exhibited maxima, i.e. strong forces appeared. The strength of the potential altered along the ridge with a local maximum at the inflection point, whereas at the channel walls minima appeared, forming "entrance" and "outlet" to the potential.*

For two species of sufficiently different electrokinetic (electrophoresis, electroosmosis, dielectrophoresis) mobilities, the dc- and ac-voltages might be tuned that way, that one sort was totally deflected at the ridge, whereas the second (less polarizable, smaller object due to equation (2.16)) passed the ridge unaffected. Accordingly, a mixture of these two sorts would be separated at the nanoslit. For the case *vice versa*, mixing of objects, the two analytes were injected from different channels (see section 3.5) and the larger one was deflected along the ridge and merged with the second particles stream at the end of the ridge.

Experimentally, some limitations were present, for example, the range of voltages was limited due to the experimental setup and the investigated probes. For example, for too high voltages dramatic Joule-heating effects occurred and would either destroy the (bio)molecule or the device itself or led to thermo driven flow that could negatively influence the trapping [193, 194]. In recent publications it was found that electrothermal flow, induced by joule heating, caused recirculating flows [195, 196]. It was also mentioned in literature that the ratio of the nanoslit and the free channel heights $r_{height} = h_{micro}/h_{nano}$ critically influenced the recirculating flow, i.e. if a specific ratio was exceeded no recirculating flow appeared [195]. Hawkins et al. found a critical ratio of $r_{height} > 6$ where the recirculating flow was suppressed (in this work the ratio was above 6 for all devices). The electrothermal flow, hence the circulations, directly depended on the strength of the electric field, thus on the applied voltages [196]. To reduce the Joule heating the applied voltage had to be minimized. This was in direct conflict to the dielectrophoretic manipulation as for successful manipulation the dielectrophoretic potential (electric field) had to exceed a critical value [56]. This problem was solved by adaption of the nano-microfluidic devices such that the necessary dielectrophoretic potential was achieved for appropriate voltage

To estimate the minimal necessary electric fields, the polarizability or at least the order of magnitude of the investigated objects had to be known. Under the assumption that the dielectrophoretic potential had to overcome the thermal energy, the necessary electric fields were calculated with equation (2.17). With $E \propto \xi U$ the necessary voltages were calculated by an equivalent circuit diagram. ξ denotes the geometrical factor of the device at the nanoslit. The dielectrophoretic potential could be written as $W_{DEP} = \xi \alpha U_{ac}^2$.

For separation as well as for mixing a continuous escape of the analyte out of the dielectrophoretic potential was necessary. Generally, the escape was theoretically described by the Kramers rate (see section 2.6). Hence, the escape events were statistically distributed. As a consequence, after a defined time, the streams of in coming and out going analytes should have been in equilibrium. But in the experiments, a continuous escape could only be detected if a minimal amount of analyte had accumulated at the end of the ridge. To describe these experimental observations, additional to thermal activated escape, a steric effect was assumed. This could be verified by simulations, where the mean time for escape was in the range of the experimental observations only if steric effects were taken into account *via* a DLVO potential [197].

As assumed in theory and confirmed in experiments, the migration along the ridge de-

pended on the layout, due to the angle dependence [56, 66]. Thus, the layout of the ridges was optimized according to particles migration and escape process. The first design consisted of an arc-shaped ridge (see figure 4.2 f). The experiments revealed that the migration along the arc was adequate but the mean escape time was about (30 s). A close look to the electric field direction and strength at the ridge gave a hint to the migration mechanism. Based on the perpendicular orientation of the ridge close to the wall the dielectrophoretic potential became maximal, whereas the linear effects became negligible.

To fasten up the escape, the ridge layout was designed s-shaped. Simulations of the electric field revealed that by the s-shape the dielectrophoretic potential close to the channel walls was reduced forming an "entrance" and an "outlet" (*cf.* figure 4.10), where the particles could easily enter or leave the ridge. Experimentally, a significant decrease of escape times was observed. But one disadvantage appeared; the particles accumulated at the inflection point and escaped out of the trapping potential. That was according to the higher retention time due to the angle dependent migration velocity and dielectrophoretic potential, i.e. the particles migration was retarded at the inflection point that exhibited a local extremum of the dielectrophoretic potential (see figure 4.10). Since the retention time was increased at the inflection point, the particles statistically escaped from the ridge (figure 4.11). So the next development of the ridge layout was towards an asymmetric s-shape, i.e. the inflection point was moved towards the end of the ridge (figure 4.2 a). The experiments revealed that at this ridge analyte of positive dielectrophoresis, migrated of adequate velocity and escaped easily, when the ridge merged tangentially with the channel wall. In the case *vice versa*, negative dielectrophoresis, the analytes accumulated at the end of the ridge before they escaped, but the time was significantly reduced.

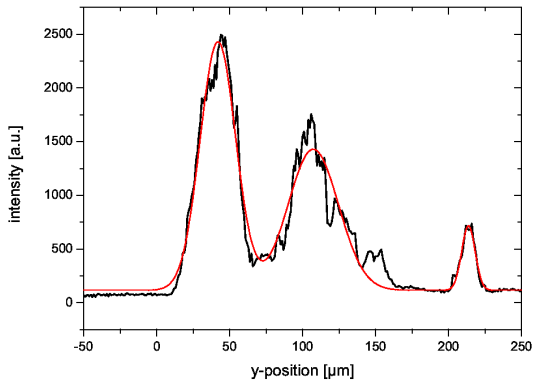

Figure 4.11: *Fluorescence intensity plot downstream of s-shaped ridge for separation of two DNA species. Three peaks appeared downstream of the ridge, indicating three distinct streams of analyte, although only two species were in the mixture. The analytes escaped at the middle position because of the high dielectrophoretic potential at the inflection point and the consequential increased retention time. Thus, the probability of escape at the inflection point was significantly increased.*

After optimization of the ridge layout, experiments of mixing and separating 100 nm and 20 nm particles were performed (see also section 4.4) as well as simulations of trajectories (see figure 4.12). The simulations were according to the experimental conditions (electric field, dielectrophoretic potential, layout of the ridge, velocity of beads). They proved that the mechanism of the continuous-flow processing could be modeled in very good agreement to the experimental results when considering these parameters.

Additionally, by theoretical evaluation the minimal difference in particle radius Δr was determined for sufficient separation under the given experimental conditions. Therefore, simulations for variable bead sizes below 100 nm were performed such as the radius, respectively the polarizability, of the smaller particles was varied to larger sizes (below 100 nm) and the electrokinetic migration behavior was observed. It was assumed that the electroosmotic/electrophoretic migration behavior would not alter for varying sizes according to equation (2.10) and equation (2.11) and that the dielectrophoretic migration depended on the (size dependent) polarizability. It was expected that a transition of "no deflection" to "fully deflection" would be observed when the dielectrophoretic potential overcame the electroosmotic/electrophoretic migration. The simulations revealed that this transition occurred in a small range of increasing particle sizes. The minimal size of particles being deflected was little larger than 70 nm in diameter, i.e. perfect separation of a mixture of 100 nm and 70 nm beads could be achieved. Thus, efficient and perfect separation under the current experimental conditions was possible for nanoparticles that differed by about 30% in size [56].

Further enhancement of the device layout, i.e. layout of the ridge and channel widths and heights, and adaption of the applied voltage amplitudes and frequencies is expected to increase the separation efficiency as well as the separation sensitivity.

The system described above was optimized for a "binary response", i.e. the analyte had two possible pathways at the ridge. Either the analyte passed the nanoslit unhindered or was deflected towards the other channel wall. As a consequence, a mixture of two species could be separated into its components.

Hawkins et al. suggested that analytes of different polarizabilities would escape from an arc-shaped ridge at different locations, due to angle dependent migration. Thus, separation of more complex mixtures should be possible at one single arc-shaped ridge [66]. But neither they nor we could observe such a behavior. Hence, a different approach was necessary to separate mixtures of three or more species.

Generally, two different approaches were possible. 1) The ridge could be structured stair-like, i.e. each step would differ in dielectrophoretic potential. So, at each step one species, that is less polarizable, would leave the ridge. Production of this device would need more than two contact lithographic steps, thus would be more sophisticated. 2) The channel could branch downstream of the ridge into two channels. One of the branches would contain an additional ridge. Due to the channel geometries, the dielectrophoretic potential at the second ridge could be set to different values. Thus, a mixture of three analytes could be separated into its components. For mixtures of higher complexity, the channel has to split

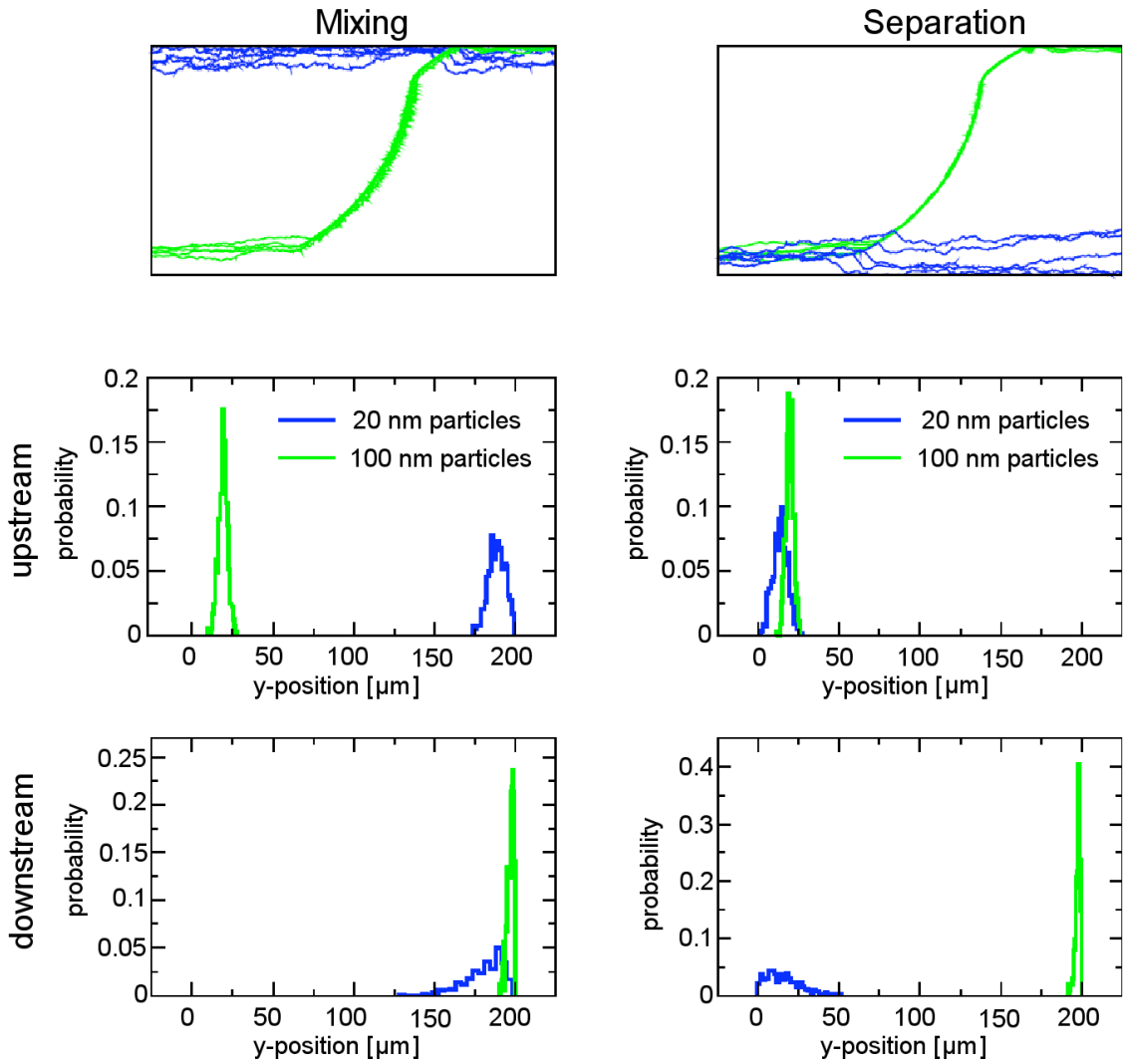

Figure 4.12: *Numerical simulation of mixing (left column) and demixing (right column) of 20 nm and 100 nm. In the first row, typical trajectories of nanobeads (exhibiting negative dielectrophoresis cf. section 4.4) are shown. The second and third row illustrate the particle distributions along the y-direction up- and downstream of the ridge as obtained from simulating 500 particle trajectories for each species.*

in an increasing amount of channels.

In this work, the latter route was followed, because of the easiness of fabrication, since the production process of the masterwafer was all the same. Up to the first ridge, the device looked the same as for the binary separation. Additionally, downstream of the first ridge the channel split up into two branches one of them with the second ridge (see figure 4.13).

When designing the device for multiple-separation, some boundary conditions had to be considered. For example, the resistance of both branches had to be the same, otherwise the analyte would follow the path of minimal resistance. Additionally, the channel geometries like length, width, and heights of the micro- and nanochannels influenced the strength of the electric field at the ridge and thus the dielectrophoretic potential. The geometrical factor ξ gave the ratio of the applied voltage and the resulting electric field at the nanoslit. It depended on the geometrical parameters. From previous separation experiments of two species the minimal electric field for successful separation was known for nanobeads as well as for DNA. Hence, the device layout for multiple-separation was designed such that the necessary field was achieved for less high voltages.

As was described above, diffusion is significant in microfluidics. Thus, in the experiments the analyte stream widened due to Brownian motion (*cf.* figure 4.16) and for multiple-separation the second ridge had to be as close as possible to the first ridge, to minimize this effect. The two branches of the first device were arranged with an angle of 45° with respect to the main channel (see figure 4.13 a). By this design, the distance between the two nanoslits was too long and efficient separation was prohibited by the wide stream downstream of the first ridge. Hence, a second device was designed with the second ridge in line with the first. As a consequence, the distance between the two ridges was significantly reduced, minimizing the diffusion based broadening during experiments. Hence, when designing a multiple-separation device, at least these were the basic parameters to consider.

The final layout is depicted in figure 4.13 b). As can be seen the ridges were arranged in a linear channel. This revealed two advantages. 1) The "free" way in between two ridges was minimized. 2) Fluorescence intensity scans of both separation steps were easily to perform, since the orientation was all the same. The devices were designed such that the middle sized and largest analytes were deflected at the first ridge, hence separating the smallest one. Whereas at the second ridge, the larger analyte was deflected and the middle-sized species passed the ridge unhindered. In consequence, the electric field at the second ridge had to be less than for the first ridge.

For each channel design two different layouts were used that varied in channel width of the second ridge resulting in two different ξ, thus ratios of electric fields. The first device consisted of two ridges, both over a channel width of 200 μm, thus the electric field of the first ridge was twice of the electric field of the second ridge (2:1). For the second device the first ridge was over a channel width of 200 μm and the second ridge over a channel width of 150 μm. Thus, the resulting ratio of electric fields was 1.5:1 for the first to the second ridge. The heights of the nanoslits were the same at both ridges, due to the fabrication process of the masterwafer. The height of the nanoslits did not influence the ratios of the

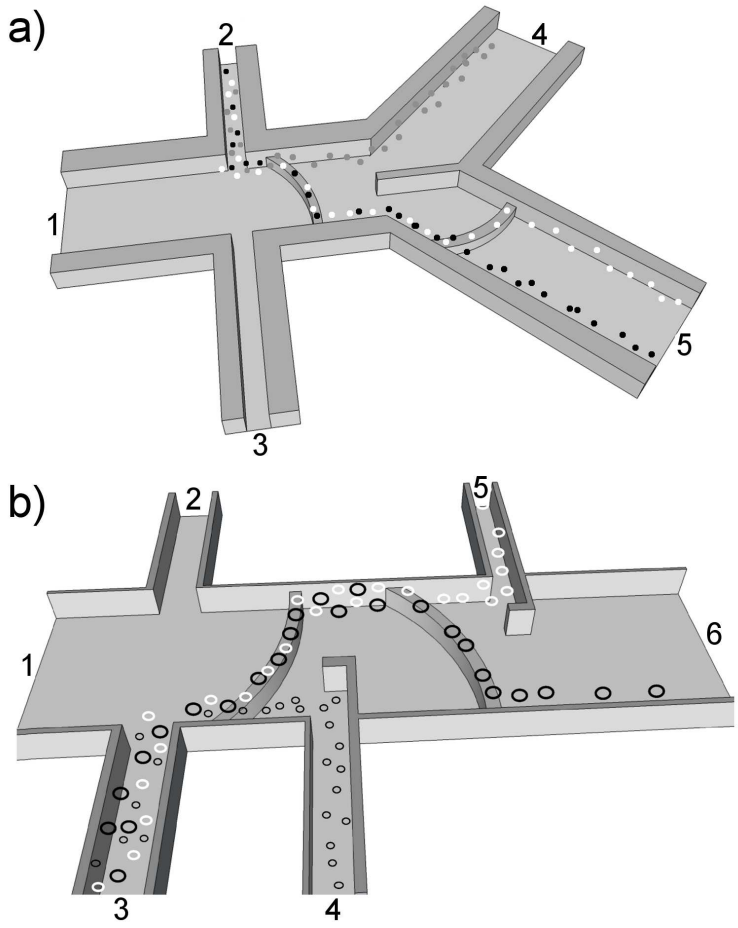

Figure 4.13: *Sketches of the device layouts for multiple-separation. The devices were designed such that at the first ridge the middle sized and the largest analytes were deflected, whereas the smallest passed the ridge unhindered and were separated from the mixture. At the second ridge the electric field was reduced, so only the larger analyte molecules were deflected. The ratio of the electric fields at the ridges was adapted by the channel widths (see text). a) First layout, due to the orientation of the two branches the distance between the ridges was too large. Thus, the separation efficiency was significantly diffusion limited. b) Second, enhanced layout. The two ridges were in one linear channel. Thus, the distance could be significantly reduced, enhancing the separation efficiency. Additionally, all three analytes were collected in separate outlets.*

electric field.

The experimental procedure for multiple-separation was the same as for a mixture of two species, i.e. first, the dc-voltages were set for a narrow stream flowing towards the ridges, and second, the ac-voltage and frequency were varied until two streams were observed downstream of the first and the second ridge. Analogue to the binary separation, each trajectory was identified afterwards at the same conditions (see appendix figure 5.3).

4.4 Dielectrophoretic nanobead manipulation

In the next sections, dielectrophoretic manipulation of nanobeads will be presented. Mixing and separation experiments were performed in continuous-flow mode. The beads were driven *via* applied dc-voltages that induced an electroosmotic flow (see section 2.3.3), additional superimposed ac-voltage generated a dielectrophoretic landscape.

4.4.1 Mixing of nanobeads

In figure 4.14 the experimental results for the continuous-flow mixing and separation of 100 nm and 20 nm polystyrene beads are depicted. First, the nanobeads were mixed in continuous-flow mode. The results are shown in the left column of figure 4.14. The nanobeads were injected in two distinct streams towards the ridge (see section 3.5) by applying appropriate dc-voltages (see capture of figure 4.14). Superimposed ac-voltages of 600 Hz at 500 V generated the dielectrophoretic potential that caused a total deflection of the 100 nm beads along the ridge. When the beads reached the other channel wall, they passed over the ridge and merged with the second particles stream (20 nm beads).

A closer look revealed that the nanobeads were trapped right before the ridge, thus in the region of minimal electric field strength (*cf.* section 2.3.4), i.e. the 100 nm beads exhibited negative dielectrophoresis, which was in accordance to the theoretically predictions in literature [71, 149, 153, 198].

To specify the mixing efficiency, it was noted that all 100 nm beads were deflected at the ridge and did not pass the ridge until the other channel wall was reached. A detailed video analysis of the mixed stream was performed. Due to the different brightnesses of the two sorts of beads, visual inspection of the mixed stream clearly revealed the presence of both particle species. It was observed that the two sorts did not flow in parallel but were fully mixed due to the electrokinetic driving and the thermal motion. The throughput of the continuous flow mixing process was calculated by the channel geometries and the particles velocity with $j = v \cdot h \cdot w = 4.5$ nl/min. v denotes the particles velocity, h and w denote channel height and width.

In section 4.3 the particle trajectories and distributions were numerically simulated for the mixing of 100 nm and 20 nm beads (see figure 4.12). The simulations fit very well to the experimental results. Hence, it was confirmed, that the interplay of linear and non-linear electrokinetic effects constitutes the basic working principle. Thus, with that theoretical

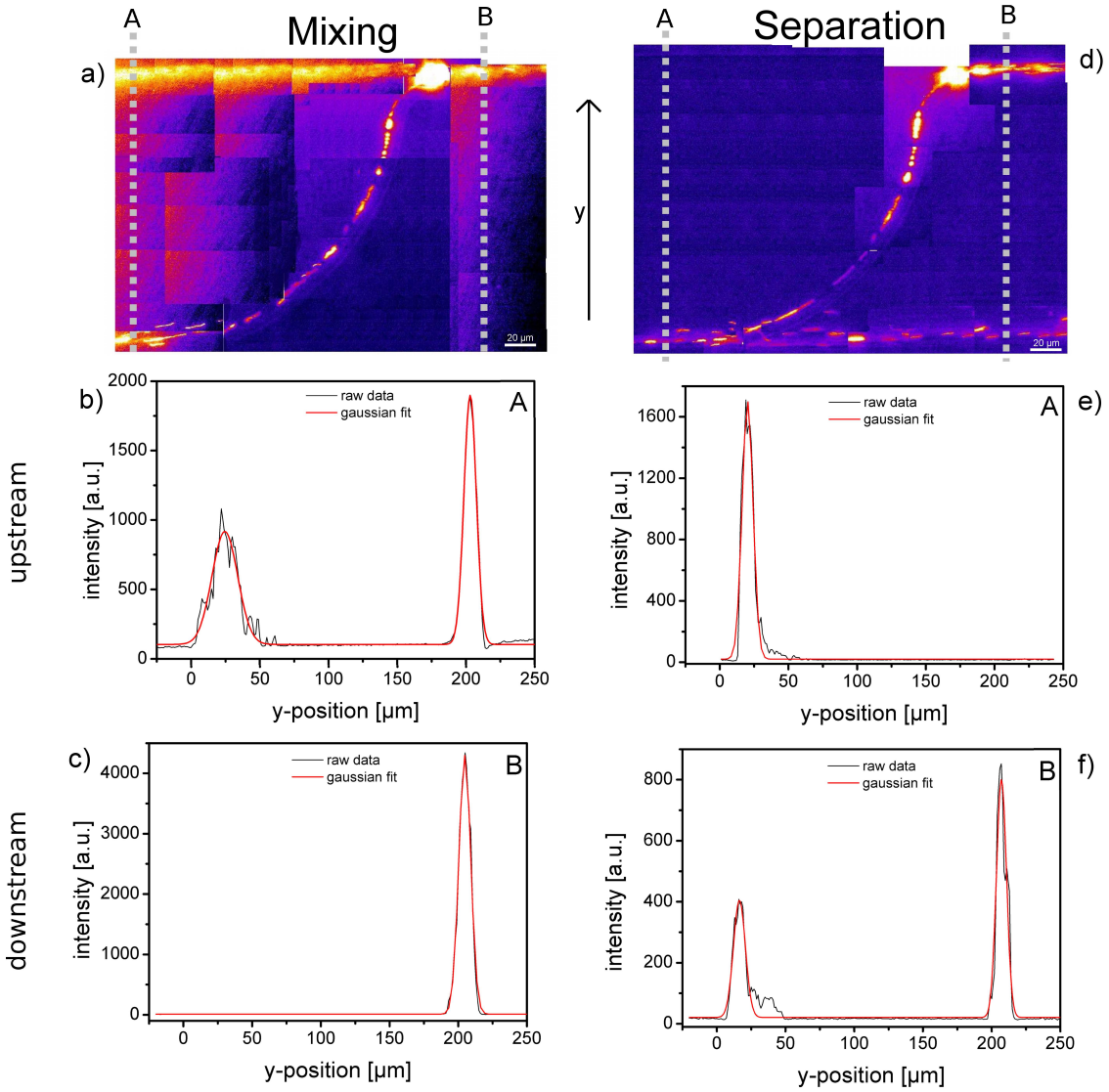

Figure 4.14: *Continuous-flow mixing and separation of nanoparticles at nanoslit of 620 nm height. a) and d) Collages of fluorescence microscopy images recorded during the experiments. The fluorescence intensities were analyzed along the dotted lines up- and downstream of the ridge (see section 3.5) to determine nanobead distributions. The beads flew from left to right. The results obtained upstream of the ridge are depicted in b) and e), the results from downstream of the ridge in c) and f). Black lines represent the measured distributions, red lines are Gaussian fits. In case of mixing (a-c), the throughput was 4.5 nl/min. The applied voltages during the mixing of 20 nm and 100 nm were: electrode 1 was grounded, -5 V dc and 500 V at 600 Hz ac were applied at electrode 2, 35 V dc at electrode 3, and 10 V dc at electrode 4. For separation (d-f), a single stream consisting a mixture of 20 nm and 100 nm flew towards the ridge. Downstream of the ridge, two distinct streams were visible with resolution Res = 5.96. The throughput of separation was 7.5 nl/min. The applied voltages for the separation were: electrode 1 was grounded, -40 V dc and 500 V at 600 Hz ac were applied at electrode 2, 5 V dc at electrode 3, and 15 V dc at electrode 4.*

model further optimization of the device is possible with numerical simulations. Further simulations can support the optimization process with respect to the ridge layout and the balance of the applied voltages to enhance sensitivity as well as efficiency. Additionally, by parallelization of several channels the total throughput could be increased.

For controlled mixing the beads had to escape from the ridge at a predefined region, i.e. into the second particles stream. The experimental results as well as the simulations proved the applicability of the novel devices to this requirement. Hawkins et al. used a similar device for continuous flow separation of microbeads [66]. In contrast to this thesis they used a slightly different shape of ridge (see figure 4.15). But for the different layout that was used by Hawkins et al. the escape process was not reproducible, since the beads did not escape at well defined regions but over a wide width (see also ref.[66]). So, only with the improved layout, demonstrated in this thesis, mixing became possible.

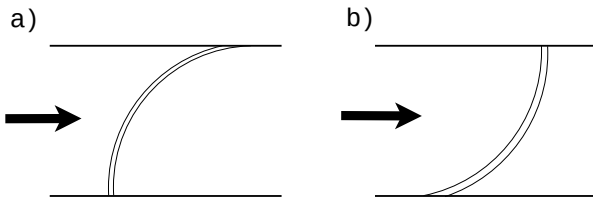

Figure 4.15: *Comparison of ridge layouts used by Hawkins et al. [66] a) and in this thesis b). The direction of flow is indicated by the arrows.*

Although a few microfluidic devices, that exploited dielectrophoresis, have been presented in literature, the presented device in this work was the first realization of continuous-flow electrodeless dielectrophoretic mixing. Tabeling recently reviewed some techniques for mixing within microfluidic devices [53]. Deval et al. and Lee et al. presented dielectrophoretic mixing devices that consisted of arrays of microelectrodes [74, 199]. Sin et al. used a ring electrode to dielectrophoretically mix analytes [76]. Besides mixing of two analytes, the present device could be used to transfer the analyte from one buffer solution into another one, i.e. "exchanging" the buffer for the analyte. A similar effect that was based on dielectrophoresis, was described by Tornay et al. [77, 78]. They used an array of microelectrodes to transfer particles from one buffer into another.

4.4.2 Separation of nanobeads

Binary separation After successful mixing of 20 nm and 100 nm beads, the process *vice versa*, separation, was performed. The experimental results of the continuous-flow separation of the 100 nm and 20 nm beads are depicted in figure 4.14 in the right column. As was described in section 3.5, a mixture of both particles was continuously injected towards the ridge as a narrow stream. The stream had a width of about 25 μm and thus occupied less than a quarter of the channel width. During the experiments, the ac- and

dc-voltages were tuned such that two distinct streams were observed downstream of the ridge (see caption of figure 4.14). Although the two sorts of beads could be distinguished by the difference in brightness, additional experiments were performed using either the 100 nm or 20 nm beads at the same conditions as for the successful separation. This confirmed that the 100 nm beads were deflected at the ridge towards the second channel wall, whereas the 20 nm beads passed the ridge unaffected. The 100 nm beads exhibited negative dielectrophoresis, i.e. they were trapped right before the ridge.

The separation started as soon as the mixture of the two particles reached the ridge where the 100 nm beads were deflected, i.e. about 30 s after the voltages were switched on. The migration of the beads along the ridge to the other channel wall took another 15 s. There the beads first accumulate until a continuous escape was observed. This took about 30 s. Thus, in summary the first 100 nm beads passed the ridge after about 1.25 min.

To determine the separation resolution the fluorescence intensity distribution downstream of the ridge was fitted with a Gaussian function (see figure 4.14 f). Thereby, a resolution of $Res = 5.96$ was calculated for the separation. Concerning the separation efficiency, it was found that 85 to 100 % of the beads were deflected (based on three independent experiments), so a perfect separation with baseline separated resolution was possible when choosing the right ac- and dc-voltages. To explain the not 100% of deflection, AFM images were taken of the nano beads to investigate the size distribution of the beads (see Appendix). The analysis of the size distribution revealed a mean particle size of 98 nm and a broad distribution (FWHM=10 nm) for the 100 nm beads. Depending on the particles size the dielectrophoretic migration behavior changed and smaller beads passed the ridge unaffected. Thus, the experimental findings agreed very well to the simulated trajectories.

The throughput of the continuous-flow separation was determined to 7.5 nl/min. By optimization of the device layout, i.e. shape of the ridge and channel width and height, and the applied ac- and dc-voltages as well as by parallelization of several channels the total through put could be further increased.

Multiple-separation Additional to the binary separation, i.e. separation of a mixture of two species, separation experiments with three species were performed. Therefore, a slightly different device layout was used. In figure 4.13 both devices that were used for the multiple-separation experiments are depicted. The multiple-separation of 100 nm, 60 nm and 20 nm beads, i.e. first experiments, were performed with device figure 4.13 a). To distinguish between the largest beads (100 nm) and the middle sized beads (60 nm), these were labeled with dyes of different fluorescence emissions (605 nm for 100 nm beads and 480 nm for the 60 nm beads).

As for the binary separation, the mixture was continuously injected towards the ridges by applying appropriate dc-voltages. For superimposed ac-voltages of 650 Hz at 500 V all of the 100 nm and most of the 60 nm beads (60%-90%) were deflected at the first ridge, whereas the 20 nm beads passed the ridge unaffected and were led into a separate channel.

At the second ridge, the 100 nm beads were deflected, too. In contrast to the 60 nm beads that passed the second ridge unaffected. Thus, a successful multiple continuous-flow separation of three sorts of beads was achieved.

To investigate the reasons for the reduced amount of deflected 60 nm beads at the first ridge, AFM-images were taken (see appendix figure 5.6). A wide size distribution was found with a mean particle diameter of 56 nm and FWHM=15 nm. Since the dielectrophoretic potential scales cubic with the particles radius (*cf.* equation (2.16)) the unaffected beads were just too small to be deflected by dielectrophoresis. A more detailed evaluation of the distribution revealed that particles larger than 52 nm were deflected at the first nanoslit.

Due to the small channel dimensions the diffusion was not negligible (see section 2.5) and resulted in a stream broadening downstream of the first ridge (see figure 4.16). The 100 nm beads were concentrated at the second nanoslit, but the 60 nm beads passed the ridge unaffected as a wide stream. To minimize the broadening downstream of the first ridge the length between the ridges was reduced (see figure 4.13 b). The enhanced layout was used for multiple-separation of three species of circular DNA (see section 4.5.1)

When introducing a new technique, a discussion of given approaches is necessary. Concerning continuous-flow separation of beads by dielectrophoresis, several approaches have been published. In contrast to the ridge assisted dielectrophoresis, presented in this thesis, Church et al. used a curved channel to continuously separate 2.2 μm and 5 μm beads [134]. Therefore, the channel was arranged in serpentines over a length of 1 cm. Several other groups used insulating obstacles, e.g. blocks or oil droplets, for dielectrophoretic continuous-flow separation of microbeads, sizes between 5.7 μm and 15.7 μm, [64, 67, 200]. Gallo-Villanueva et al. used two arrays of posts that differed in post distances [135]. Thus, two regions of varying dielectrophoretic potential were created. They could separate 1 μm and 4 μm beads into different outlets. In contrast to the 2-dimensional structures other groups used, Barret et al. fabricated 3-dimensional linear ridges (slit height of 5 μm) for separation of micrometer-sized *B.Subtilis* and 200 nm particles [68].

The first devices used in this thesis were inspired by the work of Hawkins et al. [66]. Their device consisted of a curved ridge that created a slit of 100 μm height. Hawkins et al. demonstrated at this ridge a continuous-flow separation of 2 μm and 3 μm particles. In contrast to their work, in this thesis the height of the slit was significantly reduced allowing dielectrophoretic continuous-flow separation of nanobeads for the first time. Additionally, the layout of the device was optimized to an asymmetric-s shape, due to enhanced separation performance of nanobeads.

To summarize the dielectrophoretic nanobead manipulation: mixing and separation of nanobeads was performed in one single device, just by corresponding injection of analytes. Beyond binary separation, successful realization of continuous-flow separation of three nanobead species was presented. To combine mixing and downstream analytical separation, one might think of a device similar to the multiple-separation, i.e. consisting of two nanoslits. At the first ridge nanobeads with anticipated binding sites would be mixed with the stream consisting of the binding partner, e.g. to purify DNA solutions or detect

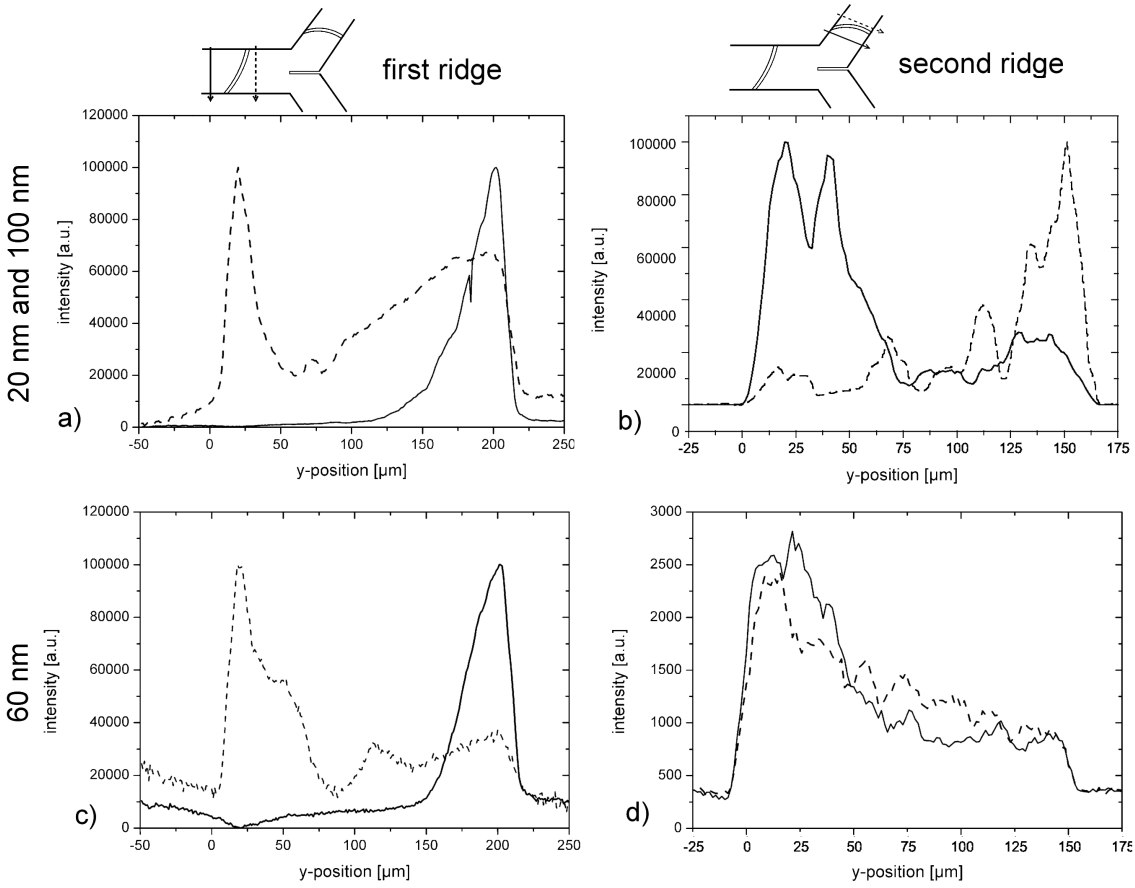

Figure 4.16: *Results of the multiple-separation of 100 nm, 60 nm, and 20 nm beads. Fluorescence intensity scans up- and downstream of the ridges (asymmetrically s-shaped, height of 500 nm). The 100 nm, 20 nm and the 60 nm beads were differently stained, unfortunately, they were visible as glowing in the filter of the other beads, respectively. The applied voltages were: 6 V dc and 650 Hz at 500 V ac were applied at electrode 1, 4.5 V dc at electrode 2, 10 V dc at electrode 3, electrodes 4 and 5 were grounded. a) Downstream of the first ridge (200 µm channel width) two peaks appeared depicting the 100 nm and 20 nm beads. The 20 nm peak downstream of the first ridge was broadened due to the unaffected 60 nm beads. The 20 nm beads were induced into a separate outlet. b) The 100 nm beads were fully deflected at the second ridge (150 µm channel width). c) Most of the 60 nm beads (60-90%) were deflected at the first ridge. d) The 60 nm beads passed the second ridge unaffected.*

specific antigens or antibodies [32, 36, 201].

4.5 DNA manipulation and characterization by dielectrophoresis

The previous experiments were performed with artificial particles (polystyrene beads). In the next sections, the applicability of the nano-microfluidic device to biological probes, i.e. DNA and DNA-complexes, is presented.

4.5.1 DNA separation

Binary separation The separation experiments were performed with two topological DNA variants, 1) linear DNA of 6.0 kbp and 2.686 kbp, 2) circular DNA of parental plasmid DNA (6.766 kbp) and its corresponding miniplasmid (4.474 kbp) and *minicircle* DNA (2.247 kbp). For the proof-of-concept of continuous-flow DNA separation, a mixture of linear DNA-molecules was injected into the separation channel by applying appropriate dc-voltages (see capture of figure 4.17 a). A superposition of ac-voltages of 350 Hz at 650 V caused two distinct molecule streams, downstream of the ridge. The two species were tested separately, afterwards, under identical conditions to identify the respective species trajectories (see appendix figure 5). The identification revealed, that the 6.0 kbp DNA was deflected at the ridge, whereas the 2.686 kbp DNA passed the ridge unhindered. The trapped and deflected DNA exhibited positive dielectrophoresis, i.e. the DNA was trapped at the region of highest electric field, on top of the ridge. This was in agreement to previously published data, were DNA exhibited positive dielectrophoresis, too [125, 155].

For a quantification of the separation efficiency, the fluorescence signals over the whole channel width were determined up- and downstream of the ridge (figure 4.17 b) and c), respectively). The scan upstream of the ridge revealed a single narrow peak. This peak corresponded to the molecules stream used for continuous injection. Downstream of the ridge two distinct peaks were observed, relating to the two separated DNA species. A resolution of $Res = 2.66$ was calculated. That corresponded to a baseline separated resolution. Besides resolution, throughput was evaluated to characterize the separation. For the separation of linear DNA, 2.686 kbp DNA and 6.0 kbp DNA, a throughput of 2.5 nl/min was achieved for one single device. By optimization of device layout and parallelization of several channels, the throughput could be increased.

One of the advantages of the continuous-flow processing was the quasi non-existing separation time, since the separation started the moment the molecules reached the ridge (15 s after starting the experiment). For migration along the ridge, the molecules needed another 30 s. Hence, first results, e.g. for purification control, were obtained within less than one minute. Despite the fast response time the resolution of $Res = 2.66$ was very competitive to other gel free microfluidic techniques [13, 202, 203].

In microfluidic applications, the ionic strength was one critical parameter if voltages were applied [43]. The most obstructive effect of the ionic strength was Joule heating, i.e. the

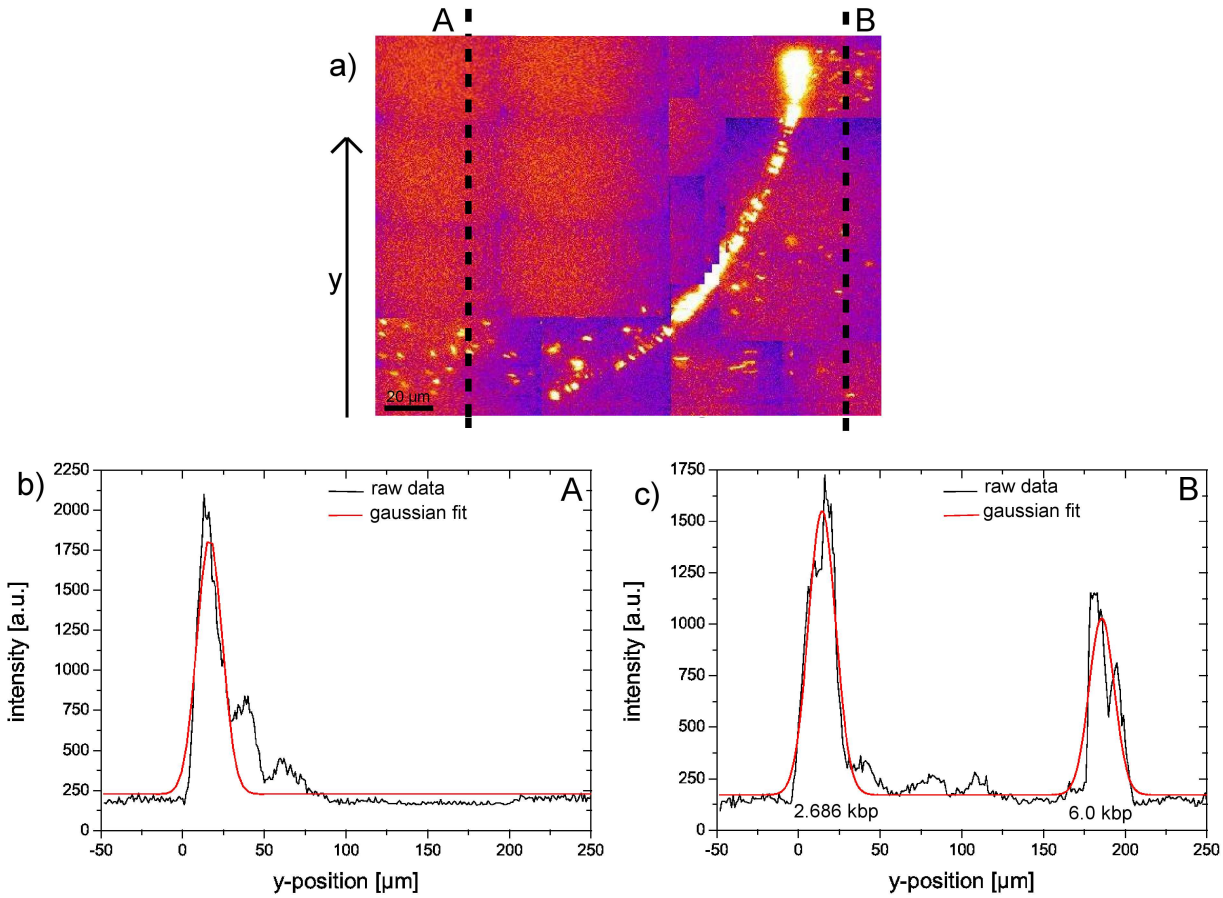

Figure 4.17: *Continuous-flow separation of DNA molecules at nanoslit of 670 nm height. a) Collage of fluorescence microscopy images recorded during the experiment. The fluorescence intensities were analyzed along the dotted lines up- and downstream of the ridge (see section 3.5) to determine DNA molecules distributions. The results obtained from upstream of the ridge are depicted in b), the results downstream of the ridge in c). Black lines represent the measured distributions, red lines are Gaussian fits. A single stream, consisting the mixture of 6.0 kbp and 2.686 kbp DNA, flew towards the ridge. Downstream of the ridge, two distinct streams were visible with resolution of Res* = 2.66. *The throughput of separation was 2.5 nl/min. The applied voltages were: -7 V dc and 350 Hz at 650 V ac at electrode 1, -7 V dc at electrode 3, and 2 V dc at electrode 4. Electrode 2 was grounded.*

temperature of the buffer increased due to resistive heating [193, 194, 204, 205]. Based on the Joule heating the temperature might cause analyte or device damages. The impact of Joule heating strongly depends on the ionic strength and decreases for low ionic strength [205]. Hence, in this thesis buffer with low ionic strength, 1 mM phosphate buffer, was used.

The ionic strength affected the dielectrophoretic force [131, 155, 164, 165]. Experiments at higher ionic strength (10 mM phosphate buffer) were accomplished to prove the general applicability. 6.0 kbp DNA was injected towards the nanoslit and was fully deflected at the ridge (see figure 4.18) demonstrating the ability to use buffer with higher ionic strength.

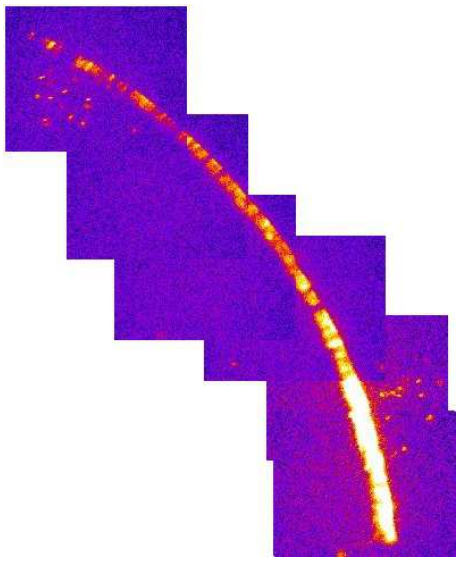

Figure 4.18: *DNA deflection at ridge with 10 mM buffer. Direction of flow was from left to right. 6.0 kbp DNA was trapped and deflected at the ridge (200 µm channel width and 670 nm nanoslit height, $U_{ac} = 650$ V, $\omega = 350$ Hz).*

The device proved efficient for separation of small linear DNA molecules. Since circular DNA becomes of increasing importance in medical applications, as for gene vaccination, separation experiments with circular DNA were performed in an enhanced device layout. The device was optimized due to the necessary ac-voltages. Therefore, the height of the nanoslit was significantly reduced to 180 nm over a channel width of 100 μm (see section 4.1). With that device a continuous-flow separation of *minicircle* DNA (2.247 kbp) and its parental DNA (6.766 kbp) was performed for ac-voltages of 350 Hz at 200 V (see figure 4.19).

A narrow stream of the mixture of DNA-molecules was injected towards the ridge. Downstream of the ridge two distinct peaks were observed. In additional experiments at identical conditions with single species the parental DNA was deflected (see appendix figure 5.2),

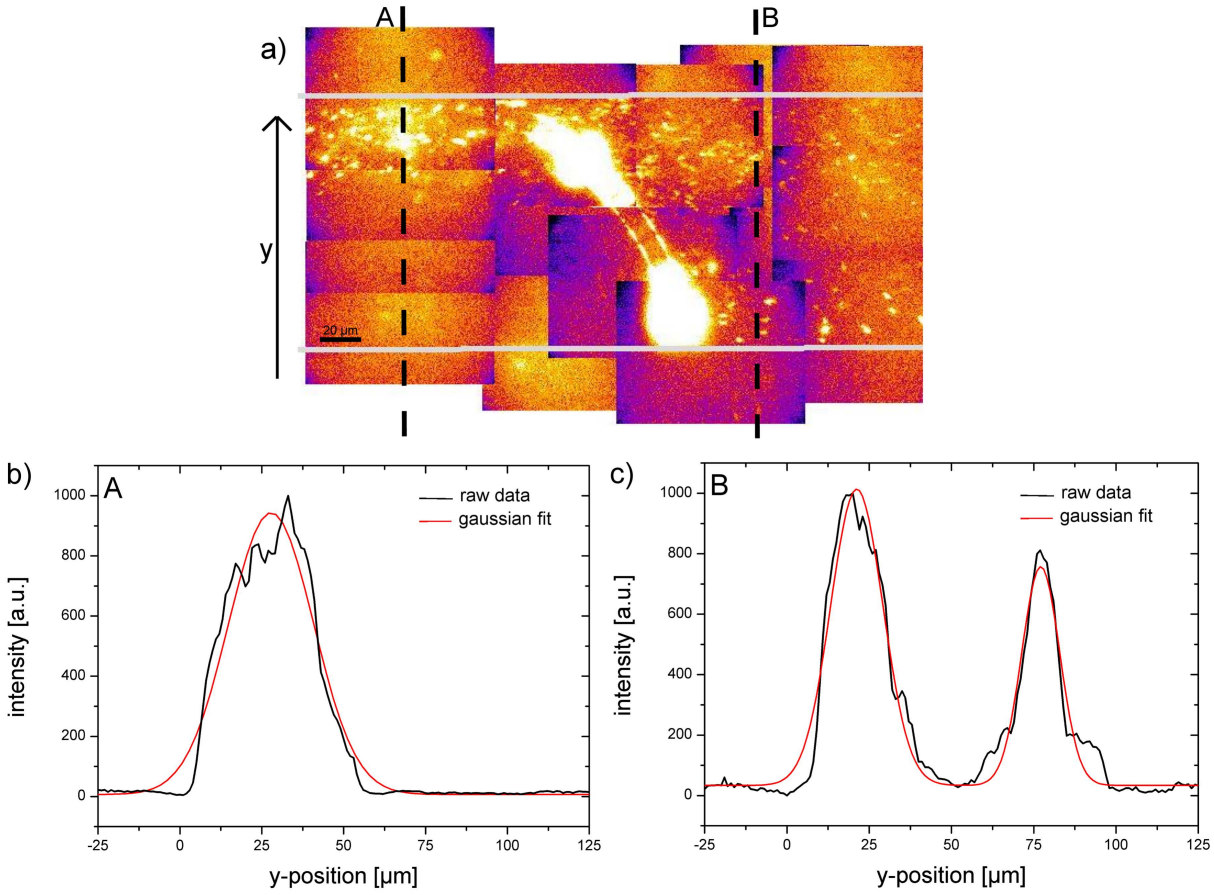

Figure 4.19: *Separation of parental and minicircle DNA (100 µm channel width and 180 nm nanoslit height, U_{ac} =200 V at ω =350 Hz). a) Collage of fluorescence microscopy images, the gray lines indicate the channel walls and the black dashed lines indicate the scanned paths. The fluorescence intensity was plotted against the y-position up- and downstream of the nanoslit (b) and c). Black lines represent the measured distributions, red lines are Gaussian fits. Downstream of the ridge two distinct streams were visible with baseline separated resolution of Res* = 1.24. *The applied voltages were: -7 V dc and 350 Hz at 200 V ac at electrode 1, -7 V dc at electrode 3, and 2 V dc at electrode 4. Electrode 2 was grounded.*

whereas the *minicircle* DNA passed the nanoslit unaffected. A close look to the downstream peaks revealed that the peak of unaffected DNA-molecules was narrowed with respect to the upstream peak. This was because of self-focusing. As was mentioned in section 4.3, the electric field had a component pointing towards the channel wall directly behind the ridge (figure 4.9). Thus, the DNA molecules were focused towards the channel wall.

The continuous-flow processing technique was developed due to the accessibility to downstream applications. A baseline separated resolution was indispensable for downstream applications. For the reduced channel width of 100 μm a baseline separated resolution of $Res = 1.24$ was achieved.

For separation of DNA the molecule length as well as the topological conformation were possible selection criteria [125]. Since the circular DNA -parental, *minicircle* or miniplasmid- might exhibit ccc- or oc-form, the conformation was tested during the production via CGE (capillary gel electrophoresis) [25]. 99 % of the DNA was in ccc conformation.

Comparing the necessary ac-voltages for separation of DNA at 670 nm high nanoslit, 650 V, and for separation at the 180 nm high nanoslit, 200 V, one advantage of the reduced nanoslit height became obvious. The necessary voltages were reduced by a factor of about 3, significantly reducing Joule heating that could degrade biomolecules.

The miniaturization towards a nanoslit of 180 nm in height offered two advantages, as the necessary voltages were reduced, and the range of manipulable molecules could be extended to even smaller DNA molecules. To calculate the minimal size of manipulable DNA molecules it was assumed that DNA molecules were deflected if the dielectrophoretic potential was the same as for the successful separation, already presented in the miniaturized device with $W_{DEP} = 4.56 \cdot 10^{-20}$ J. Thus, if the size/polarizability of the molecules decreased, the electric field, respectively applied ac-voltage, had to increase. The maximal applied ac-voltages were assumed to 600 V. Hence, DNA-fragments with polarizability of $4.4 \cdot 10^{-31}\ Fm^2$ could be deflected at the ridge. To calculate the number of base pairs N of the DNA molecule, it was exploited that $\alpha \propto N^{\nu}$ [125]. For exponent ν different values were discussed in the literature, varying between 3 for DNA of 120 bp [206] to 0.5 for DNA of about 6.0 kbp [125]. Thus, an exact value could not be calculated but the minimal DNA size should be between 3 bp and 80 bp.

Multiple-separation For the separation of nanobeads, a multiple-separation was realized for the separation channel branching into two side channels, one with an additional ridge. At that device, a multiple-separation of three nanobead species was demonstrated, but the resolution was diffusion limited (see section 4.4.2). Thus, an enhanced device was developed with reduced distance between the two nanoslits (see figure 4.13 b). With that nanofluidic device it became possible to completely separate parental (6.766 kbp), miniplasmid (2.474 kbp) and *minicircle* DNA (2.247 kbp) and led them into three different outlets.

In figure 4.20 a collage of the fluorescence microscopy images of the experiment is depicted. It is clearly visible that downstream of the first and the second ridge two molecule streams

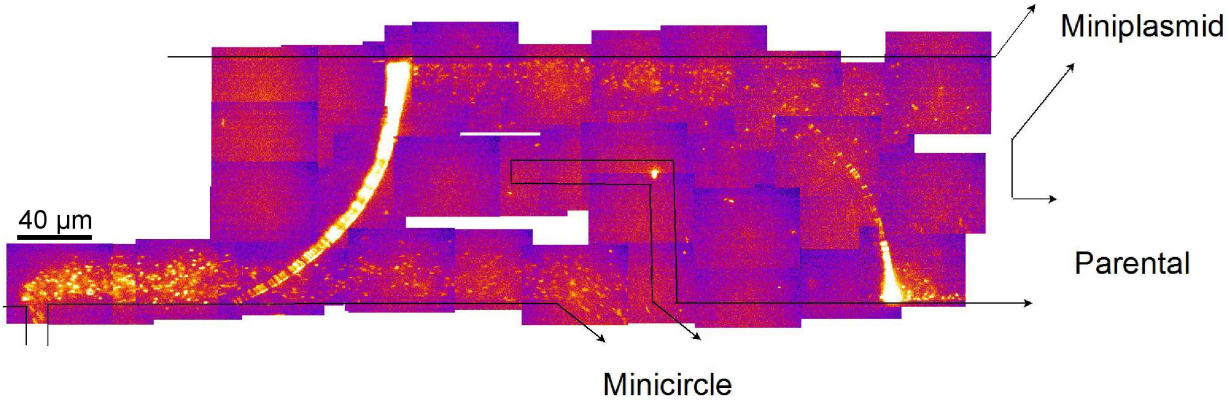

Figure 4.20: *Collage of fluorescence microscopy images for multiple-separation of parental DNA and its corresponding minicircle and miniplasmid DNA. The parental and miniplasmid DNA were totally deflected at the first ridge, whereas the minicircle DNA passed the nanoslit (500 nm height) unaffected. At the second ridge, only the parental DNA was deflected. Thus, a complete separation of the three species mixture was achieved. The ratio of the dielectrophoretic potentials at the first and the second ridge was determined to 4:1. The applied voltages were: -3V dc and 350 Hz at 250 V ac at electrode 1, -4 V dc at electrode 2, -1 V at electrode 3, electrodes 4, 5, and 6 were grounded. To determine the separation resolution the fluorescence intensity was evaluated downstream of the ridges see figure 4.21.*

were formed. At the first ridge the parental and miniplasmid DNA were deflected, whereas the smaller *minicircle* DNA was led into a separate channel. Since the dielectrophoretic potential was reduced by a factor of 4 at the second ridge, only the larger parental DNA was deflected. Thus, two molecule streams were formed. An evaluation of the fluorescence intensity distributions revealed that at both ridges a baseline separated resolution was achieved. Hence, a complete separation of three species was performed with very high separation efficiency.

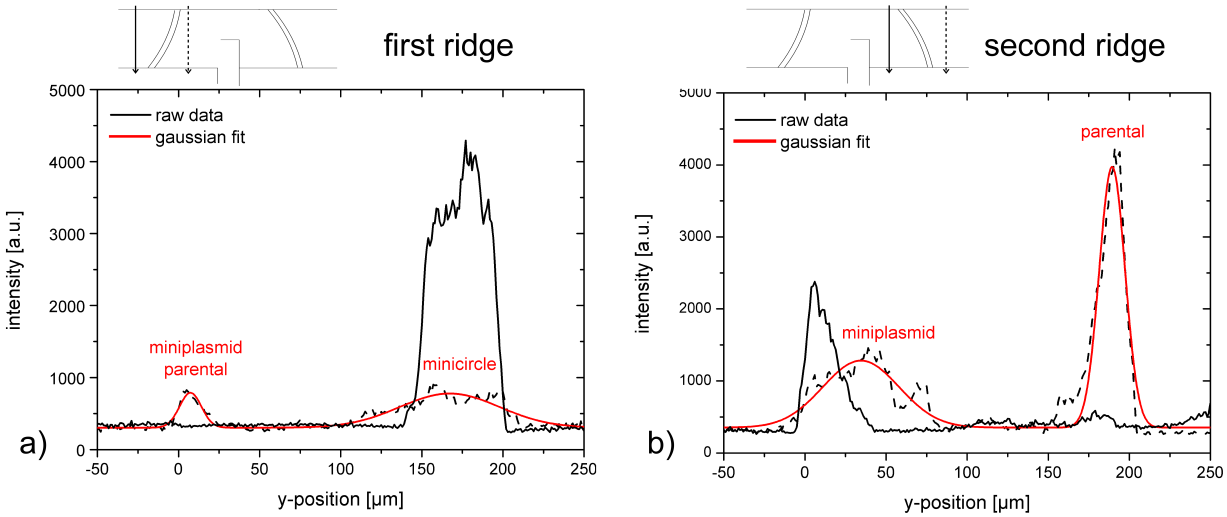

Figure 4.21: *Fluorescence intensities up- and downstream of the two ridges. The scan paths are depicted over the graphs, respectively. The black lines represent the scans upstream of the ridge, the dashed lines represent the scans downstream of the ridge. The red lines are Gaussian fits. a) Two peaks were visible downstream of the first ridge with baseline separated resolution of* $Res = 1.10$*. The minicircle DNA passed the ridge unhindered and was led into a separate outlet, whereas the parental and the miniplasmid DNA were deflected at the first ridge. b) Two peaks were visible downstream at the second ridge, representing the deflected parental DNA and the unaffected miniplasmid DNA. The throughput was 1.46 nl/min. With a resolution of* $Res = 1.25$ *a baseline separated resolution was achieved. Thus, a complete separation of the three species was performed with very high separation efficiency.*

In literature, microfluidic devices for continuous-flow separation were presented. For example, Fu et al. presented a patterned anisotropic nanofluidic device for continuous-flow separation of DNA molecules [13]. The advantage of their device was that they could separate DNA over a wide range of sizes, but its separation efficiency was limited by diffusion especially for short DNA molecules which separation mechanism was based on Ogston sieving. For long DNA molecules, the separation mechanism was based on entropic trapping. Hence, they could separate only linear DNA molecules. Fu et al. were able to separate mixtures of more than two species, but they did not achieve a baseline separated resolution.

In 2002, Huang et al. presented a DNA prism for continuous-flow separation of long DNA molecules [202]. They used an array of posts through which the DNA was driven by asymmetric pulsed fields, with tilting angles. DNA of more than 60 kbp could be separated within 15 s, but without baseline separated resolution. Two disadvantages were, that only linear DNA molecules could be separated and the diffusion limited resolution. In 2004, Huang et al. presented a device that did not rely on linear molecules and enabled continuous-flow separation of long DNA molecules and nanobeads [203]. The separation mechanisms either were based on the asymmetric bifurcation of laminar flow around obstacles driven by hydrodynamic flow (for beads) or on the bifurcation of electric fields the same way (for DNA). Dependent on the particle size different paths were followed. 0.8 μm to 1.0 μm beads could be separated within 40 seconds without baseline separated resolution. Whereas separation of large DNA (61 kbp and 158 kbp) took 10 min.

The continuous-flow separation presented in this thesis exhibited several advantages: fast separation time, less than 1 min; accessibility to linear as well as circular DNA; separation of very small DNA fragments down to 3-80 bp; baseline separated resolution, for binary as well as multiple-separation; on-line adaptability of selectivity parameters *via* applied voltages. Thus, it combined the advantages of the three continuously operating microfluidic devices, published in [13, 202, 203], in one single device.

4.5.2 Continuous-flow detection of DNA-complexes

Beyond successful preparative separation of DNA species of different sizes, the system proved to be sensitive enough to distinguish between pure DNA and DNA-complexes. Hence, complex-formation was detected in continuous-flow processing mode.

Four different DNA-complexes were investigated. Thereof three were with the intercalating cancer drug Actinomycin D (ACTD), at variable drug concentrations. The fourth complex was with *Escherichia coli* RNA polymerase core enzyme (RNAP).

DNA/Actinomycin D complexes The first complex that was investigated was a drug-DNA complex, with a ratio of 1 ACTD per 5 DNA base pairs (see figure 4.22 a). At ac-voltages of 650 Hz at 600 V two distinct molecules streams appeared downstream of the ridge. Identification of the two streams revealed that the DNA-complex was deflected at the ridge, whereas the pure DNA passed the ridge unhindered (see appendix figure 5.1 c) and d). The two peaks downstream of the ridge were baseline separated (figure 4.22) with resolution of $Res = 5.14$.

The novel technique for continuous-flow detection of complex formation was characterized regarding the sensitivity, i.e. the detectable ratio of bound drugs. Therefore, the ratio of ACTD was stepwise reduced. First, the ratio of ACTD per DNA base pairs was halved (ratio 1:10 ACTD per DNA bp). When the ac-voltages were adapted to 550 Hz at 650 V two distinct molecule streams were observed downstream of the ridge. Thus, complex formation was detected. Next, the ratio was reduced to a quarter of the starting ratio (1:20

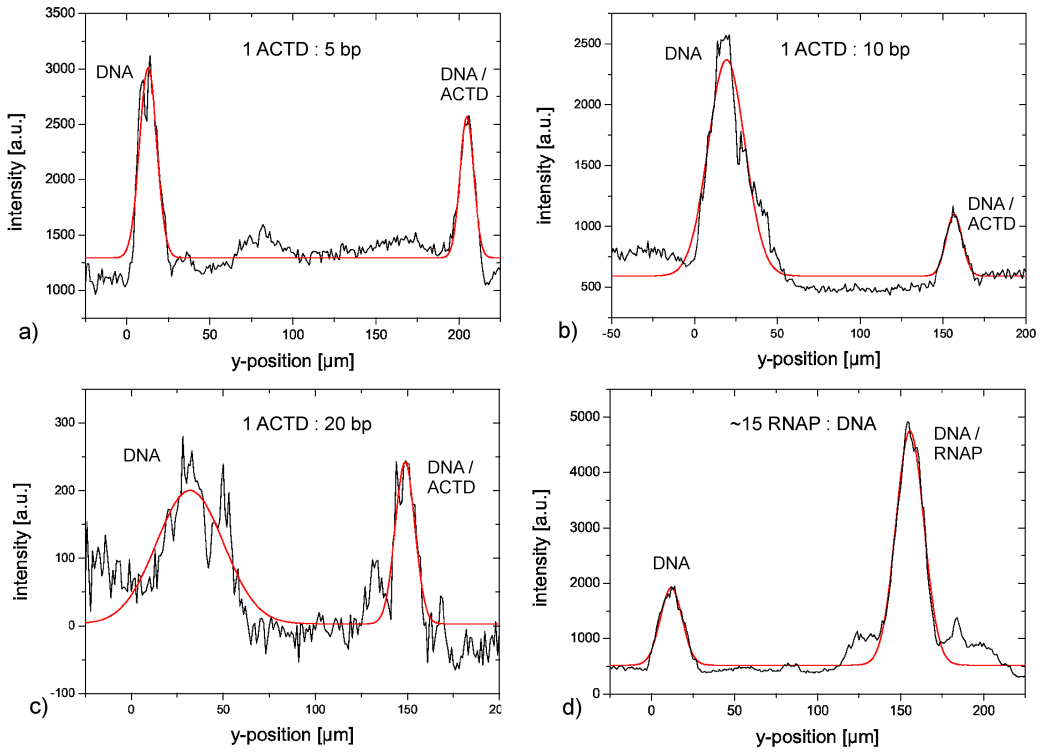

Figure 4.22: *Detection of complex formation. Fluorescence intensity plots downstream of the nanoslit (670 nm height) for separation of DNA and DNA-complexes (cf. figure 4.17). The black lines are the raw data and the red lines are Gaussian fits. a) DNA/ACTD-complex with 1 Actinomycin D per 5 DNA base pairs ($\omega = 650$ Hz at $U_{ac} = 600$ V, resolution Res $= 5.14$). b) DNA/ACTD-complex with 1 Actinomycin D per 10 DNA base pairs ($\omega = 550$ Hz at $U_{ac} = 650$ V, resolution Res $= 2.14$). c) DNA/ACTD-complex with 1 Actinomycin D per 20 DNA base pairs ($\omega = 500$ Hz at $U_{ac} = 600$ V, resolution Res $= 1.36$). d) Separation of 6.0 kbp DNA from 6.0 kbp DNA/RNAP-complex (resolution Res $= 2.4$; about 15 polymerase per DNA-molecule, ω=300 Hz at U_{ac}=650 V).*

ACTD per DNA bp). Again, the parameters were adapted (500 Hz at 600 V), and two distinct molecule streams were observed downstream of the ridge. Even for the reduced amount of ACTD to a ratio of 1ACTD per 20 base pairs, a baseline separated resolution of $Res = 1.36$ was achieved. This proved the very high sensitivity of the system to molecular recognition.

One critical point might be the low ionic strength of the buffer, as DNA-complexes might be destabilized. Here, two distinct streams were detected downstream, hence, a complex-formation was observed. Experiments with single species at the same conditions demonstrated, that the DNA-complexes were deflected. Thus, if the DNA-complex became instable and dissociated upstream of the ridge, the molecule would not be deflected. If the complex dissociated during migration along the ridge, the molecule would leave the ridge before the other channel wall was reached. This was observed only for a negligible amount of DNA-molecules.

For DNA-complexes with a substantial ionic component, like zinc-fingers [207–209], buffers with low ionic strength could stabilize the complex-formation [106]. Thus, this continuous-flow detection technique would be ideal for these types of DNA-complexes.

The binding constants of the DNA-complexes, used in this work, were quite large [210]. Hence, they were stable for several hours as was observed by EMSA (see section 4.5.5). Due to the fast response time of 1.25 min, even less stable complexes might be investigated by this non-invasive dielectrophoretic detection method.

DNA/RNA polymerase complexes The second type of complexes were 6.0 kbp DNA *E.coli* RNA polymerase core enzyme complexes (DNA/RNAP-complex). The mixture of the DNA/RNAP-complexes and pure DNA was injected as a narrow stream towards the ridge. At ac-voltages of 300 Hz at 650 V, the complexes were deflected, whereas the pure DNA passed the ridge unhindered. Evaluation of the fluorescence intensities revealed that the two streams were with baseline separated resolution of $Res = 2.4$ (see figure 4.22 d).

Noticeable shoulders to the left and the right of the DNA-complex-peak were observed. AFM images were used to investigate the distribution of RNAP along the DNA strand. In figure 4.23 a topography image of the DNA/RNAP-complex solution beforehand on-chip separation is depicted. The white dots were *Escherichia coli* RNA core polymerase and the white lines were the linear DNA strands. An inhomogeneous distribution of polymerase along the DNA strand was visible, giving a hint for the observed shoulders. Rivetti et al. found some DNA strands with more than one polymerase and some DNA strands with no polymerase, either [211].

Some methods to detect and investigate DNA-complexes were found in literature like electrophoretic mobility shift assays (EMSA) [104, 105, 107, 108, 212], surface plasmon resonance (SPR) [213–215], DNA- or protein-microarrays [216–225]. The most prominent was based on gel electrophoresis with electrophoretic mobility shift assays. Thus, in the present work EMSA investigations were performed and discussed later on (see section 4.5.5). Generally, surface plasmon resonance was used for real-time recording of association and dis-

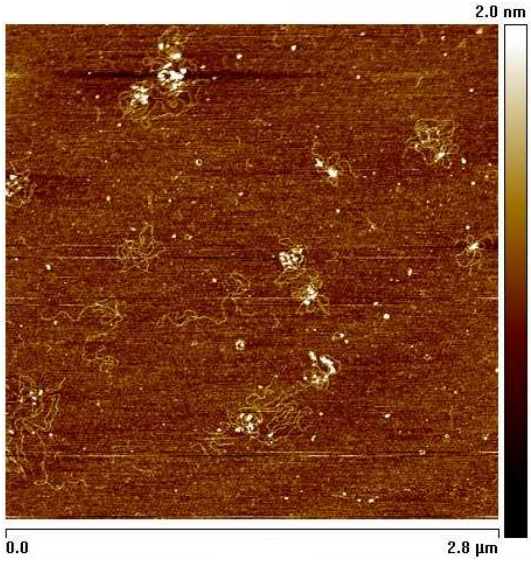

Figure 4.23: *AFM image (topography) of 6 kbp DNA/RNAP-complex solution before performance of separation. The proteins (bright spots on DNA strands) were not homogeneously distributed along the DNA strand (cf. also [211])*

sociation of proteins and their anticipated binding partner. Its disadvantage was, that no high-throughput was achieved. DNA- and protein-microarrays on the contrary allowed high-throughput detection of binding sites and semi-quantitative analysis. Beneath the sophisticated production of the microarrays, the DNA-microarrays lacked in easy analysis processes for individual proteins. For protein-microarrays, the monomer-specificity of the assay and the general requirements to the environments of different proteins were very complex.

In this thesis, a new continuous-flow detection method was developed that is competitive to the established techniques, as it allowed high throughput, real-time responses within less than 1 min with a simple and cost-saving device.

4.5.3 Dielectrophoretic mobility shift assays (DEMSA)

The dielectrophoretic potential is proportional to the analytes´ polarizability (see section 2.3.4), i.e. if two analytes, that differ in polarizability, were driven through a dielectrophoretic potential landscape, the mean velocities will differ. This effect was exploited for the novel technique of dielectrophoretic mobility shift assay.

Therefore, the microfluidic channel was structured with several insulating ridges that were oriented perpendicular to the long channel axis. Superimposed ac- and dc-voltages generated a dielectrophoretic landscape and drove the DNA-molecules. As for the continuous-

flow separation, the dielectrophoretic trapping and the electrophoretic migration could be controlled separately (equation (4.3)). Pinched injection protocol was used to inject a defined amount of molecules towards the ridges. For appropriate voltages, one sort of molecules was temporarily trapped and retarded. Thus, the migration velocity was reduced.

Experimentally, fluorescence images were taken of subsequently driven species. The fluorescence intensity was evaluated in a defined region, between two ridges, for each sort of molecule, separately. Afterwards, the fluorescence intensity was plotted versus time for each species to detect a shift between the investigated species.

6.0 kbp and 2.686 kbp DNA were investigated as a proof-of-principle. In figure 4.24 a) the fluorescence intensities are depicted. A clear shift could be observed, i.e. the 6.0 kbp DNA was clearly retarded, with respect to the 2.686 kbp DNA. To prove the applicability of dielectrophoretic mobility shift assays for detection of DNA-complex-formation, ACTD/DNA- and RNAP/DNA-complexes were investigated. The fluorescence intensity plots are depicted in figure 4.24 b) and c). It stands out, that for both complexes, ACTD/DNA and RNAP/DNA, the pure DNA appeared earlier at the detection region. Thus, the DNA-complexes had a longer trapping time. Respectively, the polarizability of the complexes was larger than for the pure DNA. That was verified by polarization experiments (see section 4.5.4).

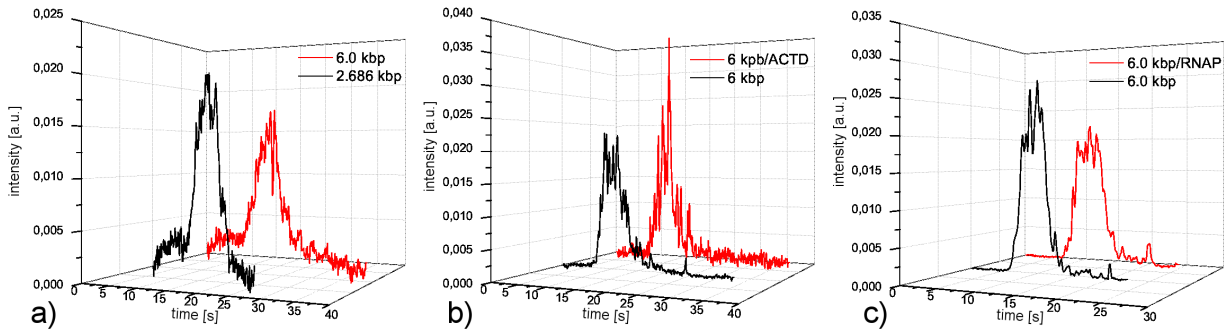

Figure 4.24: *Dielectrophoretic mobility shift assays. For all assays a clear shift was observed within less than 30 s, indicating a complex formation for DNA with Actinomycin D (ACTD) or E.coli RNA polymerase core enzyme (RNAP), respectively. a) 6.0 kbp and 2.686 kbp DNA at 350 Hz, 325 V ac-voltage. The 6.0 kbp DNA migrated more slowly than the 2.686 kbp DNA (peaks maxima at 13.2 s and 11.2 s, respectively). b) 6.0 kbp and 6.0 kbp DNA/ACTD complex, at 550 Hz, 350 V ac-voltage. The complex migrated more slowly than the pure DNA (peaks maxima at 10.4 s and 9.6 s, respectively). c) 6.0 kbp and 6.0 kbp DNA/RNAP complex at 300 Hz, 474 V ac-voltage. Again, the complex migrated more slowly (peaks maxima at 10.6 s and 9.4 s, respectively).*

The advantage of the DEMSA was the very fast detection time of less than 30 s. Even when taken into account the off-line postprocessing time for plotting the fluorescence intensity

this technique was very fast. To fasten up the detection, an on-line fluorescence evaluation could be used. In this thesis, two species of DNA variants were driven subsequently. But investigation of more than two species would be possible easily. Therefore, either the species could be driven subsequently, which might become time-consuming for a high variety of DNA species, or several channels might be driven in parallel with automated fluorescence monitoring. Additionally, the total process, from pipetting to fluorescence readout could be automized, enabling time-series to determine binding constants.

4.5.4 Determination of polarizability

One critical point in dielectrophoretic manipulation is the difficulty of obtaining quantitative values of polarizability of the analyte. Especially for biomolecules like DNA, the polarization effects are not fully understood and therefore prediction of the polarizability is challenging. Since the continuous-flow processing, presented in section 4.5.1 and section 4.5.2, allowed an on-line adaption and control of the parameters (voltages, frequencies), an *a priori* knowledge was not necessary. The selectivity parameters of DEMSA (ac-voltage and frequency) were easily adaptable after each run. Thus, an *a priory* knowledge was not necessary, either. Nevertheless, the polarizability was an interesting metric for the electrical properties of the bulk material or the surrounding ion cloud. Determination of the polarizability allowed a better understanding of the separation mechanism in more detail.

As was described in section 3.5.2, an array of perpendicular arranged ridges (see figure 3.12) was used to determine the polarizabilities. The molecules were injected *via* pinched injection protocol [178] and the migration time was evaluated for various ac-voltages. With equation (3.1) the experimental values were fitted (see figure 4.25) and the polarizabilities calculated. The resulting polarizabilities are summarized in table 2.

The obtained values agreed with the previous results of the separation experiments. DNA with larger polarizability was deflected (continuous-flow separation) or retarded (DEMSA), whereas DNA of lower polarizability passed the ridge unhindered (continuous-flow separation) or was less retarded (DEMSA), respectively. Note, that the polarizability depended on the frequency as well as on the viscosity of the buffer as was mentioned by Chou et al. [155].

Values of polarizability also depended on the technique as presented in literature: Stellwagen et al. found $5.5 \cdot 10^{-31} Fm^2$ for 4.4 kbp DNA fragments using transient electric birefringence (TEB) in Tris buffer (0.2 mM, pH 8) [226]; Elias and Eden found $2.3 \cdot 10^{-30} Fm^2$ for 5 kbp DNA fragments using TEB in sodium phosphate (1 mM Na, pH 7.2) [206]; Hanss and Bernengo found $3.2 \cdot 10^{-28} Fm^2$ for 8 kbp DNA fragments using conductivity dispersion in 1 mM NaCl [227]; Tuukkanen using dielectrophoretic trapping in a microelectrode array (assuming the potential barrier to be equal to the thermal energy under conditions for which the DNA just started to escape) found $6 \cdot 10^{-31} Fm^2$ for 8 kbp DNA fragments in 3 mM Hepes, 2 mM NaOH, pH 6.9 [157]. Thus, the polarizabilities determined in this thesis

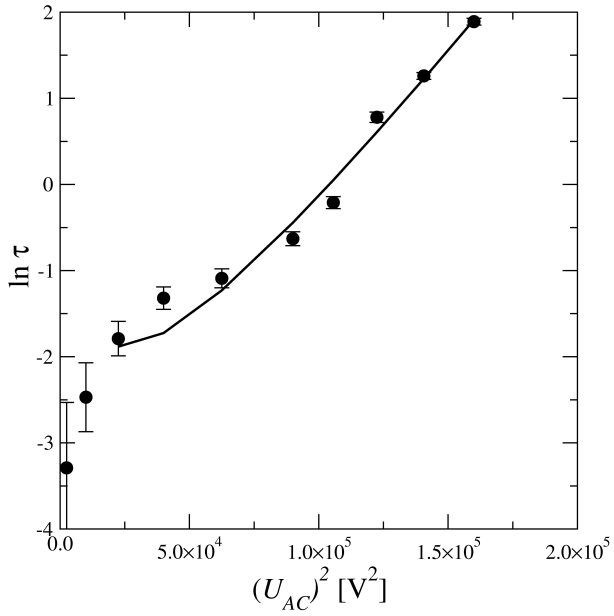

Figure 4.25: *Plot of mean lifetime versus applied U_{ac}^2, with fit exploiting equation (3.1) for determination of polarizability of 6.0 kbp DNA ($U_{dc} = 20$ V and $\omega = 350$ Hz).*

agreed very well with the published data. For protein-DNA or drug-DNA complexes, to the author's best knowledge, no values have been published, so far.

The results for the DNA-complexes confirmed a change of the polarizability due to complex-formation. This might have two reasons: 1) the ion cloud that surrounded the molecule could be changed due to the charge of the complexed molecules; 2) the radius of gyration could be changed by intercalation or alignment of ACTD or RNAP to DNA [81, 98, 228, 229]. To check the influence of complex-formation to the radius of gyration, diffusion experiments were performed.

The hydrodynamic radius was determined by equation (2.20). Therefore, the mean square area $< R^2 >$ was plotted versus time t (figure 4.26) and $D = \frac{<R^2>}{4t}$ was used to calculate the diffusion coefficient. The results are summarized in figure 4.26. The diffusion constants, and thus the molecules radii, differed only slightly within the experimental error for the 6.0 kbp DNA and DNA-complexes. In contrast, between 6.0 kbp and 2.686 kbp a significant difference was observed. Based on these results, it was more probable that the change of polarizability was affected by the ion cloud.

4.5.5 Electrophoretic mobility shift assay (EMSA)

Two new techniques for separation and detection of topological DNA-variants and DNA-complexes have been presented. When a new technique is introduced, a comparison with

Table 2: Polarizabilities of DNA and DNA-complexes at given frequencies. [a] 0.022% glycerin was added to the solution, in order to obtain the same viscosity as for the 6.0 kbp DNA/RNAP-complex.

probe	$\omega[Hz]$	$\alpha[10^{-30}Fm^2]$
2.686 kbp DNA	350	2.55 ± 0.38
6.0 kbp DNA	350	4.30± 0.37
6.0 kbp DNA	550	2.68± 0.28
6.0 kbp DNA/ACTD-complex	550	3.48± 0.10
6.0 kbp DNA[a]	300	1.41± 0.46
6.0 kbp DNA/RNAP-complex	300	1.95± 0.39

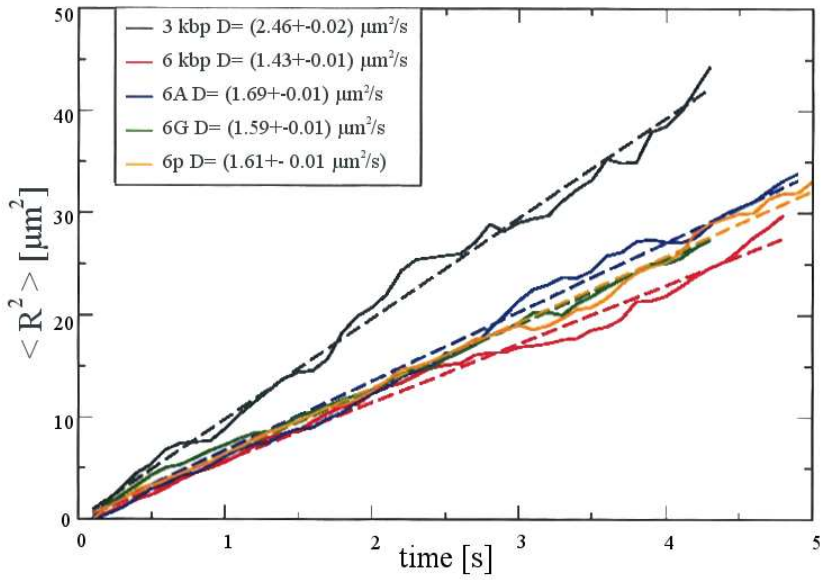

Figure 4.26: *Mean area versus time to determine the diffusion coefficient D. Abbreviations: 3 kbp stands for 2.686 kbp DNA, 6A is ACTD/DNA-complex, 6G stands for diffusion experiment of 6.0 kbp DNA with additional glycerin, 6p is RNAP/DNA-complex. No significant change of the diffusion coefficient was observed for 6.0 kbp DNA and DNA-complexes, but for 2.868 kbp DNA.*

an established method is required. The most established method for analytical separation of DNA and DNA-complexes is the electrophoretic mobility shift assay (EMSA). Thus,

with EMSA DNA binding studies were performed in this work. Therefore, typically two lanes in an agarose gel were used, one with pure DNA and the second with the DNA and its anticipated binding partner. If a shift was observed between these two bands, a complex-formation of the DNA and the binding partner was assumed [104].

Here, EMSA experiments were performed with the same analytes as for the on-chip experiments. First, the electrophoretic migration of 6.0 kbp and 2.686 kbp DNA was investigated, with and without YOYO-1 labeling (figure 4.27 A-D). The binding of YOYO-1 induced a shift with resolution of $Res = 0.22$ (figure 4.27 B and C). The shift between 6.0 kbp and 2.686 kbp DNA was of resolution $Res = 1.2$ (with YOYO-1 labeling) or $Res = 1.77$ (without YOYO-1 labeling). In additional experiments it was verified, that ACTD as well as RNAP bound to YOYO-1 labeled DNA (figure 4.27 E-J). Due to the high binding constants (YOYO-1: $K_A = 6 \cdot 10^8\ Mol^{-1}$, ACTD: $K_A = 10^6\ Mol^{-1}$, RNAP:$K_A = 1.16 \cdot 10^6\ Mol^{-1}$) the built complexes were stable. For the ACTD/DNA shift, a resolution of $Res = 0.29$ was achieved and for the RNAP/DNA shift a resolution of $Res = 0.46$. The runtime of the gel was 3 h.

Thus both new methods, continuous-flow detection of complexes and DEMSA, achieved a significant better performance, regarding the amount of analyte as well as time-to-response. The resolutions of the chip performances were competitive or even better than for the EMSA.

4.5.6 DNA mixing

Above dielectrophoretic continuous-flow separation of mixtures of topological DNA variants or DNA-complexes were described (see section 4.5.1 and section 4.5.2). The process *vice versa* (mixing of two species of DNA) was possible in the present device as well. Two species of DNA were injected towards the ridge from two separate reservoirs as distinct streams (see figure 3.11). For each stream, it was assured, by applying appropriate dc-voltages, that the molecules occupied no more than a quarter of the channel width.

In figure 4.28 the experimental results are depicted. The larger 6.0 kbp DNA was deflected at the ridge and left the ridge at the other channel wall into the 2.686 kbp DNA stream. To determine if the mixing was sufficient, it was exploited that the two species exhibited different fluorescence brightness, according to the molecules length, thus different amount of YOYO-1. Visual inspection revealed a presence of both species in the merged stream. As for the separation experiments, it was confirmed that the 2.686 kbp DNA passed the ridge unhindered, whereas the 6.0 kbp DNA migrated along the ridge and did not escape before reaching the 2.686 kbp DNA stream. A detailed analysis of the video data confirmed that both species were fully mixed and did not flow in parallel streams. This was due to the electrokinetic motion of the DNA and diffusional motion within the merged stream.

The fluorescence intensity distribution was determined from the video data as described in section 3.5. Upstream of the ridge two peaks were identified, corresponding to the narrow injected streams. Downstream of the ridge only one peak was observed, depicting the

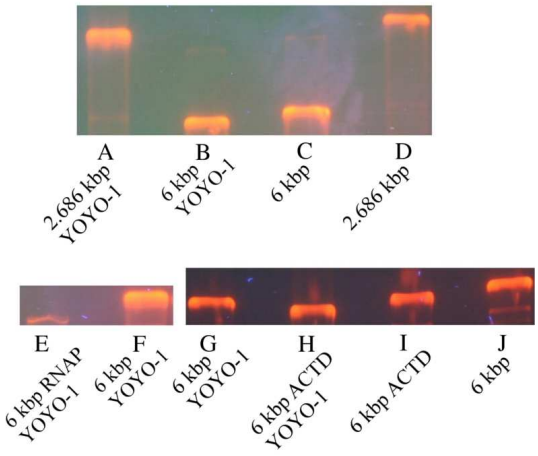

Figure 4.27: *Electrophoretic mobility shift assays. Three shift assays are shown (A-D), (E and F) and (G-J). A 2.686 kbp DNA labeled with YOYO-1. B 6.0 kbp DNA labeled with YOYO-1. C 6.0 kbp DNA. D 2.686 kbp DNA. E 6.0 kbp DNA with E.coli RNAP and YOYO-1. F 6.0 kbp DNA labeled with YOYO-1. G 6.0 kbp DNA labeled with YOYO-1. H 6.0 kbp DNA with ACTD and YOYO-1. I 6.0 kbp DNA with ACTD. J 6.0 kbp DNA. The resolution between A and B was* $Res = 1.2$*. The resolution between C and D was* $Res = 1.77$*. The resolution between E and F, polymerase induced shift, was* $Res = 0.46$*. The resolution between G and H, ACTD induced shift, was* $Res = 0.29$*. The resolution between B and C, indicating the YOYO-1 induced shift, was* $Res = 0.22$*, thus was smaller than the other shifts.*

mixed molecules stream. The throughput of the mixing process was determined to 2.5 nl/min for a mixing efficiency of about 100%. Comparing the results of DNA mixing and DNA separation it was found, that the processes were completely reversible. That means, the processes were only varied by the analytes injection, the applied voltages were all the same. As a consequence, the throughput was identical for separation and mixing.

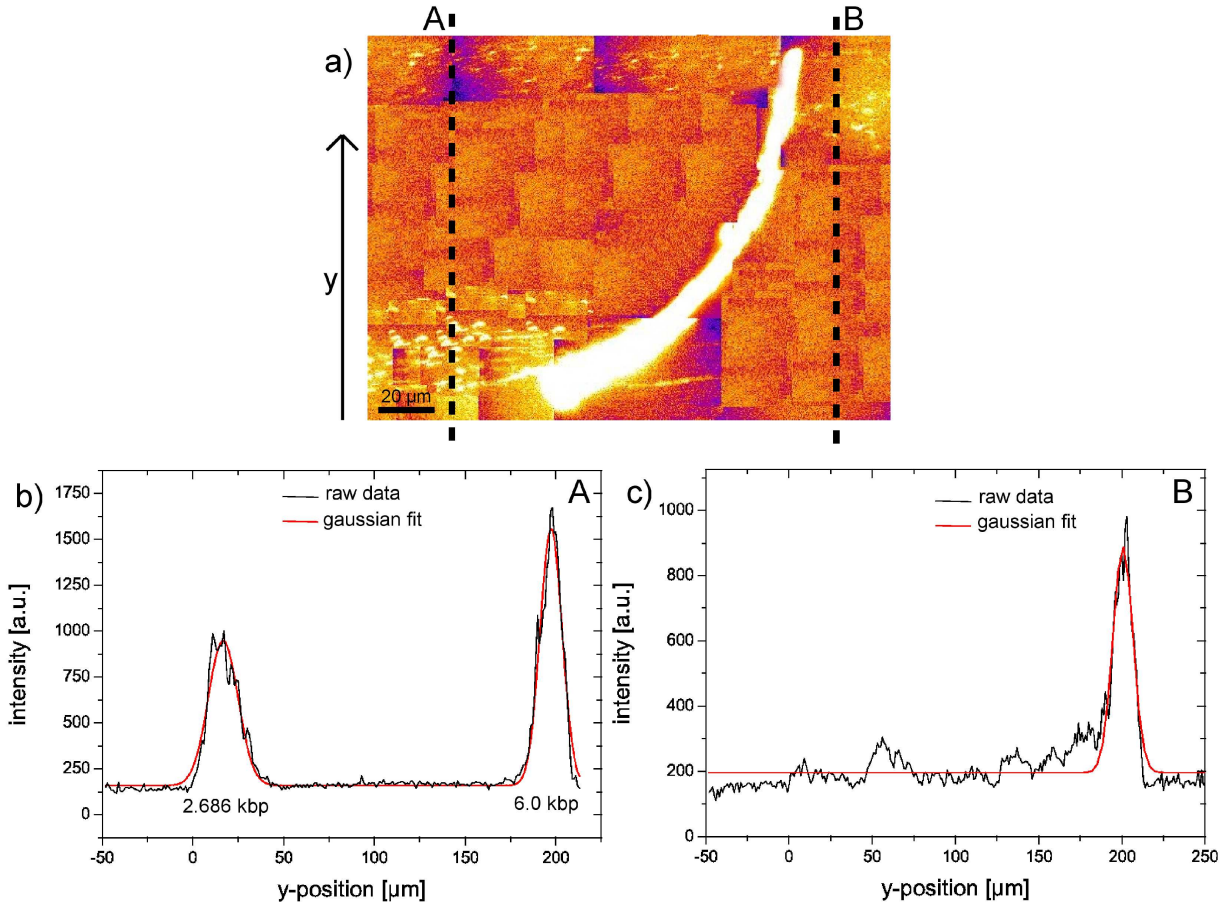

Figure 4.28: *Continuous-flow mixing of DNA molecules. a) Collage of fluorescence microscope images recorded during the experiments. The fluorescence intensities were analyzed along the dotted lines up- and downstream of the ridge (see section 3.5) to determine DNA molecules distributions. The results obtained from upstream of the ridge are depicted in b), the results downstream of the ridge in c). Black lines represent the measured distributions, red lines are Gaussian fits. For mixing two streams consisting of 6.0 kbp or 2.686 kbp DNA, respectively, flew towards the ridge. The throughput was 2.5 nl/min. The applied voltages during the mixing of 6.0 kbp and 2.686 kbp DNA were: -3 V at electrode 1, -10 V at electrode 3, and 2 V at electrode 4. Electrode 2 was grounded.*

4.5.7 Summary: DNA manipulation and separation by dielectrophoresis

Summarizing the DNA experiments, continuous-flow processes as well as batch processes with DNA, exploiting dielectrophoresis at nanoslits were presented. More precisely, novel techniques for continuous-flow detection, separation, and mixing of DNA-complexes and topological DNA variants were introduced. All exploited dielectrophoresis at a bowed ridge structure. Additionally, fast detection of DNA-complexes was performed at arrays of nanoslits introducing the new technique dielectrophoretic mobility shift assay (DEMSA). The investigated species were characterized due to their polarizability.

Generally, continuous-flow separation and mixing of DNA, were two complementary tasks that required different methodologies. Here, a realization of both tasks in one and the same device was presented. Thus, the processes had to be reversible, i.e. reversing the separation procedure resulted in mixing of the analyte and *vice versa*. Up to now the microfluidic realizations of mixing *via* dielectrophoresis presented in literature used Brownian motion, thus were not reversible. In the devices presented in this thesis, the mixing was reversible as two streams were merged, mainly without the need of Brownian motion. The mode of operation, either separation or mixing, was selected by how the analytes were injected towards the ridge. Therefore, the applied ac- and dc-voltages were tuned accordingly.

The throughput of separation and mixing of DNA was all the same (2.5 nl/min), as in both cases the total deflection of the larger molecule (here, 6.0 kbp DNA) was the limiting factor, i.e. if the electrophoretic energy/velocity was too high, the DNA was not trapped/deflected any more. Thus, no separation as well as mixing was possible in that case. Although not shown in this work, mixing of two analytes, e.g. beads with target DNA and corresponding DNA strands, can be followed by an additional separation to detect if complex formation appeared (see also Outlook).

Two new techniques to detect protein- or drug-DNA-complexes were presented with continuous-flow separation/detection and DEMSA. Both have their specific advantages. The most prominent advantages of the continuous-flow detection are the applicability for downstream applications, the on-line adaptability of the selection parameters *via* ac- and dc-voltages, and the fast detection time of less than 1 minute. Whereas the most prominent advantages of the DEMSA are the very fast response time of less than 30 s, the fast adaptability of sensitivity criterion *via* ac-voltages and the possibility to automate the processing. Hence, the best technique can be chosen depending on the task. For example, if the separated DNA-complex should be further investigated, the continuous-flow processing would be the right choice. On the other hand, if several DNA-complexes should be investigated regarding the complex-formation, the DEMSA was the right choice, since several analytes could be driven subsequently through the array and analyzed automatically.

When introducing new techniques, a comparison to well established techniques is required. In this thesis, electrophoretic mobility shift assays (EMSA) were used to yield reference. Therefore, the analytes were filled into two separate wells of an agarose gel. After 3 h, significant shifts between the pure DNA and the DNA-complex were observed. In contrast

to the EMSA experiments, for the continuous-flow detection as well as for the DEMSA the results were achieved within few minutes. Hence, the time-to-response was fastened up by a factor of about 150, without loss of sensitivity.

All three presented techniques (separation, binding-detection and mixing), were based on dielectrophoresis. The polarizability of the analyte was the inherent selectivity parameter. Hence, the polarizabilities were determined. The results of the polarizability experiments confirmed the previous observations, since the DNA with higher polarizability was deflected in separation or mixing procedures or more retarded than less polarizable DNA in DEMSA experiments. These findings agreed with equation (2.17) as for higher polarizabilities the dielectrophoretic potential increased, resulting in longer trapping times. In the DEMSA experiments the higher trapping times affected retarded migration velocities. Whereas for the continuous-flow processing, the dielectrophoretic trapping time was longer than the time for migration along the ridge, if a full deflection was achieved.

5 Summary and Outlook

In this thesis, a new monolithic production of nanochannels was presented that allowed development of new kinds of 3-dimensional structured nano-microfluidic devices. With these devices novel, sophisticated applications for functional micro total analysis systems (μTAS) were realized for the first time:

- continuous-flow electrostatic sieving of nanobeads and proteins
- continuous-flow mixing by dielectrophoresis (DEP)
- binary and multiple continuous-flow separation of nanobeads (DEP)
- binary and multiple continuous-flow separation of DNA (DEP)
- continuous-flow detection of DNA-complexes (DEP)
- dielectrophoretic mobility shift assays for detection of DNA-complexes
- determination of polarizability

The nano-microfluidic devices were produced monolithically with poly(dimethylsiloxane). The production and characterization was described in section 4.1. The channels were characterized according to size, stability, and reproducibility of production. For the first time, PDMS nanochannels with height down to 180 nm and width-to-height aspect ratio up to 873:1 were produced reproducible. These were considerable improvements compared to previously published aspect ratios for soft lithography with PDMS. Mao et al. reported maximal aspect ratios of 60:1 for using PDMS and 250:1 for the use of glass-silicone structures [184, 185]. Thus, the achieved ratio of 873:1, presented here, was 14.5 times better for PDMS and 3.5 times better for the use of glass-silicone.

These devices were used to implement new tools for μTAS. Therefore, some parameters were adjusted for control of the processing performance concerning the device layout, the applied electric voltages, and the buffer. The first method that was developed was the continuous-flow electrostatic sieving (see section 4.2). The continuous-flow electrostatic sieving concept was developed for separation of nanobeads and access to small biomolecules like proteins. For the first time a successful continuous-flow electrostatic sieving could be demonstrated by separation of 20 nm and 40 nm beads and manipulation of proteins.

The next methods were based on continuous-flow dielectrophoresis at the nanochannel. Beforehand to the experimental performance, the parameters that would influence the performance were considered (see section 4.3). The respective parameters were dc- and ac-voltages, frequency of electric field, height of the nanochannel, and shape of the ridge as well as the channel dimensions. Simulations of continuous-flow mixing and separation were performed concerning these parameters. Comparison with the experimental results

revealed that the simulations fit well, nearly quantitatively. Thus, a prediction of the sensitivity of the system was possible.

For the first time continuous-flow mixing and separation by dielectrophoresis could be preformed in one single device (see section 4.4). That became possible since the mixing process was not based on diffusion but on directed merging of two analyte streams. To change between mixing and separation only the injection of the analytes (100 nm and 20 nm beads) were adapted. The mixing efficiency was controlled during the experiment by visual inspection of the merged particles‘ stream. This revealed that both species were fully mixed and did not flow in parallel. Beyond the realization of two contrary processes in one single device, this was the first example of continuous-flow mixing by electrodeless dielectrophoresis. For the case *vice versa*, continuous-flow separation of 20 nm and 100 nm beads, a separation efficiency of 90-100% was achieved with baseline separated resolution. A throughput up to 7.5 nl/min was determined. Since the separation process started the moment the analytes reached the nanoslit no separation time existed, but for classification, the time until the first results was given with about 1 min.

Additional to binary separation, i.e. separation of two species, multiple-separation of three species was performed. Thus, a mixture of three species was continuously separated into three distinct particle streams that could be collected in separate outlets. A successful separation of three species (100 nm, 60 nm and 20 nm) was achieved.

Turning to biomolecules the novel dielectrophoresis based method allowed non-invasive investigation and preparation of DNA. Preparative separation and mixing of two DNA species was performed in one and the same device (see section 4.5.1 and section 4.5.6). For mixing very high efficiency was achieved, since all DNA molecules were merged into one single stream. Concerning continuous-flow separation of two species of linear or circular DNA, baseline separated resolutions were achieved within separation times of about 1 min. For performances, separation and mixing, the throughput was up to 2.5 nl/min for one single device.

With an improved device, three species of medically relevant DNA were completely separated without the need of matrices. Thus, the novel device allowed for the first time continuous-flow separation of three DNA species with electrodeless dielectrophoresis. Applications might be in production of *minicircle* DNA for gene vaccination. Since the novel techniques do not rely on classical filtration steps, shear-force associated analyte deterioration is reduced to a minimum. Together with the fact that this approach is inherently independent of toxic or mutagenic reagents, this new method could be implemented in a much easier way concerning the rigorous concerns of safety regulation in drug administration [17, 179].

Apart of preparative separation, dielectrophoresis was used for analytical separation, i.e. matrix-free detection of DNA-complex-formation (see section 4.5.2 and section 4.5.3). Here, two process modes were distinguished, continuous-flow and batch processing. In continuous-flow mode, a mixture of pure DNA and DNA with its anticipated binding partner was injected towards a ridge. Complex-formation was observed if the stream was split

into two streams. As for all continuous-flow processes in this work, the selectivity criteria were adaptable on-line and the result could be observed in real-time.

With dielectrophoretic mobility shift assays (DEMSA) a second fast detection method for DNA-complexes was introduced (see section 4.5.3). The basic concept for the detection relied on dielectrophoretically retarded migration velocities. Therefore, the migration of pure DNA and DNA with its anticipated binding partners was monitored in an array of nanoslits. Within less than 30 s, a clear shift could be detected, that indicated a complex-formation.

Additional to the dielectrophoretic mixing and separation of DNA molecules, the polarizability was determined according to the previous experiments (see section 4.5.4). The results revealed that in each case the polarizability corresponded to the dielectrophoretic separation experiments. For instance, the polarizability was higher for the analytes that were (more strongly) affected by dielectrophoresis. Furthermore, the determined polarizabilities of pure DNA were in good agreement to the values in the literature. Whereas for DNA-complexes no values were found in the literature, so far. Hence, these were the very first devices that allowed a dielectrophoretic characterization of DNA-complexes

Since two new methods for detection of DNA-complexes were demonstrated, additional electrophoretic mobility shift assays (EMSA) were performed (see section 4.5.5) because EMSA was one of the established techniques to investigate DNA-complex formation [104, 106]. The comparison revealed that in contrast to the dielectrophoretic methods, the EMSA experiments needed much more analyte and were significantly slower with at least 3 h. Hence, the dielectrophoresis based methods were about 150 times faster than EMSA. In spite of that, the resolution of the DEP experiments was competitive.

The trajectories of the nanobeads were simulated, according to the binary dielectrophoretic separation. The simulations agreed very well to the experimental results. Thus, the minimal size difference for successful separation could be determined by simulations. The theoretical predications revealed that nanobeads that differed 30% in size could be distinguished in the current device. In future, this should be verified experimentally. Furthermore, simulations of the multiple-separation as well as the DNA experiments could yield a more precisely insight to the separation mechanism and sensitivity of the device. Based on simulations, the device layout could be further enhanced with respect of the throughput. Additionally, the minimal difference in polarizability of DNA-molecules for successful separation could be estimated.

With the novel techniques that were presented in this thesis, bioanalysis in microfluidic devices becomes possible on a new level. For example analyte-specific detections might be realized by a coupled mixing and separation process, in one and the same device e.g. to purify DNA solutions or detect specific antigens or antibodies [32, 36, 201]. Therefore, varying modified beads with specific target molecules would be mixed with the analyte stream consecutively, each from different reservoirs. After reaction, the analytes could be identified in an analytical separation downstream or purified.

The separation of DNA of various lengths and detection of DNA-complexes could be demonstrated sufficiently. In future, the separation of various conformations (linear, oc and ccc) will be addressed. Since in gene vaccination the ccc-conformation was preferred, that would have direct impact on the quality control mechanisms.

Appendix

Results of single DNA experiments

During the separation experiments two peaks were observed downstream of the nanoslit (see Results). To identify the species, experiments with single species were performed under identical conditions (see figure 5.1 for instance). As expected the larger 6.0 kbp DNA was deflected, whereas the smaller 2.686 kbp DNA was not affected. For detection of DNA-complexes the complex was deflected, whereas the pure DNA was not affected.

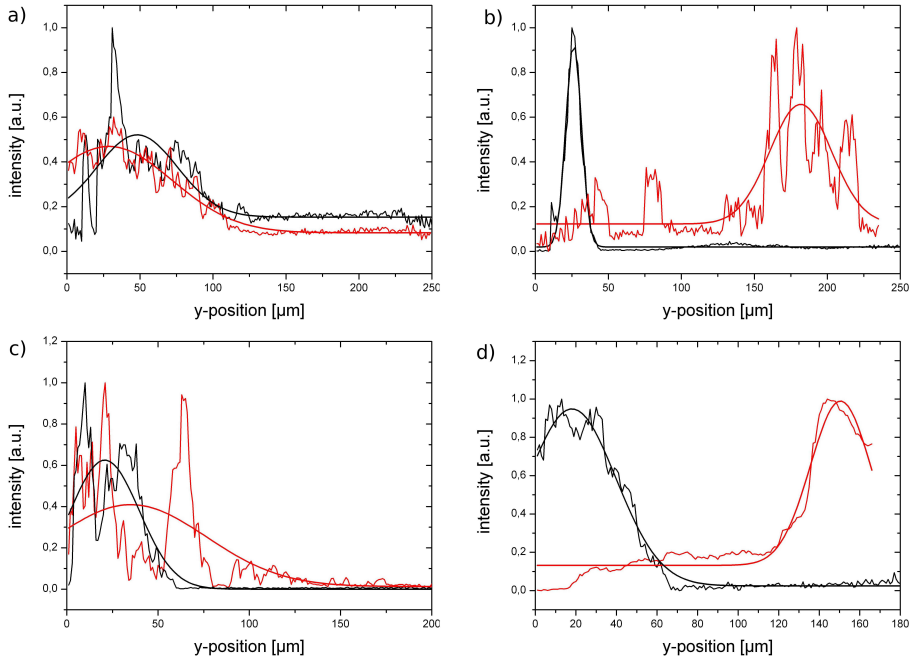

Figure 5.1: *Fluorescence intensities of the single experiments, i.e. one analyte was injected towards the ridge at identical parameters as for the successful separation experiments. a) The 2.686 kbp DNA passed the nanoslit unaffected. b) The 6.0 kbp DNA was fully deflected at the ridge. c) The pure DNA passed the nanoslit unaffected. d) The ACTD/DNA-complex was fully deflected at the ridge.*

In figure 5.2 the parental DNA was investigated beforehand incubation. All DNA molecules were deflected at the ridge. Thus, the cultivation system was not leaky [25]. Additionally, the deflected DNA of the separation experiment was identified to the parental DNA.

In figure 5.3 the dielectrophoretic response of the parental DNA and the miniplasmid were evaluated, according to the multiple-separation. The smaller miniplasmid DNA was only deflected at the first ridge and passed the second ridge unaffected. Whereas the parental plasmid was deflected at both ridges.

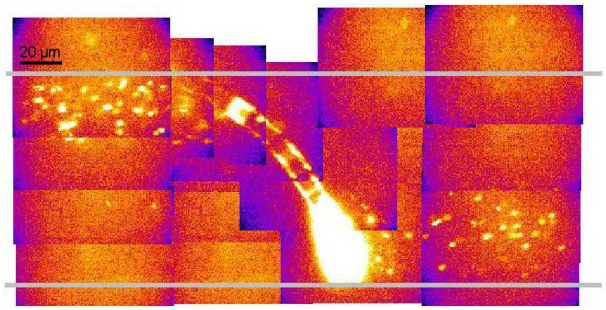

Figure 5.2: *Collage of fluorescence microscopy images of parental DNA beforehand induction. The parameters were identical to the separation of plasmid DNA and minicircle DNA in the device with 100 µm channel width and 180 nm nanoslit height. The DNA was totally deflected at the ridge.*

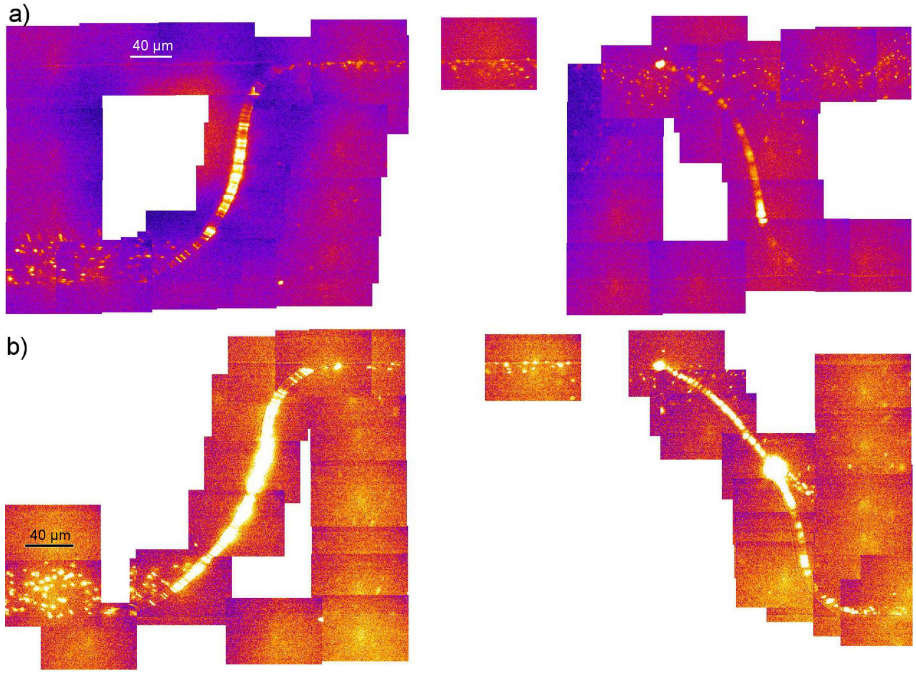

Figure 5.3: *Collage of fluorescence microscopy images of single species at identical conditions as for successful multiple-separation (channel width 200 µm height of nanoslits 500 nm). a) The miniplasmid DNA was deflected at the first ridge but passed the second ridge with reduced dielectrophoretic potential (see section 4.3) unhindered. b) The parental DNA was deflected at the first ridge as well as at the second ridge.*

AFM images of nanobeads

AFM-images of the polystyrene beads were taken to evaluate the size distribution. In figure 5.4 to figure 5.7 the AFM-images as well as the evaluated size distributions are depicted. Since the polarizability of the beads scales cubic with the radius of particles the size distribution affects the dielectrophoretic manipulation behavior significantly (*cf.* section 4.4.2).

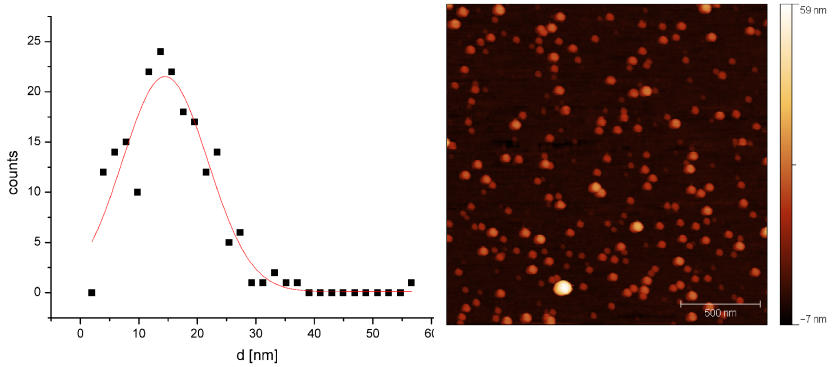

Figure 5.4: *AFM investigation of size distribution of the 20 nm beads. Left: particle size distribution. The particle sizes were determined automatically with the analyze tool of Gwyddion 2.19. Evaluation of 20 nm polystyrene beads with mean diameter of 14 nm ±7. Right: AFM image of nanobeads on mica.*

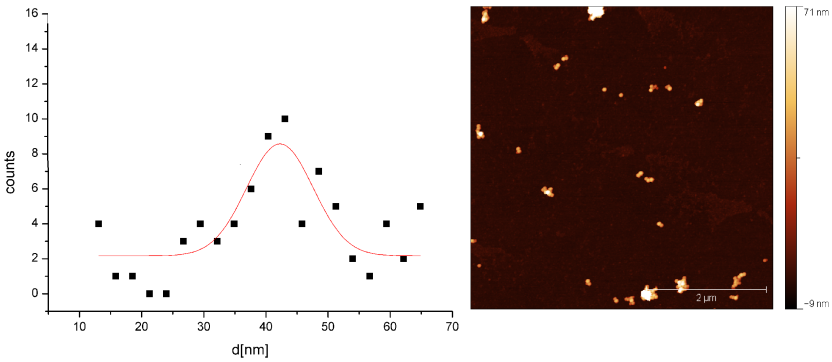

Figure 5.5: *AFM investigation of size distribution of the 40 nm beads. Left: particle size distribution. The particle sizes were determined automatically with the analyze tool of Gwyddion 2.19. Evaluation of 40 nm polystyrene beads with mean diameter of 42 nm ±5. Right: AFM image of nanobeads on mica.*

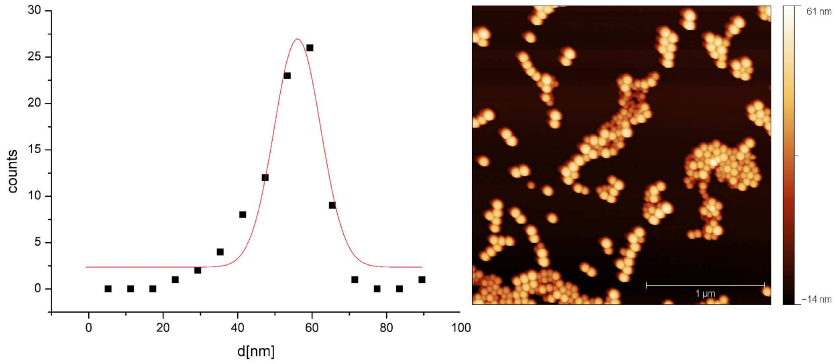

Figure 5.6: *AFM investigation of size distribution of the 60 nm beads. Left: particle size distribution. The particle sizes were determined automatically with the analyze tool of Gwyddion 2.19. Evaluation of 60 nm polystyrene beads with mean diameter of 56 nm ±6. Right: AFM image of nanobeads on mica.*

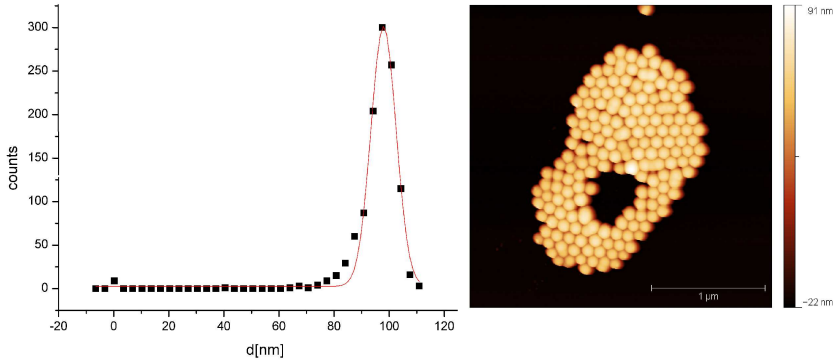

Figure 5.7: *AFM investigation of size distribution of the 100 nm beads. Left: particle size distribution. The particle sizes were determined automatically with the analyze tool of Gwyddion 2.19. Evaluation of 100 nm polystyrene beads with mean diameter of 98 nm ±5. Right: AFM image of nanobeads on mica.*

List of Publications

1. M. Everwand, D. Anselmetti, and R. Regtmeier. On-Chip continuous flow interaction studies of DNA and protein complexed DNA, Proceedings to 14th International Conference on Miniaturized Systems for Chemistry and Life Sciences (μTAS), October 3-7, 2010, Groningen, The Netherlands: 19-21, 2010.

2. J. Regtmeier, J. Käsewieter, M. Everwand, and D. Anselmetti. Continuous-flow Separation of Nanoparticles by Electrostatic Sieving at a Micro-nanofluidic interface, J. Separation Science, 34, Issue 10: 1180-1183, 2011.

3. J. Regtmeier, R. Eichhorn, M. Viefhues, L. Bogunovic, and D. Anselmetti. Electrodeless Dielectrophoresis for Bioanalysis: Theory, Devices and Applications, Electrophoresis, 32(17), 2253-2273 , 2011 (invited review).

4. M. Viefhues, S. Marchanda, T.-C. Chao, D. Anselmetti, J. Regtmeier, and A. Ros. Physisorbed Surface Coatings for Poly(dimethylsiloxane) and Quartz Microfluidic Devices, Analytical and Bioanalytical Chemistry, 401, 2113-2122, 2011.

5. M. Viefhues, R. Eichhorn, E. Fredrich, J. Regtmeier, and D. Anselmetti, Continuous and Reversible Mixing or Demixing of Nanoparticles by Dielectrophoresis, Lab Chip, 12, 485-494, 2012.

6. A. Rischmüller, M. Viefhues, M. Dieding, M. Schmeer, R. Baier, D. Anselmetti and M. Schleef, Analytical tools in minicircle production, in: Minicircle and Miniplasmids DNA vectors. The future of non-viral and viral gene transfer, Edited by M. Schleef, Wiley-VCH, Weinheim, ISBN: 3527324569, 2012.

7. M. Viefhues, J. Regtmeier and D. Anselmetti, Nanofluidic devices for dielectrophoretic mobility shift assays by soft lithography, J. Micromech. and Microeng., 22, 115024, 2012.

8. M. Viefhues, J. Regtmeier and D. Anselmetti, Fast and continuous-flow separation of DNA-complexes and topological DNA variants in microfluidic chip format, Analyst, 138 (1), 186 - 196, 2013.

9. M. Viefhues, S. Wegener, A. Rischmüller, M. Schleef and D. Anselmetti, Continuous-flow dielectrophoresis for multiple-separation of DNA, in preparation.

10. J. Regtmeier, S. Gerkens, M.Viefhues, L. Bogunovic and D. Anselmetti, Valveless pumping with one actuated membrane, in preparation.

Contributions to Conferences

1. M. Everwand, J. Regtmeier, and D. Anselmetti. Static and dynamic surface-coatings in quartz crystal- and Poly(dimethylsiloxane)-microfluidic channels, Spring Meeting of the German Physical Society, March 22-27, 2009, Dresden, Germany. (Talk)

2. M. Everwand, J. Käsewieter, D. Anselmetti, and J. Regtmeier. Hybrid Nano-Microfluidic channels with extrem aspect ratios, 13. Deutsche Physikerinnentagung, November 5-8, 2009, Frankfurt am Main, Germany. (Poster)

3. M. Everwand, A. Ros, D. Anselmetti, and J. Regtmeier. Surface coatings in Poly(dimethylsiloxane) and quartz microfluidic systems to control electroosmotic flow and protein adsorption, NanoBioTech Montreux, November 16-18,2009, Montreux, Switzerland. (Poster)

4. M. Everwand, D. Anselmetti, and J. Regtmeier. Dielectrophoresis: a new tool for continuous DNA/protein interaction studies, Spring Meeting of the German Physical Society, March 21-26, 2010, Regensburg, Germany. (Talk)

5. E. Fredrich, M. Everwand, J. Käsewieter, D. Anselmetti, and J. Regtmeier. Fabrication of hybrid nano-micro-fluidic channels with extreme aspect ratios, Spring Meeting of the German Physical Society, March 21-26, 2010, Regensburg, Germany.

6. M. Everwand, D. Anselmetti, and J. Regtmeier. Continuous separation of DNA protein complexes in a hybrid micro-nanofluidic device, 4th Lab-on-a-Chip European Congress, March 25-26,2010, Dublin, Ireland.

7. M. Everwand, D. Anselmetti, and J. Regtmeier. On-Chip continuous-flow interaction studies of DNA and protein complexed DNA, Fourteenth International Conference on Miniaturized Systems for Chemistry and Life Sciences (μTAS), October 3-7, 2010, Groningen, The Netherlands, 19-21, 2010. (Talk)

8. J. Regtmeier, M. Everwand, and D. Anselmetti. Continuous-flow separation and detection of DNA protein / DNA antibiotics complexes in a hybrid micro-nanofluidic device, Annual Meeting of the German Biophysical Society, October 3-6, 2010, Bochum, Germany.

9. J. Regtmeier, L. Bogunovic, M. Everwand, R. Eichhorn, and P. Reimann. New microfluidic tools for bioseparation, SFB 613 International Workshop, October 7+8, 2010, Bielefeld, Germany.

10. M. Everwand, D. Anselmetti, and J. Regtmeier. Switchable continuous-flow mixing and separation of DNA in microfluidic devices, 14. Deutsche Physikerinnentagung, November 4-7, 2010, Munich, Germany. (Poster)

11. M. Everwand, D. Anselmetti, and J. Regtmeier. Dielectrophoresis: a new tool for continuous DNA/ protein interaction analysis, NanoBioTech Montreux, November 15-17,2010, Montreux, Switzerland. (Poster)

12. M. Everwand, D. Anselmetti, and J. Regtmeier. On-chip realization of mixing and demixing nanoparticles using dielectrophoresis, Spring Meeting of the German Physical Society, March 13-18, 2011, Dresden, Germany. (Poster)

13. L. Bogunovic, M. Viefhues, D. Anselmetti, and J. Regtmeier. Microfluidic tools for DNA analysis, manipulation and separation, Statistical Mechanics and Computation of DNA self-assembly, May 25-28, 2011, Mariehamn, Finland.

14. M. Viefhues, L. Bogunovic, R. Eichhorn, M. Fliedner, J. Regtmeier, D. Anselmetti, and P. Reimann, New non-equilibrium migration mechanisms for microfluidic bioanalysis, SFB 613 Workshop, September 27+28, 2011, Loccum, Germany. (Talk and Poster)

15. M. Viefhues, E. Fredrich, R. Eichhorn, J. Regtmeier, and D. Anselmetti. Controlled mixing and demixing of nanoparticles by means of dielectrophoresis, NanoBioTech Montreux, November 13-16, 2011, Montreux, Switzerland. (Poster)

16. M. Viefhues, J. Regtmeier, and D. Anselmetti, Dielectrophoresis in lab-on-a-chip device: a new tool for continuous DNA/protein and DNA/antibiotic interaction analysis, SciTalk, November 23, 2011, Münster (Talk and poster)

17. S. Wegener, M. Viefhues and D.Anselmetti, Continuous-flow separation of nanoparticles by dielectrophoresis, DGfB, September 23, 2012, Göttingen

18. M. Viefhues, L. Bogunovic, S. Wegener, M. Fliedner, R. Eichhorn, J. Regtmeier, D. Anselmetti, and P. Reimann, New migration mechanisms and separation concepts for biomolecules in structured microfluidic systems, SFB 613 - International Workshop 2012, 27+28 September, 2012, Bielefeld, Germany (Poster)

Bibliography

[1] A. Manz, N. Graber, and H. M. Widmer. Miniaturized total chemical analysis systems: A novel concept for chemical sensing. *Sensors and Actuators B: Chemical*, 1(1-6):244–248, January 1990.

[2] W. Chen, R. H. W. Lam, and J. Fu. Photolithographic surface micromachining of polydimethylsiloxane (PDMS). *Lab Chip*, 12(2):391–395, Jan 2012.

[3] L. Chen, A. Manz, and P. J. R. Day. Total nucleic acid analysis integrated on microfluidic devices. *Lab Chip*, 7(11):1413–1423, Nov 2007.

[4] J. Khandurina and A. Guttman. Bioanalysis in microfluidic devices. *J Chromatogr A*, 943(2):159–183, Jan 2002.

[5] K.-I. Ohno, K. Tachikawa, and A. Manz. Microfluidics: applications for analytical purposes in chemistry and biochemistry. *Electrophoresis*, 29:4443–4453, 2008.

[6] S. K. Sia and G. M. Whitesides. Microfluidic devices fabricated in poly(dimethylsiloxane) for biological studies. *Electrophoresis*, 24:3563–3576, 2003.

[7] W. Sparreboom, A. van den Berg, and J. C. T. Eijkel. Principles and applications of nanofluidic transport. *Nat Nanotechnol*, 4(11):713–720, Nov 2009.

[8] T. M. Squires and S. R. Quake. Microfluidics: Fluid physics at the nanoliter scale. *Reviews of Modern Physics*, 77:977–1026, 2005.

[9] A. Arora, G. Simone, G. B. Salieb-Beugelaar, J. T. Kim, and A. Manz. Latest developments in micro total analysis systems. *Anal Chem*, 82(12):4830–4847, Jun 2010.

[10] P.-A. Auroux, D. Iossifidis, D. R. Reyes, and A. Manz. Micro total analysis systems. 2. analytical standard operations and applications. *Anal Chem*, 74(12):2637–2652, Jun 2002.

[11] X. Chen, D. F. Cui, and C. C. Liu. On-line cell lysis and DNA extraction on a microfluidic biochip fabricated by microelectromechanical system technology. *Electrophoresis*, 29(9):1844–1851, May 2008.

[12] P. S. Dittrich, K. Tachikawa, and A. Manz. Micro total analysis systems. Latest advancements and trends. *Anal Chem*, 78(12):3887–3908, Jun 2006.

[13] J. Fu, R. B. Schoch, A. L. Stevens, S. R. Tannenbaum, and J. Han. A patterned anisotropic nanofluidic sieving structure for continuous-flow separation of DNA and proteins. *Nat Nanotechnol*, 2(2):121–128, Feb 2007.

[14] D. R. Reyes, D. Iossifidis, P.-A. Auroux, and A. Manz. Micro total analysis systems. 1. Introduction, theory, and technology. *Anal Chem*, 74(12):2623–2636, Jun 2002.

[15] T. Vilkner, D. Janasek, and A. Manz. Micro total analysis systems. Recent developments. *Anal Chem*, 76(12):3373–3385, Jun 2004.

[16] J. West, M. Becker, S. Tombrink, and A. Manz. Micro total analysis systems: latest achievements. *Anal Chem*, 80(12):4403–4419, Jun 2008.

[17] M. Viefhues, J. Regtmeier, and D. Anselmetti. Nanofluidic devices for dielectrophoretic mobility shift assays by soft lithography. *Journal of Micromechanics and Microengineering*, 22(11):115024, 2012.

[18] P. Fanzio, V. Mussi, C. Manneschi, E. Angeli, G. Firpo, L. Repetto, and U. Valbusa. DNA detection with a polymeric nanochannel device. *Lab Chip*, Jul 2011.

[19] G. B. Salieb-Beugelaar, G. Simone, A. Arora, A. Philippi, and A. Manz. Latest developments in microfluidic cell biology and analysis systems. *Anal Chem*, 82(12):4848–4864, Jun 2010.

[20] G. M. Whitesides. The origins and the future of microfluidics. *Nature*, 442(7101):368–373, Jul 2006.

[21] S. Mandal, M. Moudgil, and S. K. Mandal. Rational drug design. *Eur J Pharmacol*, 625(1-3):90–100, Dec 2009.

[22] W. Jechlinger, C. A. Tabrizi, W. Lubitz, and P. Mayrhofer. Minicircle DNA immobilized in bacterial ghosts: in vivo production of safe non-viral DNA delivery vehicles. *J Mol Microbiol Biotechnol*, 8(4):222–231, 2004.

[23] P. Mayrhofer, M. Blaesen, M. Schleef, and W. Jechlinger. Minicircle-DNA production by site specific recombination and protein- DNA interaction chromatography. *The Journal of Gene Medicine*, 10(11):1253–1269, 2008.

[24] P. Mayrhofer, M. Schleef, and W. Jechlinger. Use of minicircle plasmids for gene therapy. *Methods Mol Biol*, 542:87–104, 2009.

[25] A. Rischmüller, M. Viefhues, M. Dieding, M. Schmeer, R. Baier, D. Anselmetti, and M. Schleef. *Minicircle and Miniplasmid DNA vectors. The future of non-viral and viral gene transfer*. Wiley-VCH, Weinheim, 2012.

[26] M. Yamada, V. Kasim, M. Nakashima, J. Edahiro, and M. Seki. Continuous cell partitioning using an aqueous two-phase flow system in microfluidic devices. *Biotechnol Bioeng*, 88(4):489–494, Nov 2004.

[27] M. Yamada and M. Seki. Hydrodynamic filtration for on-chip particle concentration and classification utilizing microfluidics. *Lab Chip*, 5(11):1233–1239, Nov 2005.

[28] S. Meinhardt, J. Smiatek, R. Eichhorn, and F. Schmid. Separation of chiral particles in micro- or nanofluidic channels. *Phys Rev Lett*, 108(21):214504, May 2012.

[29] J. Sun, M. Li, C. Liu, Y. Zhang, D. Liu, W. Liu, G. Hu, and X. Jiang. Double spiral microchannel for label-free tumor cell separation and enrichment. *Lab Chip*, 12(20):3952–3960, Sep 2012.

[30] G. D. Chen, F. Fachin, E. Colombini, B. L. Wardle, and M. Toner. Nanoporous micro-element arrays for particle interception in microfluidic cell separation. *Lab Chip*, 12(17):3159–3167, Sep 2012.

[31] S. M. McFaul, B. K. Lin, and H. Ma. Cell separation based on size and deformability using microfluidic funnel ratchets. *Lab Chip*, 12(13):2369–2376, Jul 2012.

[32] M. Karle, J. Miwa, G. Czilwik, V. Auwärter, G. Roth, R. Zengerle, and F. von Stetten. Continuous microfluidic DNA extraction using phase-transfer magnetophoresis. *Lab Chip*, 10(23):3284–3290, Dec 2010.

[33] N. Pamme. Magnetism and microfluidics. *Lab Chip*, 6(1):24–38, Jan 2006.

[34] A. Weddemann, C. Albon, A. Auge, F. Wittbracht, P. Hedwig, D. Akemeier, K. Rott, D. Meissner, P. Jutzi, and A. Hütten. How to design magneto-based total analysis systems for biomedical applications. *Biosens Bioelectron*, 26(4):1152–1163, Dec 2010.

[35] A. Hütten, D. Sudfeld, I. Ennen, G. Reiss, W. Hachmann, U. Heinzmann, K. Wojczykowski, P. Jutzi, W. Saikaly, and G. Thomas. New magnetic nanoparticles for biotechnology. *J Biotechnol*, 112(1-2):47–63, Aug 2004.

[36] M. Karle, J. Miwa, G. Roth, R. Zengerle, and F. von Stetten. A novel microfluidic platform for continuous DNA extraction and purification using laminar flow magnetophoresis. In *Micro Electro Mechanical Systems, 2009. MEMS 2009. IEEE 22nd International Conference on*, pages 276 –279, Jan 2009.

[37] Y. Baba. Capillary affinity gel electrophoresis. New tool for detection of the mutation on DNA. *Mol Biotechnol*, 6(2):143–153, Oct 1996.

[38] M. Kamahori and H. Kambara. Characteristics of single-stranded DNA separation by capillary gel electrophoresis. *Electrophoresis*, 17(9):1476–1484, Sep 1996.

[39] R. Kuhn and S. Hoffstetter-Kuhn. *Capillary Electrophoresis: Principles and Practice*. Springer Verlag, 1993.

[40] G. Slater and J. L. Viovy. Theory of electrophoresis. *Electrophoresis*, 17(6):A68–A71, Jun 1996.

[41] G. W. Slater, S. Guillouzic, M. G. Gauthier, J.-F. Mercier, M. Kenward, L. C. McCormick, and F. Tessier. Theory of DNA electrophoresis (approximately 1999-2002(1/2)). *Electrophoresis*, 23:3791–3816, 2002.

[42] N. C. Stellwagen, C. Gelfi, and P. G. Righetti. The free solution mobility of DNA. *Biopolymers*, 42:687–703, 1997.

[43] J. Regtmeier, R. Eichhorn, M. Viefhues, L. Bogunovic, and D. Anselmetti. Electrodeless dielectrophoresis for bioanalysis: Theory, devices and applications. *Electrophoresis*, 32(17):2253–2273, 2011.

[44] S. K. Srivastava, A. Gencoglu, and A. R. Minerick. DC insulator dielectrophoretic applications in microdevice technology: a review. *Anal Bioanal Chem*, 399(1):301–321, Jan 2011.

[45] R. Pethig, A. Menachery, S. Pells, and P. D. Sousa. Dielectrophoresis: a review of applications for stem cell research. *J Biomed Biotechnol*, 2010:182581, 2010.

[46] R. Hölzel. Dielectric and dielectrophoretic properties of DNA. *IET Nanobiotechnol*, 3(2):28–45, Jun 2009.

[47] B. H. Lapizco-Encinas and M. Rito-Palomares. Dielectrophoresis for the manipulation of nanobioparticles. *Electrophoresis*, 28(24):4521–4538, Dec 2007.

[48] J. Voldman. Electrical forces for microscale cell manipulation. *Annu Rev Biomed Eng*, 8:425–454, 2006.

[49] O. Bakajin, T. A. Duke, J. Tegenfeldt, C. F. Chou, S. S. Chan, R. H. Austin, and E. C. Cox. Separation of 100-kilobase DNA molecules in 10 seconds. *Anal. Chem.*, 73:6053–6056, 2001.

[50] J. Han and H. G. Craighead. Separation of long DNA molecules in a microfabricated entropic trap array. *Science*, 288:1026–1029, 2000.

[51] M. Streek, F. Schmid, T. T. Duong, and A. Ros. Mechanisms of DNA separation in entropic trap arrays: a Brownian dynamics simulation. *J Biotechnol*, 112(1-2):79–89, Aug 2004.

[52] T. Duong, G. Kim, R. Ros, M. Streek, F. Schmid, J. Brugger, D. Anselmetti, and A. Ros. Size-dependent free solution DNA electrophoresis in structured microfluidic systems. *Microelectronic Engineering*, 67-68:905–912, 2002.

[53] P. Tabeling. A brief introduction to slippage, droplets and mixing in microfluidic systems. *Lab Chip*, 9(17):2428–2436, Sep 2009.

[54] V. Hessel, H. Löwe, and F. Schönfeld. Micromixers a review on passive and active mixing principles. *Chem Eng Sci*, 60:2479–2501, 2005.

[55] N.-T. Nguyen and Z. Wu. Micromixers - a review. *J Micromech Microeng*, 15:R1–R16, 2005.

[56] M. Viefhues, R. Eichhorn, E. Fredrich, J. Regtmeier, and D. Anselmetti. Continuous and reversible mixing or demixing of nanoparticles by dielectrophoresis. *Lab Chip*, 12:485–494, 2012.

[57] J. Regtmeier, J. Käsewieter, M. Everwand, and D. Anselmetti. Continuous-flow separation of nanoparticles by electrostatic sieving at a micro-nanofluidic interface. *J Sep Sci*, 34(10):1180–1183, May 2011.

[58] C. Church, J. Zhu, J. Nieto, G. Keten, E. Ibarra, and X. Xuan. Continuous particle separation in a serpentine microchannel via negative and positive dielectrophoretic focusing. *Journal of Micromechanics and Microengineering*, 20(6):065011, 2010.

[59] A. Lenshof and T. Laurell. Continuous separation of cells and particles in microfluidic systems. *Chem Soc Rev*, 39(3):1203–1217, Mar 2010.

[60] N. Lewpiriyawong, C. Yang, and Y. C. Lam. Continuous sorting and separation of microparticles by size using ac dielectrophoresis in a PDMS microfluidic device with 3D conducting PDMS composite electrodes. *Electrophoresis*, 31(15):2622–2631, Aug 2010.

[61] B. Cetin, Y. Kang, Z. Wu, and D. Li. Continuous particle separation by size via ac-dielectrophoresis using a lab-on-a-chip device with 3-D electrodes. *Electrophoresis*, 30(5):766–772, Mar 2009.

[62] S. S. Kuntaegowdanahalli, A. A. S. Bhagat, G. Kumar, and I. Papautsky. Inertial microfluidics for continuous particle separation in spiral microchannels. *Lab Chip*, 9(20):2973–2980, Oct 2009.

[63] J. Shi, H. Huang, Z. Stratton, Y. Huang, and T. J. Huang. Continuous particle separation in a microfluidic channel via standing surface acoustic waves (SSAW). *Lab Chip*, 9(23):3354–3359, Dec 2009.

[64] N. Lewpiriyawong, C. Yang, and Y. C. Lam. Dielectrophoretic manipulation of particles in a modified microfluidic H filter with multi-insulating blocks. *Biomicrofluidics*, 2(3):34105, 2008.

[65] G. O. F. Parikesit, A. P. Markesteijn, O. M. Piciu, A. Bossche, J. Westerweel, I. T. Young, and Y. Garini. Size-dependent trajectories of DNA macromolecules due to insulative dielectrophoresis in submicrometer-deep fluidic channels. *Biomicrofluidics*, 2(2):24103, 2008.

[66] B. G. Hawkins, A. E. Smith, Y. A. Syed, and B. J. Kirby. Continuous-flow particle separation by 3D insulative dielectrophoresis using coherently shaped, dc-biased, ac electric fields. *Anal Chem*, 79(19):7291–7300, 2007.

[67] K. H. Kang, Y. Kang, X. Xuan, and D. Li. Continuous separation of microparticles by size with direct current-dielectrophoresis. *Electrophoresis*, 27(3):694–702, Feb 2006.

[68] L. M. Barrett, A. J. Skulan, A. K. Singh, E. B. Cummings, and G. J. Fiechtner. Dielectrophoretic manipulation of particles and cells using insulating ridges in faceted prism microchannels. *Anal Chem*, 77(21):6798–6804, Nov 2005.

[69] S. Choi and J.-K. Park. Microfluidic system for dielectrophoretic separation based on a trapezoidal electrode array. *Lab Chip*, 5(10):1161–1167, Oct 2005.

[70] E. B. Cummings. Streaming dielectrophoresis for continuous-flow microfluidic devices. *IEEE Eng Med Biol Mag*, 22(6):75–84, 2003.

[71] E. B. Cummings and A. K. Singh. Dielectrophoresis in microchips containing arrays of insulating posts: theoretical and experimental results. *Anal Chem*, 75(18):4724–4731, Sep 2003.

[72] H. A. Pohl and K. Kaler. Continuous dielectrophoretic separation of cell mixtures. *Cell Biophys*, 1(1):15–28, Mar 1979.

[73] M. Z. Bazant and T. M. Squires. Induced-charge electrokinetic phenomena: theory and microfluidic applications. *Phys Rev Lett*, 92(6):066101, Feb 2004.

[74] Y.-K. Lee, J. Deval, P. Tabeling, and C.-M. Hoagland. Chaotic mixing in electrokinetically and pressure driven micro flows. *Proc 14th IEEE workshop on MEMS*, pages 483–486, 2001.

[75] A. Salmanzadeh, H. Shafiee, R. V. Davalos, and M. A. Stremler. Microfluidic mixing using contactless dielectrophoresis. *Electrophoresis*, 32(18):2569–2578, Sep 2011.

[76] M. L. Y. Sin, Y. Shimabukuro, and P. K. Wong. Hybrid electrokinetics for separation, mixing, and concentration of colloidal particles. *Nanotechnology*, 20(16):165701, Apr 2009.

[77] R. Tornay, T. Braschler, N. Demierre, B. Steitz, A. Finka, H. Hofmann, J. A. Hubbell, and P. Renaud. Dielectrophoresis-based particle exchanger for the manipulation and surface functionalization of particles. *Lab Chip*, 8(2):267–273, Feb 2008.

[78] R. Tornay, T. Braschler, and P. Renaud. Wide channel dielectrophoresis-based particle exchanger with electrophoretic diffusion compensation. *Lab Chip*, 9(5):657–660, Mar 2009.

[79] L. Ying, S. S. White, A. Bruckbauer, L. Meadows, Y. E. Korchev, and D. Klenerman. Frequency and voltage dependence of the dielectrophoretic trapping of short lengths of DNA and dCTP in a nanopipette. *Biophys J*, 86(2):1018–1027, Feb 2004.

[80] N. A. Campbell and J. B. Reece. *Biologie*. Spektrum Akademischer Verlag, 2003.

[81] H. Chen, X. Liu, and D. J. Patel. DNA bending and unwinding associated with Actinomycin D antibiotics bound to partially overlapping sites on DNA. *J Mol Biol*, 258(3):457–479, May 1996.

[82] N. P. Pavletich and C. O. Pabo. Zinc finger-DNA recognition: crystal structure of a zif268-DNA complex at 2.1 a. *Science*, 252:809–817, May 1991.

[83] Homepage Plasmid Factory. *Minicircle - minimized DNA to achieve unsurpassed luciferase expression*, Dec 2012.

[84] J.-L. Viovy. Electrophoresis of DNA and other polyelectrolytes: Physical mechanisms. *Reviews of Modern Physics*, 72(3):813–872, 2000.

[85] M. Doi and S. Edwards. *The theory of polymer dynamics*. Clarendon Press, Oxford, 1986.

[86] Y. Lu, B. Weers, and N. C. Stellwagen. DNA persistence length revisited. *Biopolymers*, 61(4):261–275, 2001.

[87] E. Abbe. Beiträge zur Theorie des Mikroskops und der mikroskopischen Wahrnehmung: I. die Construction von Mikroskopen auf Grund der Theorie. *Arch. f. Mikroskop. Anat.*, 9(1):413–468, 1873.

[88] D. Meschede. *Gerthsen Physik*. Springer Verlag, 2002.

[89] A. Larsson, C. Carlsson, M. Jonsson, and B. Albinsson. Characterization of the binding of the fluorescent dyes YO and YOYO to DNA by polarized light spectroscopy. *Journal of the American Chemical Society*, 116(19):8459–8465, 1994.

[90] A. Larsson, C. Carlsson, and M. Jonsson. Characterization of the binding of YO to [poly(dA-dT)]2 and [poly(dG-dC)]2, and of the fluorescent properties of YO and YOYO complexed with the polynucleotides and double-stranded DNA. *Biopolymers*, 36(2):153–167, Aug 1995.

[91] A. Fürstenberg, M. D. Julliard, T. G. Deligeorgiev, N. I. Gadjev, A. A. Vasilev, and E. Vauthey. Ultrafast excited-state dynamics of DNA fluorescent intercalators: new insight into the fluorescence enhancement mechanism. *J Am Chem Soc*, 128(23):7661–7669, Jun 2006.

[92] A. Rahman and D. A. Isenberg. Systemic lupus erythematosus. *New England Journal of Medicine*, 358(9):929–939, 2008.

[93] M. F. Fromm and M. Gramatzki. *Pharmakotherapie*, volume 13. Springer Verlag, 2007.

[94] Homepage Sigma-Aldrich. *A1410 Sigma: Actinomycin D*, Dec 2012.

[95] F.-M. Chen, F. Sha, K.-H. Chin, and S.-H. Chou. Binding of Actinomycin D to single-stranded DNA of sequence motifs d(TGTCT(n)G) and d(TGT(n)GTCT). *Biophys J*, 84(1):432–439, Jan 2003.

[96] R. L. A. Furlan, L. M. Garrido, G. Brumati, G. P. Amarante-Mendes, R. A. Martins, M. C. R. Facciotti, and G. Padilla. A rapid and sensitive method for the screening of DNA intercalating antibiotics. *Biotechnology Letters*, 24:1807–1813, 2002.

[97] Homepage Biocyc. *E. coli RNA Polymerase core enzyme*, Apr 2009.

[98] T. P. Hunt and B. Magasanik. Transcription of glnA by purified Escherichia coli components: core RNA polymerase and the products of glnF, glnG, and glnL. *Proc Natl Acad Sci*, 82(24):8453–8457, Dec 1985.

[99] S. Bülow and G. Link. Sigma-like activity from mustard (sinapis alba l.) chloroplasts conferringDNA-binding and transcriptionspecifity to E. coli core RNA polymerase. *Plant Molecular Biology*, 10:349–357, 1988.

[100] M. Leibman and A. Hochschild. A sigma-core interaction of the RNA polymerase holoenzyme that enhances promoter escape. *EMBO J*, 26(6):1579–1590, Mar 2007.

[101] M. Fried and D. M. Crothers. Equilibria and kinetics of lac repressor-operator interactions by polyacrylamide gel electrophoresis. *Nucleic Acids Research*, 9(23):6505–6525, 1981.

[102] S. M. Beverley. Characterization of the 'unusual' mobility of large circular DNAs in pulsed field-gradient electrophoresis. *Nucleic Acids Res*, 16(3):925–939, Feb 1988.

[103] A. G. Ogston. The spaces in a uniform random suspension of fibres. *Trans. Faraday Soc.*, 54:1754–1757, 1958.

[104] L. M. Hellman and M. G. Fried. Electrophoretic mobility shift assay (EMSA) for detecting protein-nucleic acid interactions. *Nat Protoc*, 2(8):1849–1861, 2007.

[105] C. Desruisseaux, G. W. Slater, and T. B. Kist. Trapping electrophoresis and ratchets: a theoretical study for DNA-protein complexes. *Biophys J*, 75(3):1228–1236, Sep 1998.

[106] M. G. Fried. Measurement of protein-DNA interaction parameters by electrophoresis mobility shift assay. *Electrophoresis*, 10(5-6):366–376, 1989.

[107] M. M. Garner and A. Revzin. A gel electrophoresis method for quantifying the binding of proteins to specific DNA regions: application to components of the Escherichia coli lactose operon regulatory system. *Nucleic Acids Res*, 9(13):3047–3060, Jul 1981.

[108] G. A. Griess, H. Choi, A. Basu, J. W. Valvano, and P. Serwer. Cyclic capillary electrophoresis. *Electrophoresis*, 23(16):2610–2617, Aug 2002.

[109] J. D. Taylor, A. J. Ackroyd, and S. E. Halford. The gel shift assay for the analysis of DNA-protein interactions. *Methods Mol Biol*, 30:263–279, 1994.

[110] J. C. Giddings. *Unified separation science*. 1991.

[111] W. Sparreboom, A. van den Berg, and J. C. T. Eijkel. Transport in nanofluidic systems: a review of theory and applications. *New Journal of Physics*, 12(1):015004, 2010.

[112] J. C. T. Eijkel and A. v. d. Berg. Nanofluidics: what is it and what can we expect from it? *Microfluidics and Nanofluidics*, 1:249–267, 2005. 10.1007/s10404-004-0012-9.

[113] Demtröder. *Experimentalphysik 1, Mechanik und Wärme*. Springer, 2004.

[114] J. Berthier and P. Silberzan. *Microfluidics for Biotechnology*. Artech House, 2006.

[115] P. Grossmann and J. Colburn. *Capillary Electrophoresis- Theory and Practice*. Academic Press, 1992.

[116] R. Tadmor, E. Hernandez-Zapata, N. Chen, P. Pincus, and J. N. Israelachvili. Debye length and double-layer forces in polyelectrolyte solutions. *Macromolecules*, 35(6):2380–2388, 2002.

[117] H. Bruus. *Theoretical microfluidics, Lecture notes*. Oxford University Press, 2007.

[118] B. J. Kirby and E. F. Hasselbrink. Zeta potential of microfluidic substrates: 2. Data for polymers. *Electrophoresis*, 25(2):203–213, Jan 2004.

[119] F. Baldessari and J. G. Santiago. Electrokinetics in nanochannels: part i. electric double layer overlap and channel-to-well equilibrium. *J Colloid Interface Sci*, 325(2):526–538, Sep 2008.

[120] B. J. Kirby and E. F. Hasselbrink. Zeta potential of microfluidic substrates: 1. Theory, experimental techniques, and effects on separations. *Electrophoresis*, 25(2):187–202, Jan 2004.

[121] R. Probstein. *Physicochemical Hydrodynamics, An Introduction*. John Wiley and Sons, Inc., second edition, 2003.

[122] C. L. Asbury, A. H. Diercks, and G. van den Engh. Trapping of DNA by dielectrophoresis. *Electrophoresis*, 23(16):2658–2666, Aug 2002.

[123] M. Kumemura, D. Collard, C. Yamahata, N. Sakaki, G. Hashiguchi, and H. Fujita. Single DNA molecule isolation and trapping in a microfluidic device. *Chemphyschem*, 8(12):1875–1880, Aug 2007.

[124] A. Kuzyk, B. Yurke, J. J. Toppari, V. Linko, and P. Törmä. Dielectrophoretic trapping of DNA origami. *Small*, 4(4):447–450, Apr 2008.

[125] J. Regtmeier, T. T. Duong, R. Eichhorn, D. Anselmetti, and A. Ros. Dielectrophoretic manipulation of DNA: separation and polarizability. *Anal Chem*, 79(10):3925–3932, May 2007.

[126] J. Regtmeier, R. Eichhorn, L. Bogunovic, A. Ros, and D. Anselmetti. Dielectrophoretic trapping and polarizability of DNA: the role of spatial conformation. *Anal Chem*, 82(17):7141–7149, Sep 2010.

[127] N. Swami, C.-F. Chou, V. Ramamurthy, and V. Chaurey. Enhancing DNA hybridization kinetics through constriction-based dielectrophoresis. *Lab Chip*, 9(22):3212–3220, Nov 2009.

[128] A. Wolff, C. Leiterer, A. Csaki, and W. Fritzsche. Dielectrophoretic manipulation of DNA in microelectrode gaps for single-molecule constructs. *Front Biosci*, 13:6834–6840, 2008.

[129] W.-H. Yeo, J.-H. Chung, Y. Liu, and K.-H. Lee. Size-specific concentration of DNA to a nanostructured tip using dielectrophoresis and capillary action. *J Phys Chem B*, 113(31):10849–10858, Aug 2009.

[130] R. W. Clarke, S. S. White, D. Zhou, L. Ying, and D. Klenerman. Trapping of proteins under physiological conditions in a nanopipette. *Angew Chem Int Ed Engl*, 44(24):3747–3750, Jun 2005.

[131] B. H. Lapizco-Encinas, S. Ozuna-Chacón, and M. Rito-Palomares. Protein manipulation with insulator-based dielectrophoresis and direct current electric fields. *J Chromatogr A*, 1206(1):45–51, Oct 2008.

[132] L. Zheng, J. P. Brody, and P. J. Burke. Electronic manipulation of DNA, proteins, and nanoparticles for potential circuit assembly. *Biosens Bioelectron*, 20(3):606–619, Oct 2004.

[133] M. Castellarnau, A. Errachid, C. Madrid, A. Juárez, and J. Samitier. Dielectrophoresis as a tool to characterize and differentiate isogenic mutants of Escherichia coli. *Biophys J*, 91(10):3937–3945, Nov 2006.

[134] C. Church, J. Zhu, G. Wang, T.-R. J. Tzeng, and X. Xuan. Electrokinetic focusing and filtration of cells in a serpentine microchannel. *Biomicrofluidics*, 3(4):44109, 2009.

[135] R. Gallo-Villanueva, N. Jesus-Perez, J. Martinez-Lopez, A. Pacheco, and B. Lapizco-Encinas. Assessment of microalgae viability employing insulator-based dielectrophoresis. *Microfluidics and Nanofluidics*, pages 1–11, 2011.

[136] M. Gel, Y. Kimura, O. Kurosawa, H. Oana, H. Kotera, and M. Washizu. Dielectrophoretic cell trapping and parallel one-to-one fusion based on field constriction created by a micro-orifice array. *Biomicrofluidics*, 4(2), 2010.

[137] C.-P. Jen and T.-W. Chen. Selective trapping of live and dead mammalian cells using insulator-based dielectrophoresis within open-top microstructures. *Biomed Microdevices*, 11(3):597–607, Jun 2009.

[138] Y. Kang, D. Li, S. Kalams, and J. Eid. DC-dielectrophoretic separation of biological cells by size. *Biomedical Microdevices*, 10:243–249, 2008.

[139] E. T. Lagally, S.-H. Lee, and H. T. Soh. Integrated microsystem for dielectrophoretic cell concentration and genetic detection. *Lab Chip*, 5(10):1053–1058, Oct 2005.

[140] B. H. Lapizco-Encinas, B. A. Simmons, E. B. Cummings, and Y. Fintschenko. Dielectrophoretic concentration and separation of live and dead bacteria in an array of insulators. *Anal Chem*, 76(6):1571–1579, Mar 2004.

[141] H. Shafiee, M. B. Sano, E. A. Henslee, J. L. Caldwell, and R. V. Davalos. Selective isolation of live/dead cells using contactless dielectrophoresis (cDEP). *Lab Chip*, 10(4):438–445, Feb 2010.

[142] S. K. Srivastava, P. R. Daggolu, S. C. Burgess, and A. R. Minerick. Dielectrophoretic characterization of erythrocytes: positive AB0 blood types. *Electrophoresis*, 29(24):5033–5046, Dec 2008.

[143] J. Suehiro, G. Zhou, M. Imamura, and M. Hara. Dielectrophoretic filter for separation and recovery of biological cells in water. *Industry Applications, IEEE Transactions on*, 39(5):1514 – 1521, 2003.

[144] L. Bogunovic, R. Eichhorn, J. Regtmeier, D. Anselmetti, and P. Reimann. Particle sorting by a structured microfluidic ratchet device with tunable selectivity: theory and experiment. *Soft Matter*, 8:3900–3907, 2012.

[145] J. D. Yantzi, J. T. W. Yeow, and S. S. Abdallah. Multiphase electrodes for microbead control applications: integration of DEP and electrokinetics for bio-particle positioning. *Biosens Bioelectron*, 22(11):2539–2545, May 2007.

[146] R. Krupke, F. Hennrich, H. v Löhneysen, and M. M. Kappes. Separation of metallic from semiconducting single-walled carbon nanotubes. *Science*, 301(5631):344–347, Jul 2003.

[147] M. J. Mendes, H. K. Schmidt, and M. Pasquali. Brownian dynamics simulations of single-wall carbon nanotube separation by type using dielectrophoresis. *J Phys Chem B*, 112(25):7467–7477, Jun 2008.

[148] S. K. Srivastava, J. L. Baylon-Cardiel, B. H. Lapizco-Encinas, and A. R. Minerick. A continuous dc-insulator dielectrophoretic sorter of microparticles. *J Chromatogr A*, 1218(13):1780–1789, Apr 2011.

[149] H. Zhou, M. A. Preston, R. D. Tilton, and L. R. White. Calculation of the electric polarizability of a charged spherical dielectric particle by the theory of colloidal electrokinetics. *J Colloid Interface Sci*, 285(2):845–856, May 2005.

[150] J. L. Baylon-Cardiel, N. M. Jesús-Pérez, A. V. Chávez-Santoscoy, and B. H. Lapizco-Encinas. Controlled microparticle manipulation employing low frequency alternating electric fields in an array of insulators. *Lab Chip*, 10(23):3235–3242, Dec 2010.

[151] R. C. Gallo-Villanueva, V. H. Pérez-González, R. V. Davalos, and B. H. Lapizco-Encinas. Separation of mixtures of particles in a multipart microdevice employing insulator-based dielectrophoresis. *Electrophoresis*, 32(18):2456–2465, Sep 2011.

[152] Y.-S. Huang, Y.-H. Peng, and S.-K. Fan. Microfluidic immunosensor based on insulator dielectrophoresis and electrowetting-on-dielectric. *Proceedings of the 2010 5th IEEE International Conference on Nano/Micro Engineered and Molecular Systems*, 2010.

[153] H. Morgan, M. P. Hughes, and N. G. Green. Separation of submicron bioparticles by dielectrophoresis. *Biophys J*, 77(1):516–525, Jul 1999.

[154] L. Zheng, S. Li, P. Burke, and J. Brody. Towards single molecule manipulation with dielectrophoresis using nanoelectrodes. In *Nanotechnology, 2003. IEEE-NANO 2003. 2003 Third IEEE Conference on*, volume 1, pages 437 – 440 vol.2, Aug 2003.

[155] C.-F. Chou, J. O. Tegenfeldt, O. Bakajin, S. S. Chan, E. C. Cox, N. Darnton, T. Duke, and R. H. Austin. Electrodeless dielectrophoresis of single- and double-stranded DNA. *Biophys J*, 83(4):2170–2179, Oct 2002.

[156] R. Krishnan, B. D. Sullivan, R. L. Mifflin, S. C. Esener, and M. J. Heller. Alternating current electrokinetic separation and detection of DNA nanoparticles in high-conductance solutions. *Electrophoresis*, 29(9):1765–1774, May 2008.

[157] S. Tuukkanen, J. J. Toppari, A. Kuzyk, L. Hirviniemi, V. P. Hytönen, T. Ihalainen, and P. Törmä. Carbon nanotubes as electrodes for dielectrophoresis of DNA. *Nano Lett*, 6(7):1339–1343, Jul 2006.

[158] A. D. Goater and R. Pethig. Electrorotation and dielectrophoresis. *Parasitology*, 117 Suppl:S177–S189, 1998.

[159] V. Shilov, A. Delgado, F. González-Caballero, J. Horno, J. López-García, and C. Grosse. Polarization of the electrical double layer. Time evolution after application of an electric field. *J Colloid Interface Sci*, 232(1):141–148, Dec 2000.

[160] H. Zhao. Double-layer polarization of a non-conducting particle in an alternating current field with applications to dielectrophoresis. *Electrophoresis*, 32(17):2232–2244, 2011.

[161] D. Porschke. Macrodipoles. unusual electric properties of biological macromolecules. *Biophys Chem*, 66(2-3):241–257, Jun 1997.

[162] H. Washizu and K. Kikuchi. Electric polarizability of DNA in aqueous salt solution. *J Phys Chem B*, 110(6):2855–2861, Feb 2006.

[163] J. I. Martínez-López, H. Moncada-Hernández, J. L. Baylon-Cardiel, S. O. Martínez-Chapa, M. Rito-Palomares, and B. H. Lapizco-Encinas. Characterization of electrokinetic mobility of microparticles in order to improve dielectrophoretic concentration. *Anal Bioanal Chem*, 394(1):293–302, May 2009.

[164] S. Ozuna-Chacón, B. H. Lapizco-Encinas, M. Rito-Palomares, S. O. Martínez-Chapa, and C. Reyes-Betanzo. Performance characterization of an insulator-based dielectrophoretic microdevice. *Electrophoresis*, 29(15):3115–3122, Aug 2008.

[165] R. V. Davalos, G. J. McGraw, T. I. Wallow, A. M. Morales, K. L. Krafcik, Y. Fintschenko, E. B. Cummings, and B. A. Simmons. Performance impact of dynamic surface coatings on polymeric insulator-based dielectrophoretic particle separators. *Anal Bioanal Chem*, 390(3):847–855, Feb 2008.

[166] B. Saif, R. K. Mohr, C. J. Montrose, and T. A. Litovitz. On the mechanism of dielectric relaxation in aqueous DNA solutions. *Biopolymers*, 31(10):1171–1180, 1991.

[167] C. L. Asbury and G. van den Engh. Trapping of DNA in nonuniform oscillating electric fields. *Biophys J*, 74(2 Pt 1):1024–1030, Feb 1998.

[168] D. Frenkel. Soft condensed matter. *Phsica A*, 313:1–31, 2002.

[169] P. Reimann. Brownian motors: noisy transport far from equilibrium. *Physics Reports*, 361(2-4):57–265, 2002.

[170] A. Einstein. Über die von der molekularkinetischen Theorie der Wärme geforderte Bewegung von in ruhenden Flüssigkeiten suspendierten Teilchen. *Annalen der Physik*, 322(8):549–560, 1905.

[171] P. Hänggi, P. Talkner, and M. Borkovec. Reaction-rate theory: fifty years after Kramers. *Rev. Mod. Phys.*, 62:251–341, Apr 1990.

[172] P. Park and W. Sung. Dynamics of a polymer surmounting a potential barrier: The Kramers problem for polymers. *J Chem Phys*, 111:5259–5266, 1999.

[173] P. Reimann, G. J. Schmid, and P. Hänggi. Universal equivalence of mean first-passage time and Kramers rate. *Phys Rev E Stat Phys Plasmas Fluids Relat Interdiscip Topics*, 60(1):R1–R4, Jul 1999.

[174] Y. Xia and G. M. Whitesides. Soft lithography. *Annual Review of Materials Science*, 28(1):153–184, 1998.

[175] T. W. Odom, J. C. Love, D. B. Wolfe, K. Paul, and G. M. Whitesides. Improved pattern transfer in soft lithography using composite stamps. *Langmuir*, 18:5314–5320, 2002.

[176] D. J. Campbell, K. J. Beckman, C. E. Calderon, P. W. Doolan, R. M. Ottosen, A. B. Ellis, and G. C. Lisensky. Replication and compression of bulk surface structures with polydimethylsiloxane elastomer. *J Chem Educ*, 76(4):537–541, 1999.

[177] M. Viefhues, S. Manchanda, T.-C. Chao, D. Anselmetti, J. Regtmeier, and A. Ros. Physisorbed surface coatings for poly(dimethylsiloxane) and quartz microfluidic devices. *Anal Bioanal Chem*, 401(7):2113–2122, Aug 2011.

[178] S. V. Ermakov, S. C. Jacobson, and J. M. Ramsey. Computer simulations of electrokinetic injection techniques in microfluidic devices. *Anal Chem*, 72(15):3512–3517, Aug 2000.

[179] M. Viefhues, J. Regtmeier, and D. Anselmetti. Fast and continuous-flow separation of dna-complexes and topological dna variants in microfluidic chip format. *Analyst*, 138:186–196, 2013.

[180] M. A. Unger, H. P. Chou, T. Thorsen, A. Scherer, and S. R. Quake. Monolithic microfabricated valves and pumps by multilayer soft lithography. *Science*, 288(5463):113–116, Apr 2000.

[181] H. Becker and C. Gärtner. Polymer microfabrication technologies for microfluidic systems. *Anal Bioanal Chem*, 390:89–111, 2008.

[182] X. Zhang, J. M. Cooper, P. B. Monaghan, and S. J. Haswell. Continuous flow separation of particles within an asymmetric microfluidic device. *Lab Chip*, 6(4):561–566, Apr 2006.

[183] J. S. Kuo and D. T. Chiu. Disposable microfluidic substrates: Transitioning from the research laboratory into the clinic. *Lab Chip*, 11(16):2656–2665, Aug 2011.

[184] P. Mao. *Fabrication and characterization of nanofluidic channels for studying molecular dynamics in confined environments*. PhD thesis, Massachusetts Institute of Technology. Dept. of Mechanical Engineering, 2005.

[185] P. Mao and J. Han. Fabrication and characterization of 20 nm planar nanofluidic channels by glass-glass and glass-silicon bonding. *Lab Chip*, 5(8):837–844, Aug 2005.

[186] N. Pamme. Continuous flow separations in microfluidic devices. *Lab Chip*, 7(12):1644–1659, Dec 2007.

[187] Q. Pu, J. Yun, H. Temkin, and S. Liu. Ion-enrichment and ion-depletion effect iof nanochannel structures. *Nano Lett*, 4:1099–1103, 2004.

[188] S. J. Kim, Y.-C. Wang, J. H. Lee, H. Jang, and J. Han. Concentration polarization and nonlinear electrokinetic flow near a nanofluidic channel. *Phys Rev Lett*, 99(4):044501, Jul 2007.

[189] D. Gillespie. Analytic theory for dilute colloids in a charged slit. *J.Phys.Chem. B*, 114:4302–4309, 2010.

[190] K.-D. Huang and R.-J. Yang. Formation of ionic depletion/enrichment zones in a hybrid micro-/nano-channel. *Microlfuid Nanofluid*, 5:631–638, 2008.

[191] A. Plecis, R. B. Schoch, and P. Renaud. Ionic transport phenomena in nanofluidics: experimental and theoretical study of the exclusion-enrichment effect on a chip. *Nano Lett*, 5(6):1147–1155, Jun 2005.

[192] R. B. Schoch, J. Han, and P. Renaud. Transport phenomena in nanofluidics. *Rev Mod Phys*, 80:839–883, 2008.

[193] D. Erickson, D. Sinton, and D. Li. Joule heating and heat transfer in poly(dimethylsiloxane) microfluidic systems. *Lab Chip*, 3(3):141–149, Aug 2003.

[194] G. Tang, D. Yan, C. Yang, H. Gong, J. C. Chai, and Y. C. Lam. Assessment of Joule heating and its effects on electroosmotic flow and electrophoretic transport of solutes in microfluidic channels. *Electrophoresis*, 27(3):628–639, Feb 2006.

[195] B. G. Hawkins and B. J. Kirby. Electrothermal flow effects in insulating (electrodeless) dielectrophoresis systems. *Electrophoresis*, 31(22):3622–3633, Nov 2010.

[196] S. Sridharan, J. Zhu, G. Hu, and X. Xuan. Joule heating effects on electroosmotic flow in insulator-based dielectrophoresis. *Electrophoresis*, Jul 2011.

[197] R. Eichhorn. personal communication: discussion of simulation of separation and mixing of nanobeads.

[198] A. J. Skulan, L. M. Barrett, A. K. Singh, E. B. Cummings, and G. J. Fiechtner. Fabrication and analysis of spatially uniform field electrokinetic flow devices: theory and experiment. *Anal Chem*, 77(21):6790–6797, Nov 2005.

[199] J. Deval, P. Tabeling, and C.-M. Ho. A dielectrophoretic chaotic mixer. *Proc 15th IEEE workshop on MEMS*, pages 36–39, 2002.

[200] I. Barbulovic-Nad, X. Xuan, J. S. H. Lee, and D. Li. DC-dielectrophoretic separation of microparticles using an oil droplet obstacle. *Lab Chip*, 6(2):274–279, Feb 2006.

[201] T. Kawabata and M. Washizu. *IEEE Transactions on Industry Applications, daraus: Dielectrophoretic detection of molecular bindings*, volume 37. Nov/Dec 2001.

[202] L. R. Huang, J. O. Tegenfeldt, J. J. Kraeft, J. C. Sturm, R. H. Austin, and E. C. Cox. A DNA prism for high-speed continuous fractionation of large DNA molecules. *Nat Biotechnol*, 20(10):1048–1051, Oct 2002.

[203] L. R. Huang, E. C. Cox, R. H. Austin, and J. C. Sturm. Continuous particle separation through deterministic lateral displacement. *Science*, 304(5673):987–990, May 2004.

[204] G. Tang and C. Yang. Numerical modeling of Joule heating-induced temperature gradient focusing in microfluidic channels. *Electrophoresis*, 29(5):1006–1012, Mar 2008.

[205] G. Tang, C. Yang, J. Chai, and H. Gong. Joule heating effect on electroosmotic flow and mass species transport in a microcapillary. *International Journal of Heat and Mass Transfer*, 47(2):215–227, 2004.

[206] J. Elias and D. Eden. Transient electric birefringence study of the persistence length and electrical polarizability of restriction fragments of DNA. *Macromolecules*, 14:410–419, 1981.

[207] L. Yang, K. Arora, W. A. Beard, S. H. Wilson, and T. Schlick. Critical role of magnesium ions in DNA polymerase β's closing and active site assembly. *Journal of the American Chemical Society*, 126(27):8441–8453, 2004. PMID: 15238001.

[208] K. Lee. Stability of ionic complexes prepared from plasmid DNA and self-aggregated chitosan nanoparticles. *Macromolecular Research*, 13:542–544, 2005. 10.1007/BF03218494.

[209] V. Andrushchenko, J. H. Van De Sande, and H. Wieser. Vibrational circular dichroism and IR absorption of DNA complexes with Cu^{2+} ions. *Biopolymers*, 72(5):374–390, 2003.

[210] J. Goodisman, R. Rehfuss, B. Ward, and J. C. Dabrowiak. Site-specific binding constants for Actinomycin D on DNA determined from footprinting studies. *Biochemistry*, 31(4):1046–1058, Feb 1992.

[211] C. Rivetti, M. Guthold, and C. Bustamante. Wrapping of DNA around the E.coli RNA polymerase open promoter complex. *EMBO J*, 18(16):4464–4475, Aug 1999.

[212] M. G. Fried and M. A. Daugherty. Electrophoretic analysis of multiple protein-DNA interactions. *Electrophoresis*, 19(8-9):1247–1253, Jun 1998.

[213] M. Buckle, R. M. Williams, M. Negroni, and H. Buc. Real time measurements of elongation by a reverse transcriptase using surface plasmon resonance. *Proc Natl Acad Sci*, 93(2):889–894, Jan 1996.

[214] B. Johne, M. Gadnell, and K. Hansen. Epitope mapping and binding kinetics of monoclonal antibodies studied by real time biospecific interaction analysis using surface plasmon resonance. *J Immunol Methods*, 160(2):191–198, Apr 1993.

[215] R. L. Rich and D. G. Myszka. Survey of the year 2005 commercial optical biosensor literature. *J Mol Recognit*, 19(6):478–534, 2006.

[216] M. F. Berger and M. L. Bulyk. Universal protein-binding microarrays for the comprehensive characterization of the DNA-binding specificities of transcription factors. *Nat Protoc*, 4(3):393–411, 2009.

[217] J. Zhu and X. Xuan. Particle electrophoresis and dielectrophoresis in curved microchannels. *J Colloid Interface Sci*, 340(2):285–290, Dec 2009.

[218] W. Gong, K. He, M. Covington, S. P. Dinesh-Kumar, M. Snyder, S. L. Harmer, Y.-X. Zhu, and X. W. Deng. The development of protein microarrays and their applications in DNA-protein and protein-protein interaction analyses of Arabidopsis transcription factors. *Mol Plant*, 1(1):27–41, Jan 2008.

[219] A. A. Philippakis, A. M. Qureshi, M. F. Berger, and M. L. Bulyk. Design of compact, universal DNA microarrays for protein binding microarray experiments. *J Comput Biol*, 15(7):655–665, Sep 2008.

[220] M. L. Bulyk. Protein binding microarrays for the characterization of DNA-protein interactions. *Adv. Biochem. Engin./ Biotechnol.*, 104:65–85, 2007.

[221] S. Field, I. Udalova, and J. Ragoussis. Accuracy and reproducibility of protein-DNA microarray technology. *Adv Biochem Eng Biotechnol*, 104:87–110, 2007.

[222] M. F. Berger, A. A. Philippakis, A. M. Qureshi, F. S. He, P. W. Estep, and M. L. Bulyk. Compact, universal DNA microarrays to comprehensively determine transcription-factor binding site specificities. *Nat Biotechnol*, 24(11):1429–1435, Nov 2006.

[223] M. L. Bulyk. DNA microarray technologies for measuring protein-DNA interactions. *Curr Opin Biotechnol*, 17(4):422–430, Aug 2006.

[224] S.-W. Ho, G. Jona, C. T. L. Chen, M. Johnston, and M. Snyder. Linking DNA-binding proteins to their recognition sequences by using protein microarrays. *Proc Natl Acad Sci*, 103(26):9940–9945, Jun 2006.

[225] J. Ragoussis, S. Field, and I. A. Udalova. Quantitative profiling of protein-DNA binding on microarrays. *Methods Mol Biol*, 338:261–280, 2006.

[226] N. C. Stellwagen. Electric birefringence of restriction enzyme fragments of DNA: optical factor and electric polarizability as a function of molecular weight. *Biopolymers*, 20:399–434, 1981.

[227] M. Hanss and J. C. Bernengo. Dielectric relaxation and orientation of DNA molecules. *Biopolymers*, 12:2151–2159, 1973.

[228] O. G. Stonington and D. E. Pettijohn. The folded genome of escherichia coli isolated in a protein-DNA-RNA complex. *Proc Natl Acad Sci*, 68(1):6–9, Jan 1971.

[229] J. Yaneva, E. Paneva, S. Zacharieva, L. Yossifova, and J. Zlatanova. Highly preferential linker histone binding to actinomycin D-treated DNA. *Biotechnology & Biotechnological Equipment*, 23:1048–1052, 2009.

Danksagung

An dieser Stelle möchte ich mich bei allen Personen bedanken, die mich während dieser Arbeit unterstützt haben und so erst ein Gelingen ermöglicht haben.

Professor Dario Anselmetti möchte ich danken, dass ich meine Promotion in seiner Arbeitsgruppe machen konnte. Er ließ mir einen großen Freiraum, so dass ich meine Ideen frei umsetzen konnte und gab mir einige Impulse für weitere interessante Aspekte.

Für seine schnelle Bereitschaft nach meiner Bachelor- und Masterarbeit nun auch meine Dissertation zu begutachten möchte ich Professor Andreas Hütten sehr danken ebenso wie für seine Unterstützung bei manchen bürokratischen Hürden.

Professor Thomas Huser möchte ich danken für die spontane Bereitschaft meine Dissertation zu begutachten.

Dr. Jan Regtmeier hat mich von meiner Bachelor-Arbeit über die Masterarbeit bis hin zu meiner Promotion begleitet und stets unterstützt. Dafür und für die vielen anregenden Diskussionen danke ich ihm sehr.

Dr. Katja Tönsing möchte ich für die Unterstützung danken. Sie war immer da wenn ich Fragen hatte, ob zu bürokratischen Angelegenheiten oder fachlicher Natur.

Die Zusammenarbeit mit Dr. Ralf Eichhorn hat mir sehr geholfen die entwickelten Systeme noch besser zu verstehen. Ich danke ihm für die erschöpfend ausführlichen Diskussionen.

Der Mensch muss zwischendurch auch mal entspannen und etwas essen. Beides konnte ich mit meiner "Mittagstruppe". Hier möchte ich besonders Andreas Helmstedt und Carolin Rademacher danken.

Wenn´s mal wieder nicht läuft: Christoph Pelargus ist da und hilft. Vielen Dank für deinen technischen Support.

Gabi Krome war stets die gute Seele. Ihr möchte ich danken für die Unterstützung bei so manchem "Papierkram".

Dr. Katrin Wollschläger danke ich für die Unterstützung bei der Herstellung der pUC 18 DNA und Hilfe bei Restriction.

Anja Rischmüller möchte ich für die Herstellung der *minicircle* DNA und die moralische Unterstützung danken.

Bei der experimentellen Umsetzungen mancher Ideen wurde ich von sehr guten Studenten unterstützt. Besonders hervorheben möchte ich hier Sonja Wegener, Eugenie Fredrich und Verena Leder. Vielen Dank für eure Hife.

Die Mikrofluidik ist mir über die Jahre sehr ans Herz gewachsen. Das verdanke ich nicht zuletzt auch den anderen "Mikrofluidikern" Lukas Bogunovic, Lukas Galla und Dominik Greif.

Meinen Eltern und meinem Opa möchte ich danken für das große Vertrauen in mich und meine Fähigkeiten. Meinem Vater möchte ich ganz speziell danken: Ich konnte gar nichts

anderes werden als eine Physikerin, denn schon von klein auf war das Gesprächsthema Nummer eins beim Essen wie die Dinge funktionieren und warum etwas so ist wie es ist. Schon damals wurde meine Neugier geweckt.

Meinem Mann Tim möchte ich danken für die Unterstützung über all die Jahre meines Studiums. Ich weiß, dass es gerade in der Schlussphase schwierig war mich zu ertragen, aber du hast es geschafft und mich darüberhinaus auch noch aufgebaut und ermuntert. Vielen Dank!!!